UILU-ENG 84-3601

Report No. 101

MODELING CYCLIC DEFORMATION AND FATIGUE BEHAVIOR OF CAST IRON UNDER UNIAXIAL LOADING

by

Stephen Douglas Downing*
Department of Mechanical and Industrial Engineering, UIUC
*Presently with Deere and Company, Moline, IL

A Report of the
MATERIALS ENGINEERING - MECHANICAL BEHAVIOR
College of Engineering, University of Illinois at Urbana-Champaign
January 1984

ABSTRACT

A model for estimating cyclic deformation behavior of cast irons under unaxial loading is described. The model separates total response into components due to symmetrical elastic/plastic response in the matrix/graphite composite and to the nonlinear elastic response of the free graphite phase. Predictions are compared to experimental data for gray cast iron, compacted graphite cast iron and nodular iron.

A continuum damage model for fatigue analysis of cast iron is also discussed. The model considers damage to be a global measure of surface crack growth. Several easily measured bulk deformation parameters are studied as alternate measures of damage. The model is compared with Miner's Rule for gray iron under various loading histories.

Finally, the cyclic deformation model is extended to include transient effects due to surface crack growth and compared to experimental data for gray iron.

ACKNOWLEDGEMENT

This investigation was conducted in the Materials Engineering Research Laboratory, University of Illinois, Urbana, with Professor F. V. Lawrence as Head and the Engineering Mechanics Department of the Deere & Company Technical Center, Moline, Illinois, with Dr. H. D. Berns as Manager. Partial funding was provided by the Fracture Control Program, College of Engineering, University of Illinois.

Professor Darrell F. Socie is gratefully acknowledged for the many stimulating discussions which both initiated and aided in the completion of this work. Mr. D. R. Galliart is thanked for the many years of personal and professional association which helped the author realize his goals.

Ms. G. E. Leese reviewed the original manuscript and made many valuable suggestions for its improvement. Ms. C. A. Brown and Ms. L. K. Popp are thanked for typing the manuscript.

Finally, the author wishes to thank his father, John C. Downing, whose example demonstrated that age need not hinder the pursuit of further education, and his wife, Diane, for the financial and emotional sacrifice necessary for the completion of this work.

TABLE OF CONTENTS

LIST OF SYMBOLS

σ	Stress
σ_{max}	Maximum tensile stress
σ^*	Peak tensile stress at a given cycle number
σ_m	Stress in the matrix
σ_g	Stress in the graphite
σ_B	Bulk stress
$(\sigma_B)_i$	Bulk stress at reversal i
$\Delta\sigma_B$	Bulk stress range
$(\sigma_B)_T$	Bulk stress in tension
$(\sigma_B)_C$	Bulk stress in compression
$(\sigma_M)_T$	Monotonic tensile stress
$(\sigma_M)_C$	Monotonic compressive stress
σ_G	Compressive stress due to graphite constraint
σ_{cc}	Compressive stress due to crack closure
σ_0	Mean stress
ε	Strain
$\Delta\varepsilon$	Strain range
ε_a	Strain amplitude
ε_S	Secant strain
ε_R	Remaining plastic strain
ε'	Strain at which boundary conditions, B_1 and B_2, are evaluated
ε_{max}	Maximum strain in a block history
ε_{min}	Minimum strain in a block history

m	Slope of secant modulus versus stress curve
m_T	Tensile secant slope
m_C	Compressive secant slope
m_B	Bulk secant slope
m_u	Unloading modulus parameter
K	Strength coefficient
K_T	Tensile strength coefficient
K_C	Compressive strength coefficient
K_B	Bulk strength coefficient
n	Strain hardening exponent
n_T	Tensile strain hardening exponent
n_C	Compressive strain hardening exponent
n_B	Bulk strain hardening exponent
F	Force
a^*	Crack length at given cycle number
a_f	Final crack length
A_m	Area fraction of the matrix
A_g	Area fraction of the graphite
A_{eff}	Cross-sectional area fraction unaffected by surface cracking
A_{eff}^*	Effective area fraction at a given cycle count
$(A_{eff})_{max}$	Effective area fraction at zero damage
E_0	Tangent modulus at zero stress and strain
E_S	Secant modulus
$(E_S)_{linear}$	Linear portion of the secant modulus versus stress curve
E_u	Unloading modulus from peak tensile stress

E_u^*	Unloading modulus at a given cycle number
$(E_u)_{max}$	Unloading modulus at zero damage
E_m	Elastic modulus of the matrix
E_g	Elastic modulus of graphite
ΔW^*	Hysteresis energy at a given cycle number
ΔW_{max}	Hysteresis energy at zero damage
Q, q	Coefficient and exponent of crack closure reponse at zero damage
Q', q'	Coefficient and exponent of crack closure response at given damage level
B_1, B_2	Boundary conditions for calculating Q and q
D	Fatigue damage
D_i	Fatigue damage before application of cycle i
ΔD	Fatigue damage increment
D_{MR}	Fatigue damage calculated by Miner's Rule
N	Number of applied cycles
N_i	Number of repetitions of cycle i
N_f	Number of cycles to failure
N_{fi}	Number of cycles to failure for cycle i
B_f	Number of blocks to failure
P	Damage rate parameter
P_i	Damage rate parameter for cycle i
R_P	Ratio of damage rate parameters and equal to $(P_2 + 1)/(P_1 + 1)$

I. INTRODUCTION

A. Background

With the birth of gray iron at the turn of the nineteenth century, the foundry industry began a period of rapid and sustained growth. Simpson [1]* considers gray iron "the most versatile and diverse of all cast metals" and "a metal little understood and still greatly underestimated". Since that time the developments of malleable iron (spheriodal graphite obtained by annealing), nodular iron (spheriodal graphite obtained by innoculation) and compacted graphite iron have greatly increased the range of ferrous-based cast materials available to designers. Unfortunately, analytical tools for evaluating the fatigue resistance and asymmetrical deformation behavior in cast irons have not developed as rapidly.

In the absence of a well-defined methodology for analyzing cast irons, procedures developed for wrought materials have been used, in most cases, incorrectly. For wrought materials, it is often convenient to separate the fatigue process into two parts; a portion of life spent in crack initiation and a portion spent in crack propagation. No such clear distinction exists for most cast irons; the dominant portion of fatigue life

---

* Numbers in brackets refer to corresponding items in the list of references

is spent in growth and linking up of multiple crack systems. This thesis contends that both fatigue resistance and deformation behavior in cast irons are controlled by this phenomenon. Data supporting this contention are provided.

Readers unfamiliar with these cast irons should refer to the material descriptions given in Appendix A.

B. Objectives

The overall objective of this work is to identify the mechanisms which control fatigue resistance and deformation behavior in cast iron and to develop a consistent methodology for their characterization. It is intended that the analysis be as straightforward as possible by concentrating on the most important variables. It would certainly be advantageous to the stress analyst and designer if the calculation of fatigue life and cyclic deformation of cast irons was no more difficult than for wrought metals.

The procedures described in this thesis were initially developed for gray cast iron because its behavior differs greatly from wrought metals. Nodular iron, on the other hand, exhibits characteristics which are, in some ways, similar to steel. It is intended that the described analysis procedures be applicable to the full spectrum of cast irons, including gray, compacted graphite, malleable and nodular cast irons.

C. Approach

The procedure for estimating the fatigue life of smooth specimens of cast iron is shown in Fig. 1. It is similar to procedures used for wrought metals with the following exceptions:

(1) Material properties for fatigue resistance and deformation behavior reflect not only elastic/plastic response in the matrix, but also nonlinear elastic effects of surface crack growth and graphite behavior.

(2) The cyclic deformation model treats cast iron as an initially cracked material.

(3) A continuum damage model replaces the linear damage model (Miner's Rule) commonly used for wrought metals.

II. STRESS/STRAIN RESPONSE

A. Background

Prior investigations have shown that stress/strain response in cast iron is controlled by the properties of the steel matrix and, more importantly, the details of graphite morphology. Quantity, distribution, and shape of the free graphite all affect the degree to which the steel matrix is weakened. To simulate tensile behavior in gray iron, Thum and Ude [2] subjected steel plates containing arrays of slots to tensile loading and showed that the load/displacement curves are similar to tensile stress/strain curves of gray cast iron. Also, when the length of the slots was increased, elastic stiffness was decreased, just as gray iron is more compliant with longer flakes. Similarly, Coffin [3] treated gray cast iron as a steel matrix containing internal notches. He considered a properly oriented graphite flake in a tensile field to have an effective stress concentration factor of approximately three. Flinn and Ely [4] stated that free graphite would have a similar effect on the tensile properties as voids, that is, the modulus of the matrix between the graphite should be the same as for steel. MacKensie [5] contended that, in compression, free graphite would behave as voids filled with incompressible fluid.

Other researchers have reported that, for gray iron under tensile loading, properly oriented graphite flakes crack and debond from the matrix. Clough and Shank [6] assumed this phenomenon occurred uniformly

throughout the material. However, a detailed study by Gilbert [7] of the microstructure of gray iron under tensile load indicated that graphite debonding occurs only near the free surface. In other papers [8, 9] on stress/strain response in gray iron, he made the following observations:

(1) Curvature in the tensile stress/strain curve is not only associated with elastic and plastic deformation of the matrix, but is also due to volume increase in spaces occupied by the graphite.

(2) This volume increase is most pronounced on the specimen surface where graphite flakes, oriented perpendicular to the load, can actually crack or debond from the matrix.

(3) Gray iron is stiffer in compression than tension because spaces occupied by the graphite do not see corresponding decreases in volume.

Another contention of some researchers is that gray iron behaves as a precracked material. Mitchell [10] showed similarity in closed hysteresis loops of gray cast iron to those of mild steel with observable cracks. By using replicating techniques, Fash and Socie [11] found evidence to support this contention. Fatigue cracks initiating at graphite flake tips were detected very early in the life of gray iron specimens. Russell [12] implemented this idea with elastic/plastic finite element analysis to model gray iron cyclic deformation behavior. In his two-dimensional

model, graphite flakes were modeled as cracked members which could transmit only compressive stress. While good qualitative agreement was found, the approach was too complicated for general use.

Downing and Socie [13] used a more practical approach where finite element analysis was replaced by a simple ligament model. Using this as a basis, they developed a set of simple constituative equations for cyclic stress/strain response in gray cast iron. While these equations gave good first approximations, certain aspects of predicted response were incorrect.

Nodular iron has similar matrix structure to gray iron, but free graphite is in the form of roughly spherical nodules rather than interconnected graphite flakes. Because the internal notch effect of spheroidal graphite is much less severe than for graphite flakes, nodular iron behaves elastically over a considerable stress range in tension and compression. The elastic limit in compression is, however, slightly higher than in tension as shown by Gilbert [14]. This phenomenon is attributed to a greater local stress concentration effect in tension, resulting in plastic deformation at a lower average stress. Gilbert also considered that, at tensile stresses above the elastic limit, the volume of spaces occupied by graphite increased due to voids formed in the direction of loading. Contrary to the behavior of gray iron, however, little overall increase in volume occurred under compressive stress. Testin's data [15] also suggest nearly symmetrical behavior for nodular iron.

Compacted graphite (CG) cast iron, which possesses a graphite configuration intermediate to that of conventional gray and nodular irons, has recently become recognized as a viable material for commercial production. Mechanical properties of CG irons far surpass those of gray irons, but thermal conductivity, resistance to thermal shock, and machinability are more similar to gray than nodular irons. Studies of deformation behavior and fatigue resistance of CG irons [16,17] indicate mechanical properties bounded by those of gray iron and nodular iron.

B. Monotonic Behavior

Monotonic stress/strain curves for the range of cast irons from gray to nodular differ greatly in character. Gray iron exhibits highly asymmetrical behavior and neither tensile nor compressive stress/strain curves show definable elastic limits. Nodular irons, on the other hand, do remain linearly elastic over a considerable range of stress, and tensile and compressive behavior is nearly identical. In order to facilitate development of a consistent cyclic deformation model, a single constitutive relationship which adequately represents the monotonic tensile and compressive curves for all cast irons is desirable. Development of such a relationship follows. Again the model is developed for gray iron, it being the most difficult to model.

In a paper on the stress/strain properties of flake graphite cast iron, Gilbert and Kemp [18] investigated variation in the secant modulus as a function of stress. Secant modulus, defined as the slope of a line

from the origin to a point on the stress/strain curve, was plotted against stress level. Figure 2 shows that secant modulus, E_S, for the gray iron employed in this investigation, is linear with stress over a considerable stress range. The intercept of the initial straight-line portion at zero stress defines the tangent modulus, E_0, at the origin of the monotonic stress/strain curve. Slope, m, reflects the amount of initial stress/strain curvature. Together these parameters define an expression for the linear portion of the secant modulus curve

$$(E_S)_{linear} = E_0 + m\sigma \tag{1}$$

from which a corresponding component of total strain, termed the secant strain, ε_S, may be calculated. Total strain, ε, is the sum of secant strain and the remaining plastic strain, ε_R,

$$\varepsilon = \varepsilon_S + \varepsilon_R \tag{2}$$

and secant strain is expressed by

$$\begin{aligned} \varepsilon_S &= \sigma/(E_S)_{linear} \\ &= \sigma/(E_0 + m\sigma) \end{aligned} \tag{3}$$

In gray iron, plastic strain occurs at the graphite flake tips at low stress levels due to their high stress concentration factors. Remaining plastic strain is analogous to net section plastic strain in wrought materials.

At higher stress levels, the secant modulus/stress curve deviates from linearity, indicating that ε_R is increasing in magnitude. Remaining plastic strain is determined at each stress level by subtracting the calculated secant strain from total strain. Figure 3 indicates a power law relationship between stress and remaining plastic strain in the same manner as stress and plastic strain are related in wrought metals. This yields the following expression for ε_R as a function of stress

$$\varepsilon_R = (\sigma/K)^{1/n} \tag{4}$$

where n is the slope of the curve in Fig. 3 and K is the intercept at $\varepsilon_R = 1$. A constitutive equation for monotonic stress/strain behavior is then obtained by combining Eqs. (2)-(4).

$$\varepsilon = \frac{\sigma}{E_0 + m\sigma} + (\sigma/K)^{1/n} \tag{5}$$

Figures 4-6 indicate that this equation provides an excellent fit to both the tensile and compressive stress/strain curves of gray iron, CG iron and nodular iron, respectively. Table 1 shows values for the material properties, E_0, m, K and n, for tensile and compressive curves of gray, CG, and nodular cast irons. In general, separate sets of material

properties are needed for tension and compression. It should be noted that Eq. (5) becomes the well-known Ramberg-Osgood equation used for wrought metals if m is zero. Thus, it should have general applicability for irons up to and including steels which have been traditionally characterized by the Ramberg-Osgood formulation.

The constitutive relationship described by Eq. (5) is not, by itself, sufficient for modeling cyclic behavior. Additional information concerning the effects of free graphite is needed. The next three sections describe the individual components of total stress/strain response which are: (1) the symmetrical bulk response, (2) compressive stress due to internal graphite constraint, and (3) compressive stress due to surface crack closure.

C. Bulk Behavior

A simple mechanics of materials approach is used to evaluate the symmetrical elastic/plastic response of the metal matrix and graphite. This behavior is to be termed Bulk Response. Consider a unit cube of steel matrix containing one representative eutectic cell. For gray iron, the eutectic cell consists of interconnected graphite flakes forming a cell of roughly spherical shape. The eutectic cell for nodular iron is considered to be an individual graphite nodule. Figure 7 diagrammatically depicts a unit cube of gray iron. At an infinitesimal slice, dx, through the cross-section at some distance, x, are seen what appears to be individual graphite flakes. The total force in the x-direction, F, could be expressed as

$$F = \sigma_m A_m + \sigma_g A_g$$

$$= \sigma_m (1 - A_g) + \sigma_g A_g \tag{6}$$

where (σ_m, A_m) and (σ_g, A_g) are the stresses and area fractions of the matrix and graphite, respectively. For elastic deformation in both the matrix and graphite

$$F = \varepsilon[E_m(1 - A_g) + E_g A_g] \tag{7}$$

where E_m is the elastic modulus of the matrix and E_g is the elastic modulus of graphite.

Bulk stress/strain response is dominated by the metal matrix ($E_m >> E_g$ and A_g is typically less than 0.25) and is assumed to have characteristics similar to wrought metals in the elastic and plastic regimes. Of primary significance are Masing behavior (where outer loops are the same as initial loading curves if both stresses and strains are multiplied by 2) and material memory (the occurrence of closed hysteresis loops).

Using these assumptions, the bulk stress/strain curve will have the same form as the monotonic curves, that is,

$$\varepsilon = \frac{\sigma_B}{E_0 + m_B \sigma_B} + \left(\frac{\sigma_B}{K_B}\right)^{1/n_B} \tag{8}$$

where σ_B is the bulk stress at a given strain, ε, and m_B, K_B, and n_B are material properties. Here the same material properties are used for both tension and compression.

Constitutive equations for bulk stress/strain response under cyclic loading are

$$(\sigma_B)_i = (\sigma_B)_{i-1} \pm \Delta\sigma_B \tag{9}$$

and

$$\Delta\varepsilon = \frac{\Delta\sigma_B}{E_0 + (m_B/2)\Delta\sigma_B} + 2\left(\frac{\Delta\sigma_B}{2K_B}\right)^{1/n_B} \tag{10}$$

where $(\sigma_B)_i$ = bulk stress at reversal i

$(\sigma_B)_{i-1}$ - bulk stress at reversal i-1

$\Delta\sigma_B$ = bulk stress range, and

$\Delta\varepsilon$ = strain range

The sign of $\Delta\sigma_B$ in Eq. (9) is positive for loading and negative for unloading. Selection of values for material properties, m_B, K_B and n_B, will be discussed in a later section.

Because of the symmetrical nature of the bulk response, additional components of the total response are needed to adequately describe the deformation behavior of graphite flake cast irons. These components, described in the following three sections, quantity the effects of internal graphite constraint and surface cracking.

D. Internal Graphite Behavior

One of the characteristics of cast iron (gray iron in particular) is its greater stiffness in compression than tension. Under compressive loading, properly oriented graphite is constrained such that it approaches incompressibility. Additional compressive stress is transferred to the inherently stiffer matrix; therefore, a component of stress which accounts for this phenomenon must be defined. Addition of this stress, σ_G, and bulk stress in compression must result in the monotonic compressive stress/strain curve. Therefore, σ_G may be expressed by

$$\begin{aligned} \sigma_G &= (\sigma_M)_C - (\sigma_B)_C \quad \text{if } \varepsilon \leq 0 \\ &= 0 \qquad\qquad\quad \text{if } \varepsilon > 0 \end{aligned} \tag{11}$$

where $(\sigma_M)_C$ is the monotonic compressive response and $(\sigma_B)_C$ is the bulk response in compression. This stress partially accounts for the inflection point on the unloading portion of some gray and CG iron hysteresis loops. Also, it is considered nonlinear elastic and dependent only on compressive strain. Experimental justification for this assumption is presented later.

For low compressive strains, this graphite stress may be determined directly from the secant components of the bulk compressive stress/strain curves, or

$$\sigma_G = E_0\varepsilon/[1 + m_C\varepsilon] - E_0\varepsilon/[1 + m_B\varepsilon] \quad \text{if } \varepsilon \leq 0$$
$$= 0 \quad \text{if } \varepsilon > 0 \tag{12}$$

When compressive strains are of sufficient magnitude that the remaining plastic strain components are no longer negligible, an iterative approach is required. At each compressive strain level, Eqs. (5) and (8) must be solved for $(\sigma_M)_C$ and $(\sigma_B)_C$ and σ_G calculated from Eq. (11). The Newton-Raphson iteration technique works well for these solutions. By separating compressive strain into discrete intervals, it is possible to perform all iterative solutions in advance and to store the results in an array. This array may be used in conjunction with the other components of total stress to perform an efficient stress/strain simulation.

E. Surface Behavior

As previously mentioned, numerous researchers have detected cracks and crack-like defects (debonded graphite) on the surface of cast iron specimens loaded in tension. Phenomenologically, this is significant, for it results in changes of specimen compliance at high tensile stresses. Decreases in the unloading modulus from tensile peaks of flake iron hysteresis loops are evidence of these changes.

Figure 8 illustrates that the unloading modulus decreases with increasing stress for gray cast iron. Unloading modulus, E_u, and maximum stress for each hysteresis loop in Fig. 8 correlate as shown in Fig. 9. A linear relationship is indicated resulting in

$$E_u = E_0 + m_u \sigma \tag{13}$$

where m_u is the slope. The intercept at zero stress, E_0, is indistinguishable from the tangent modulus of the monotonic stress/strain curve and is therefore considered equivalent. Gilbert and Kemp [18] also observed similar behavior.

Differences in the elastic modulus of steel and cast iron reflect a reduced effective cross-sectional area for cast iron specimens due to the presence of free graphite. Several investigators [19,20] subscribe to this argument. Similarly, the decrease in unloading modulus, which results from surface cracking, is evidence of further degradation in effective area. It is useful then to define a dimensionless parameter, A_{eff}, to be the fraction of cross-sectional area unaffected by surface cracking. For an unstressed cast iron specimen, A_{eff} is assumed equal to unity. Since surface cracking is reflected in decreased unloading modulus, A_{eff} is expressed by

$$A_{eff} = E_u/E_0 \tag{14}$$

or by substituting Eq. (13)

$$A_{eff} = 1 + \frac{m_u \sigma_{max}}{E_0} \tag{15}$$

Bulk behavior, described earlier, is the symmetrical response of the metal matrix and graphite without the effects of graphite constraint and surface cracking. Graphite stress, σ_G, is nonzero only for compressive strains. Therefore, the stress reached by cast iron under monotonic tensile loading must be the product of bulk stress and the effective area fraction or

$$(\sigma_M)_T = A_{eff} (\sigma_B)_T \tag{16}$$

Manipulation of Eqs. (5), (8) and (16) for low tensile stress levels results in

$$A_{eff} = 1 + \frac{(m_T - m_B)\sigma_{max}}{E_0} \tag{17}$$

This expression is identical to Eq. (15) if

$$m_B = m_T - m_u \tag{18}$$

The other bulk material properties, K_B and n_B, can be determined as follows:

(1) Determine monotonic tensile stress at a number of strain levels from Eq. (5).

(2) Calculate corresponding $A_{eff's}$ from Eq. (15).

(3) Calculate corresponding σ_B's from Eq. (16).

(4) Calculate the bulk remaining plastic strain from

$$\varepsilon_R = \varepsilon - \frac{\sigma_B}{E_0 + m_B\sigma_B}$$

(5) Perform linear regression on log σ_B vs. log ε_R to obtain K_B and n_B.

In actual practice, bulk stress at discrete strain intervals can be determined from Step (3) and stored in an array for future processing.

At some point during unloading, open surface cracks close and add compressive stress to the overall response. Therefore, a stress component, σ_{cc}, due to crack closure must be defined. Mathematical formulation of this stress is given in the next section.

F. Cyclic Stress/Strain Response Model

The total stress/strain response for cast iron under cyclic loading is given by

$$\sigma = A_{eff}(\sigma_B + \sigma_G) + (1 - A_{eff})\sigma_{cc} \qquad (19)$$

The first term, $A_{eff}\ (\sigma_B + \sigma_G)$, represents the bulk and graphite stresses acting over the fraction of cross-sectional area unaffected by surface cracking. The second term, $(1 - A_{eff})\sigma_{cc}$ is the compressive crack closure stress acting over the remaining area. All terms have been defined previously with the exception of σ_{cc}.

Numerous formulations of σ_{cc} were attempted with the following power-law relationship proving most effective and convenient:

$$\sigma_{cc} = Q(\varepsilon_{max} - \varepsilon)^q \tag{20}$$

where Q and q are new constants which depend on monotonic material properties and the strain limits. These new constants are determined by imposing appropriate boundary conditions, B_1 and B_2, to σ_{cc} and $d\sigma_{cc}/d\varepsilon$, respectively at some strain, ε'. The constants, Q and q, are then expressed by

$$q = -(B_2/B_1)\ (\varepsilon_{max} - \varepsilon') \tag{21}$$

and $$Q = B_1/(\varepsilon_{max} - \varepsilon')^q \tag{22}$$

The rationale for choosing B_1 and B_2 is outlined below.

Observations of initial stress/strain hysteresis loops of cast iron specimens cycled between strain limits ε_{max}, ε_{min} lead to the following conclusions:

(1) If $|\varepsilon_{max}| \leq |\varepsilon_{min}|$, the unloading curve of the hysteresis loop at $\varepsilon' = \varepsilon_{min}$ has the same magnitude as the monotonic compressive stress/strain curve at $\varepsilon' = \varepsilon_{min}$, and

(2) If $|\varepsilon_{max}| > |\varepsilon_{min}|$, the unloading curve of the hysteresis loop at $\varepsilon' = -\varepsilon_{max}$ would have the same magnitude as the monotonic compressive stress/strain curve at $\varepsilon' = -\varepsilon_{max}$

In fact, under completely-reversed strain cycling, the peak tensile and compressive stresses generally lie on the monotonic tensile and compressive curves, respectively. The boundary conditions, B_1 and B_2, may then be expressed by

$$B_1 = (\sigma_M)_c \Big|_{\varepsilon'}$$
$$B_2 = E_0 \tag{23}$$

$$\text{where } \varepsilon' = \varepsilon_{min} \quad \text{if } |\varepsilon_{max}| \leq |\varepsilon_{min}|$$
$$= -\varepsilon_{max} \quad \text{if } |\varepsilon_{max}| > |\varepsilon_{min}| \tag{24}$$

The expression $B_2 = E_0$ states that the response returns to full stiffness at ε' due to crack closure. In practice, all constants can be determined in advance if the maximum and minimum strains are known.

Crack closure stress, σ_{cc}, is also considered nonlinear elastic. Thus, neither σ_{cc} nor the graphite stress, σ_G, contribute to hysteresis energy in cast iron; if so, the elastic/plastic bulk response must then be the sole cause of area in cast iron hysteresis loops. The imposition of Masing behavior on bulk response dictates that, for this model, the distribution of hysteresis energy must be symmetrical with respect to the

mean strain of a hysteresis loop. Stated another way, the height of cast iron hysteresis loops must be a maximum at and symmetrical about the mean strain. Figure 10 provides experimental verification. The height (stress difference of loading and unloading curves at the same strain) of several hysteresis loops of gray iron at various mean levels is plotted against strain. Even though gray cast iron is highly asymmetrical in terms of absolute stress, these curves demonstrate essentially symmetrical strain energy behavior. Minor deviations in symmetry are initially observed in hysteresis loops with large negative mean strains. Subsequent loops rapidly approach symmetrical behavior.

Figure 11 shows the total and individual components of stress/strain response for a representative gray iron hysteresis loop. Stress/strain simulation of cast iron by this method is well-suited to computer implementation. Details are contained in Appendix B.

G. Test Results

Stress/strain response predictions were made for smooth specimens of gray, compacted graphite and nodular cast irons, all tested in strain-control. Metallurgical and chemical descriptions of the irons tested are included in Appendix A.

Predicted and experimental data for three gray iron constant amplitude tests are shown in Figs. 12-14. Agreement between experimental observations (circular symbols) and predicted results (solid lines) is considered good. Predictions were made using only data from monotonic tension and

compression tests and the incremental test shown in Fig. 9. In general, best agreement was found for tests with zero and higher mean strain levels. It appears that cyclic stability of the steel matrix occurs more quickly at higher stress levels, thus the assumption of symmetry in hysteresis energy is more valid for these tests.

Similar results were obtained for compacted flake iron (Fig. 15) and nodular iron (Fig. 16). Nodular iron stress/strain response is nearly symmetrical in stress behavior. The stress/strain response model correctly accounts for this by making σ_{cc} and σ_G very small.

A series of variable amplitude tests were also conducted for gray iron. Two of the strain histories tested are shown in Fig. 17. These tests were also conducted in strain control on a computer-controlled servo-hydraulic testing system. Experimental and predicted responses are shown in Figs. 18 and 19 and tabulated values of the peak stresses in MPa are also given in Fig. 17. Other strain histories and maximum amplitudes were also investigated but are not reported here since the results are similar.

H. Discussion

The cyclic deformation model presented accurately predicts the initial stress/strain response of cast iron under variable loading. Eight material constants (m_T, K_T, n_T, m_C, K_C, n_C, m_u and E_0) are needed compared with four needed for wrought materials (with the same properties in tension and compression). These can be obtained from the following three tests:

(1) Monotonic tensile test

(2) Monotonic compressive test

(3) Incremental loading test to determine the unloading modulus parameter, m_u

Because of the inherent variability of cast iron, it may be desirable to obtain material properties in a way which produces better average response. A potential method for determining these materials constants from companion fatigue specimens will be described in a later section.

Experimental evidence validates the assumption of nonlinear elastic behavior for the effects of internal graphite constraint and surface crack closure.

The stresses and strains estimated with this model are to be used as input to appropriate cumulative damage procedures for predicting fatigue life. Development of a continuum damage model for fatigue analysis of cast iron is covered in the next section.

III. CUMULATIVE FATIGUE DAMAGE

A. Background

Early methods for estimating fatigue life in cast materials were identical to those used for wrought metals. Simple S/N curves were used, an endurance limit assumed and numerous factors devised to account for size effect, mean stress, surface finish, etc. The approach was totally empirical. Concerted efforts to establish design stresses left little time for identifying and understanding the controlling mechanisms of fatigue. Many cast iron fatigue design codes in use today are still based on procedures developed for wrought metals.

In an attempt to model the structure of cast iron in a more realistic manner, several researchers considered cast iron analogous to notched steel by assigning a fatigue reduction factor to the graphite morphology. Neuber's Rule [21] and low cycle fatigue concepts were then used to predict crack initiation. Mitchell [22] first implemented this model for gray cast iron and later extended it to include nodular iron, cast steel and high hardness wrought steels. Testin [23] used a similar approach for nodular cast iron. While crack initiation concepts might be applicable to cast iron at long lives, their validity in low cycle fatigue ($<10^5$ cycles) is questionable. In this life regime, the total fatigue life of cast irons is clearly dominated by complex crack growth.

Several researchers have reported fatigue cracks on the surface of cast iron specimens at very small fractions of total life. Cracks are observed to form uniformly over the surface and then propagate inward. Fash [24] documented surface crack growth in gray iron with detailed replicas taken periodically during specimen life. Cracks initiated at the tips of properly oriented graphite flakes almost immediately upon application of load, then underwent a complex process of linkage and growth. Not until the life was far advanced did a single dominant crack become evident. Using the same procedures, Molinaro [25] found similar cracking in compacted flake iron. Starkey and Irving [26] found that microcrack growth commenced from pores in nodular iron within a few percent of the life for lives up to 10^5 reversals and utilized elastic/plastic fracture mechanics concepts to predict fatigue life. Hua [30] had similar success with nodular iron. In the general case, the crack systems, particularly in gray iron, are far too complex to be analyzed with conventional fracture mechanics techniques. However, continuum damage analysis does have potential for dealing with these materials.

In the following analysis, damage will be considered a state variable, that is, a single scalar parameter describing the internal state of the material. The damage parameter, D, is some unknown function of strain range, mean stress and applied cycles or

$$D = f(N/N_f, \Delta\varepsilon, \sigma_0) \tag{25}$$

where, for convenience, damage varies from D = 0 for an undamaged state to D = 1 at failure. The rate of damage accumulation with cycles is expressed by

$$\frac{dD}{dN} = g(D, \Delta\varepsilon, \sigma_0) \tag{26}$$

where D replaces N/N_f, assuming there is some relationship between the current damage state and previously accumulated cycles.

In the development of the damage model, it is first necessary to establish a relationship between cycles to failure, N_f, and the loading parameters, $\Delta\varepsilon$ and σ_0. Again, considerable effort has been directed toward the characterization of gray iron because its behavior differs greatly from wrought metals.

B. Material Properties

The relationship between loading parameters and cycles to failure for cast irons should, in some way, account for the surface crack phenomenon. Smith, Watson and Topper [28] suggested a parameter, the product of the maximum stress and strain amplitude in a hysteresis loop, to include the effects of mean stress and early crack growth for fatigue in metals. Figure 20 shows this parameter plotted against cycles to failure for pearlitic gray iron under a variety of testing conditions. Peak stress and strain amplitude can be measured initially or at the half life with

equally good correlation. This parameter, $\sigma_{max}\varepsilon_a$, not only accounted for mean stress, but provided a single relationship for both load-control and strain-control data. Fash and Socie [29] found the following relationship for the pearlitic gray iron investigated,

$$\sigma_{max}\varepsilon_a = 1.82\ (N_f)^{-0.25} \tag{27}$$

where σ_{max} is maximum tensile stress in MPa and ε_a is strain amplitude. Both were determined from the initial hysteresis loop.

Having established the relationship between the loading parameters and fatigue life, it is necessary to define fatigue damage quantitatively. In the phenomenological approach, equivalent damage can only be determined by extensive two level testing. The selection of physically-based damage parameters can reduce the testing required.

C. Measures of Damage

The most direct assessment of damage in cast irons relates to measured crack development. A damage parameter based on crack growth is expressed by

$$D = a^*/a_f \tag{28}$$

where a^* is the length of the crack that grows to failure at a given point in life and a_f is the final crack length. Figure 21 shows crack length as a function of normalized life, N/N_f, for pearlitic gray iron at several

strain amplitudes. The rate of crack growth increases with increasing strain amplitude which indicates faster damage rates for higher levels of loading. Since crack growth is the dominant failure mechanism, equivalent crack length is considered to represent equivalent damage. Because the complex nature of crack growth in gray iron presents difficulties in determining the dominant crack length, the definition of alternate, more easily measured damage parameters relating to surface behavior is desirable. Among those considered were peak stress drop, hysteresis energy drop and unloading modulus drop.

For strain control tests of gray iron, the maximum tensile stress decreases with increased cycling as shown in Fig. 22. Figure 23 shows peak tensile stress behavior at a number of strain levels for pearlitic gray iron. The rate of stress drop increases with increasing strain amplitude indicating a faster rate of damage accumulation at higher strains. The damage relationship in terms of peak stress drop is

$$D = [1 - \sigma^*/\sigma_{max}] \tag{29}$$

where σ^* is the peak stress at a given cycle number and σ_{max} is the initial peak stress. Again, damage varies between $D = 0$ when $\sigma^* = \sigma_{max}$ and $D = 1$ when the material can no longer transmit tensile stress. Equation (29) is intended to reflect a reduction in tensile load carrying capacity due to surface cracking; however, some of the variation in peak stress may be the result of transient matrix behavior. Some mean stress relaxation of the matrix is undoubtedly present for nonzero mean strains and does not directly relate to surface crack behavior.

Hysteresis energy decrease was also investigated as a measure of damage. For considerations discussed in Section II, all of the area enclosed by cast iron hysteresis loops is attributed to the elastic/plastic bulk response acting over an effective cross-sectional area fraction. Thus, decreases in hysteresis energy with increased cycling should reflect a reduced effective cross-section from surface cracking. A damage parameter based on hysteresis energy drop is given by

$$D = [1 - \Delta W^{*}/\Delta W_{max}] \tag{30}$$

where ΔW^{*} is the hysteresis energy at a given cycle count and ΔW_{max} is the initial hysteresis energy. Figure 24 shows hysteresis energy behavior as a function of cycle ratio for pearlitic gray iron tested at two strain amplitudes. Hysteresis energy behavior may also be influenced by matrix hardening or softening, but the effect should be small for gray iron. This is because high stress concentration factors at graphite flake tips enable the steel matrix to quickly stabilize. This is borne out in Fig. 24 where hysteresis energy drops rapidly at first, then approaches steady state behavior.

The final damage parameter investigated is based on changes in specimen compliance with increased cycling. The unloading modulus at tensile peaks is considered a measure of overall specimen compliance and has already been shown to decrease with increasing stress. For gray iron tested in strain control, the unloading modulus is maximum at the initial tensile peak, and progressively decreases with ensuing cycles. The damage parameter written in terms of the drop in unloading modulus is

$$D = [1 - E_u^*/(E_u)_{max}] \tag{31}$$

where E_u^* denotes the unloading modulus at a given point in life, and $(E_u)_{max}$ is the maximum unloading modulus after the first cycle. Figure 25 shows the unloading modulus as a function of normalized fatigue life for pearlitic gray iron tested at several strain amplitudes. This damage parameter should be relatively insensitive to matrix hardening or softening and mean stress relaxation since neither of these phenomena result in appreciable modulus changes in steel. Therefore, any drop in unloading modulus should relate directly to surface crack behavior. Douglas and Plumtree [30] suggested the use of this parameter to isolate cracking behavior from cyclic hardening or softening.

The proper way to assess which damage parameter is preferred is to evaluate their effect on predicted fatigue life. Before this can be accomplished, the differential equations governing the growth of damage must be determined.

D. Continuum Damage Model

Kachanov [31] originally proposed a theory of brittle rupture based on the concept of material "continuity"; as time passes, damage accumulates, decreasing the proportion of the material available to carry load. Lemaitre and Plumtree [32] modified this theory for fatigue and developed a differential equation for the evolution of damage with each cycle of loading

$$\frac{dD}{dN} = \frac{[1 - D]^{-P}}{(P + 1)\, N_f} \tag{32}$$

where P is a parameter which describes the rate of damage accumulation and is dependent on loading conditions.

For constant amplitude loading, D may be expressed directly in terms of normalized fatigue life, N/N_f. Integration of Eq. (32) between damage limits, 0 to D, and cycle limits, 0 to N, results in

$$[1 - D] = [1 - N/N_f]^{\frac{1}{P + 1}} \tag{33}$$

where $1/(P + 1)$ is the slope of the straight line obtained from plotting log $[1 - D]$ versus log $[1 - N/N_f]$. The damage rate parameter, P, is determined in this way.

To find the relationship between the growth of normalized crack length and applied cycle ratio, Eqs. (28) and (33) are combined to yield

$$1 - \frac{a^*}{a_f} = [1 - N/N_f]^{\frac{1}{P + 1}} \tag{34}$$

Similarly substituting Eq. (33) yields for peak stress behavior

$$\sigma^* = \sigma_{max}[1 - N/N_f]^{\frac{1}{P + 1}} \tag{35}$$

for hysteresis energy behavior

$$\Delta W^{*} = \Delta W_{max}[1 - N/N_f]^{\frac{1}{P+1}} \tag{36}$$

and for unloading modulus behavior

$$E_u^{*} = (E_u)_{max}[1 - N/N_f]^{\frac{1}{P+1}} \tag{37}$$

Figures 26(a)-26(d) show data from a strain-controlled fatigue test where P is determined independently from Eqs. (34)-(37), respectively. It should be noted that the straight line fit is only good over approximately 90 percent of life. The remaining 10 percent represents macrocracking and is not described by this relationship. The selection of N_f should perhaps be defined as the point of deviation from the straight line. Although similar values of P are obtained by any of these methods (within a factor of two), there are some trends which are worth noting. First define P_a, P_σ, P_w and P_u as the damage rate parameters determined from crack growth, stress drop, energy drop and unloading modulus drop, respectively. The approximate ranking of the last three parameters is

$$P_u > P_\sigma > P_w \tag{38}$$

indicating that unloading modulus decreases at a slower rate than either stress or hysteresis energy. It may be argued that unloading modulus is the least sensitive to matrix transient effects (cyclic hardening/

softening and mean stress relaxation) and therefore most closely reflects surface crack behavior. This is borne out because P_u is consistently closer in value to P_a than is P_σ or P_w.

Equations (35)-(37) are also useful in projecting initial values for σ_{max}, ΔW_{max} and $(E_u)_{max}$ from which early matrix transient behavior has been erased. With this information, it should be possible to derive all of the material properties needed for stress/strain simulation from standard strain-controlled fatigue tests. A proposed method is presented in Appendix C.

Socie et al [34] found reasonable correlation between the Smith-Watson-Topper parameter, $\sigma_{max}\varepsilon_a$, and the damage rate parameter, P, as shown in Fig. 27. Damage was described by crack length, stress drop and strain increase (which is a damage parameter used for load control tests). A first order linear regression analysis yielded a relationship of the form

$$P = 2.55\ (\sigma_{max}\varepsilon_a)^{-0.8} \tag{39}$$

Scatter in P can be quite large because it is based on fatigue life, N_f, which can vary by factors of 2 to 5. The analysis, however, is not sensitive to small variations in P; later calculations predict significantly different lives only when P varies greatly.

E. Damage Calculations

The damage calculation for this model must be made on a cycle-by-cycle or block-by-block basis until the damage parameter, D, exceeds a value of 1. Integration of Eq. (32) between damage limits, D_i to D_{i+1}, and cycle limits, 0 to N, results in the expression for damage after the application of N constant amplitude cycles

$$D_{i+1} = 1 - [(1 - D_i)^{P+1} - N/N_f]^{\frac{1}{P+1}} \tag{40}$$

where N_f and P are the cycles to failure and damage rate parameter, respectively, for the constant amplitude cycles, and D_{i+1} and D_i the damage states before and after N constant amplitude cycles. Equation (40) is incrementally applied until D_{i+1} equals or exceeds one. It should be noted that, if P is equal to zero, Eq. (39) simplifies to conventional linear damage analysis given by Miner's Rule (MR), or

$$D_{i+1} = D_i + N/N_f \tag{41}$$

For repeating histories, Brussat [35] has suggested numerical integration techniques for rapid crack growth calculations. These ideas are employed here to reduce the number of damage calculations. The incremental damage growth for each cycle is obtained from Eq. (32)

$$\Delta D = \frac{[1 - D_i]^{P_i}}{(P_i + 1)\, N_{fi}} \tag{42}$$

where D_i is the damage accumulated before the application of the ith cycle of loading; P_i and N_{fi} are the damage rate parameter and cycles to failure, respectively, for the ith cycle of loading. The damage growth rate per block, $\Delta D/\Delta B$, is calculated by assuming damage is fixed at the beginning of the block and summing incremental damage growth for each cycle.

$$\frac{\Delta D}{\Delta B} = \sum_{1}^{K} \Delta D \tag{43}$$

Combining Eqs. (42) and (43) results in the following:

$$\frac{\Delta D}{\Delta B} = \sum_{i=1}^{K} \frac{[1 - D]^{-P_i}}{(P_i + 1)\, N_{fi}} \tag{44}$$

The reciprocal damage growth rate versus damage curve is then formed using 20 increments between D = 0 and D = 1. Simpson's Rule was used to numerically integrate this curve to obtain loading blocks to failure, B_f.

$$B_f = \int_0^1 \frac{\Delta B}{\Delta D}\, dD \tag{45}$$

Similar numerical integration procedures were used by Galliart [35] and Socie [36] for crack growth calculations.

F. Test Results

A limited series of strain-controlled variable loading tests were conducted to evaluate the continuum damage model. Six loading histories were chosen and are illustrated in Fig. 28. Included are short repeating complex loadings and two level block loadings traditionally used for evaluating damage methods. Material properties described by Eqs. (27) and (34) are used in conjunction with Eqs. (40) and (41) which describe damage accumulation. The cyclic stress/strain response model presented in Section II was used for determining mean stresses.

Experimental and predicted fatigue lives are given in Table 2 in terms of blocks to failure for histories A through D. The damage approach always gives roughly equivalent, but slightly shorter lives than those predicted by Miner's linear damage rule for short repeating histories such as these. This is because the large cycles repeat so often that they are essentially constant amplitude, and the damage approach and Miner's Rule must give equivalent lives under constant amplitude loading.

Test results and predictions for histories E and F are reported in terms of residual cycles to failure, N_2, and are also given in Table 2. The continuum damage model more correctly assesses the sequence effect than does Miner's Rule. It should be noted that both methods account for mean stresses identically; differences in predictions must be attributed to the damage models themselves.

Differences between estimates based on Miner's Rule and the continuum damage model may be attributed to the damage rate parameter, P; in fact,

large differences occur only when the P varies greatly. To access the dependence of the predictions on P, a further analytical evaluation of the traditional hi-lo block sequence is useful. Consider a loading sequence in which N_1 repetitions of a cycle with fatigue life, N_{f1}, and damage rate parameter, P_1, are first applied. How many repetitions N_2, of a cycle with corresponding N_{f2} and P_2 can be withstood until failure? The continuum damage model predicts that

$$N_2 = N_{f2}[1 - (N_1/N_{f1})]^{R_P} \tag{46}$$

where

$$R_P = \frac{P_2 + 1}{P_1 + 1} \tag{47}$$

The total damage, D_{MR}, predicted by Miner's linear damage rule when failure is detected by the continuum damage model can be written

$$\begin{aligned} D_{MR} &= (N_1/N_{f1}) + (N_2/N_{f2}) \\ &= (N_1/N_{f1}) + [1 - (N_1/N_{f1})]^{R_P} \end{aligned} \tag{48}$$

Figure 29 shows D_{MR} plotted versus applied cycle ratio, N_1/N_{f1}, for varying levels of $R_P = (P_2 + 1)/(P_1 + 1)$. The maximum discrepancies between Miner's Rule and the continuum damage model increase with increasing R_P. Also, for a given ratio, R_P, there exist critical cycle ratios

$$(N_1/N_{f1})_{critical} = 1 - R_P^{\frac{1}{1 - R_P}} \tag{49}$$

and

$$(N_2/N_{f2})_{critical} = R_P^{\frac{R_P}{1 - R_P}} \tag{50}$$

which yields a minimum Miner's Rule prediction

$$(D_{MR})_{min} = 1 - R_P^{\frac{1}{1 - R_P}} + R_P^{\frac{R_P}{1 - R_P}} \tag{51}$$

As an example, two loading levels with corresponding cycles to failure N_{f1} equal to 10^3 and N_{f2} equal to 10^6 were chosen. If P_1 and P_2 are equal to 2 and 29, respectively (i.e., $R_P = 10$), the minimum Miner's damaged at failure, $(D_{MR})_{min}$ equal to .3, occurs when N_1 equal to 226 cycles and N_2 equal to 77,426 cycles are consecutively applied.

While the above example clearly demonstrates sequence effects in hi-lo loading not recognized by Miner's linear damage rule, what happens when two loading levels are mixed so that failure occurs in more than one block? In the following example, the critical cycle ratios, $(N_1/N_{f1})_{critical}$ and $(N_2/N_{f2})_{critical}$, are scaled down equally to yield applied cycle ratios per block

$$\begin{aligned} (N_1/N_{f1})_{BLOCK} &= F_S(N_1/N_{f1})_{critical} \\ (N_2/N_{f2})_{BLOCK} &= F_S(N_2/N_{f2})_{critical} \end{aligned} \tag{52}$$

where F_S is a scalar less than one. The scaling factor, F_S, was varied so that the continuum damage model predicted failures between 1 and 1000 blocks, and the corresponding Miner's damage sum noted. The results are summarized in Fig. 30. They imply that Miner's damage sum increases as blocks to failure increase, but reaches a saturation level above which further load interspersion causes no further increase in Miner's damage sum. It should be noted that while this is a highly specialized case (i.e., minimum linear damage condition), it may have interesting implications to fatigue testing. Under the proper conditions of loading levels and degree of load mixing, failures of block loadings might be approximated by equivalent hi-lo sequences. For example, the classic engine cycle (a large startup cycle followed by many working cycles) could possibly be tested as a defined number of startup cycles followed by working loads until failure, certainly a more efficient test. Further investigation into other sets of load conditions is needed before this equivalency can be generally accepted.

Both examples demonstrate that the ratio $R_P = (P_2 + 1)/(P_1 + 1)$ is the controlling factor in the differences between Miner's Rule and the continuum damage model and that values of P needed to cause large life discrepancies are easily within what might be expected.

G. Discussion

The proposed continuum damage model has been shown to correctly assess the effect of loading sequence in gray iron and thereby give better life

estimates. It models the behavior of the actual failure mechanism, the growth and development of multiple crack systems, rather than crack initiation. It requires simple testing procedures already in use for wrought metals and little extra time and effort than is now expended for linear damage analysis.

Four physically-based measures of damage have been investigated. These were crack growth, stress drop, hysteresis energy drop, and unloading modulus drop. For the pearlitic gray iron studied, all of the parameters yielded roughly equivalent values of the damage rate parameter, P, and could be used interchangeably; however, this is probably not true of all cast irons. In general, the damage parameter which most closely reflects crack behavior and is least affected by matrix transient behavior should be chosen. The author's personal preference for gray iron is to use unloading modulus drop because it seems to ignore the effects of matrix transient behavior, and to more closely represent cracking behavior. Detailed observation of this parameter in steels might extend the usefulness of continuum damage ideas to wrought metals.

Because the fatigue life of gray iron is controlled by crack growth, the effect of specimen size must be addressed. All of the previously mentioned tests on pearlitic gray iron were performed on 10 mm diameter axial smooth specimens. To study size effect, two sets of new specimens were prepared, one with twice and the other with half the cross-sectional area of the original specimens. A series of completely-reversed strain-controlled tests was then conducted to evaluate the effect of specimen size on fatigue life and the aforementioned damage parameters. Unfortu-

nately, no data could be obtained for the large specimens at strains less than .003 due to an insufficient difference between the grip end and gage diameters. In general, however, the large specimens withstood more strain cycles until failure (95 percent drop in tensile load) than did the small specimens. This is believed to be due to increased large scale crack growth in the larger specimen. A plot of peak tensile stress versus normalized cycles to failure (Fig. 31) illustrates this phenomenon. Data for the large specimen exhibit increased inflection in stress drop behavior which is believed to mark the transition between small and large crack growth. Determination of the relative rates of stress-drop for different sized specimens from this normalized plot can be misleading. Apparently, the stress in the large specimen drops at a faster rate than the small specimen. This is not really the case. Figure 32, which shows peak tensile stress versus applied cycles for the same two specimens, demonstrates nearly equivalent rates of stress drop per cycle. The apparent difference seen in Fig. 31 is attributed to the difference in N_f due to specimen size.

IV. TRANSIENT STRESS/STRAIN RESPONSE

A. Background

Observing the transient stress/strain response of pearlitic gray iron during strain-controlled constant amplitude cycling, the following trends were identified.

(1) For negative mean strains, the maximum stress decreases arithmetically and the minimum stress increases arithmetically with increasing cycles,

(2) For completely-reversed loading, the maximum stress decreases arithmetically and the minimum stress remains constant with increasing cycles, and

(3) For positive mean strains, both the maximum and minimum stresses decrease arithmetically with increasing cycles.

These trends are inconsistent with either cyclic hardening/softening or mean stress relaxation commonly observed in steels. While undoubtedly present in some degree (the matrix is, after all, steel), neither can fully explain gray iron transient behavior. The previous discussion on hysteresis energy response demonstrated that cyclic hardening or softening in gray iron occurs rapidly due to severe stress concentrations at graphite flake tips. Also, the energy symmetry of gray iron would tend to

preclude the presence of mean stress relaxation under completely reversed loading. The predominant cause of this behavior must be due to surface crack growth. A model for estimating the stress/strain response of gray iron as a function of accumulated damage follows.

B. Transient Stress/Strain Response Model

As fatigue cracks grow from the surface into the specimen, it is reasonable to assume a further reduction in the fraction of cross-sectional area available to transmit tensile stress. Therefore, A_{eff} may be considered a function of not only material properties and maximum stress, but also accumulated fatigue damage. The following relationship is then proposed.

$$A_{eff}^{*} = (1 - D)(A_{eff})_{max} \tag{53}$$

where A_{eff}^{*} = instantaneous area fraction,

$(A_{eff})_{max}$ = area fraction at zero damage, and

D = fatigue damage

This relationship is consistent with Kachanov's original damage hypothesis; fatigue damage is a measure of the cross-sectional area available to carry load. The evolution of damage with applied cycles for this material was previously described.

In addition to the change in A_{eff}, the crack closure stress, σ_{cc}, must be modified to account for changing specimen compliance. As cracks grow, the strain at which they start to close reduces; in other words, the cracks remain open over a greater portion of the overall strain range. The following estimate of this behavior is then offered.

$$\sigma_{cc} = Q'[(1 - D)\varepsilon_{max} - \varepsilon]^{q'} \tag{54}$$

The new properties Q' and q' must be solved for at each damage level, D, but the solution is identical to that discussed in Section II. F. for Q and q.

The implications of this simple model are that peak stress, hysteresis energy, and unloading modulus decrease at the same rate with increased cycling. While not strictly true, as demonstrated by Eq. (38), reasonable first estimates of transient response can be obtained for selected cases in the life region where microcrack growth is dominant.

C. Test Results

Figures 33-35 show experimental and predicted transient stress/strain response at selected damage levels for strain-controlled constant amplitude cycling. Damage was determined by the stress drop method so that peak tensile stresses are always nearly correct. It is important then to see how well the model predicts the overall shape and compressive peak stress for each hysteresis loop.

For completely-reversed loading, the model does reasonably well as seen in Fig. 33. When the mean strain of the cycle is nonzero, however, the match between predicted and actual response becomes worse with increased cycling as demonstrated in Figs. 34 and 35. In the general case, greater deviation from completely-reversed cycling results in greater discrepancy between predicted and experimental response. The symmetrical bulk response seems to be affected by mean stress relaxation in these cases similar to wrought metals. Transition of the bulk response up (for negative mean strains) or down (for positive mean strains) with increased cycling would tend to account for these discrepancies. A mean stress relaxation model for cast iron is, therefore, desirable but beyond the scope of this thesis.

Since the transient model works well for completely-reversed strain cycling, its effect on the fatigue predictions for histories A through D in Fig. 28 can be evaluated. For these histories, the completely-reversed outer loops control the overall response. Damage, calculated after each block, modifies the stress/strain response of the next block causing changes in P and N_f for each hysteresis loop. The process was repeated until the continuum damage model predicted failure for each history. The results shown in Table 2 indicate that, for these types of histories, the details of transient stress/strain behavior are not particularly important since they don't appreciably change the fatigue predictions. Further research with other types of histories is needed to determine the general importance of accurately tracking transient cyclic deformation of cast iron.

D. Discussion

A simple modification of the stress/strain response model presented in Section II allows reasonable prediction of gray iron transient response for completely-reversed strain cycling. For nonzero mean loading, the inclusion of mean stress relaxation effects is deemed necessary. Additional research needs to be conducted before the applicability of this model can be extended to include the full range of cast irons.

V. SUMMARY

The cyclic deformation and low cycle fatigue behavior of cast iron (particularly gray iron) is controlled by the growth and development of multiple crack systems. The use of initiation-based procedures in this life regime is incorrect.

A practical stress/strain response model for cast iron was presented. Total response is composed of symmetrical elastic/plastic bulk behavior and nonlinear responses attributed to internal graphite constraint and surface crack growth. Because hysteresis energy behavior is essentially symmetrical (even though stress/strain response is not), these nonlinear responses may, for all practical purposes, be considered elastic.

The proposed continuum damage model has been shown to properly account for sequence effects in gray iron. Damage, a state variable reflecting surface cracking development, may be alternately measured with any of several bulk stress/strain parameters.

Of those evaluated, unloading modulus at the peak tensile stress seems to most closely represent surface behavior and is thus preferred. Maximum error in the application of Miner's linear damage to gray iron is observed for traditional hi-lo sequences. On the other hand, both damage rules predict comparable results for short repeating histories which, in most cases, are equivalent to constant amplitude loading. Analytical studies of cycle interspersion have shown that, in specialized cases, block loading may be evaluated with equivalent hi-lo sequences. The effect of

specimen size on the deformation and fatigue behavior of the pearlitic gray iron tested was considered small. Finally, continuum damage analysis requires little extra work than procedures now in use.

The simple transient stress/strain response model presented in this thesis works well for completely-reversed strain cycling in the life region dominated by microcracking. Mean stress relaxation effects must be added to the bulk response before it is generally applicable to other types of loading.

VI. RECOMMENDATIONS

1. The cyclic deformation and damage models presented in this thesis should be evaluated with different materials to determine the range of applicability.

2. Successful finite element analysis of iron castings requires extension of the cyclic deformation model to stress states of more than one dimension.

3. The continuum damage model should be evaluated with other loading types including random histories.

4. Detailed investigation of unloading modulus as a measure of damage in steel may help extend continuum damage analysis to wrought materials.

TABLE 1. STRESS/STRAIN PROPERTIES

	Gray Iron	CG Iron	Nodular Iron
Elastic Tangent Modulus, E_0 (MPa)	119,550	145,021	181,070
Tensile Secant Slope, m_T	-400	-120	-100
Tensile Strength Coefficient, K_T (MPa)	430	780	1,050
Tensile Strain Hardening Exponent, n_T	.115	.111	.15
Compressive Secant Slope, m_C	-100	-60	-30
Compressive Strength Coefficient, K_C (MPa)	820	920	1,100
Compressive Strain Hardening Exponent, n_C	.115	.111	.15
Unloading Modulus Parameter, m_u	-185	-85	0

TABLE 2. LIFE PREDICTIONS AND TEST RESULTS

Block History	Experimental Life in Blocks	Miner's Rule Prediction	Damage Model Prediction	Damage Model with Transient
A	93	181	116	105
B	169	101	77	68
C	323	212	188	165
D	226	210	188	165
E	95,000*	285,000	55,000	-
F	550*	343	470	-

* Residual life, N_2

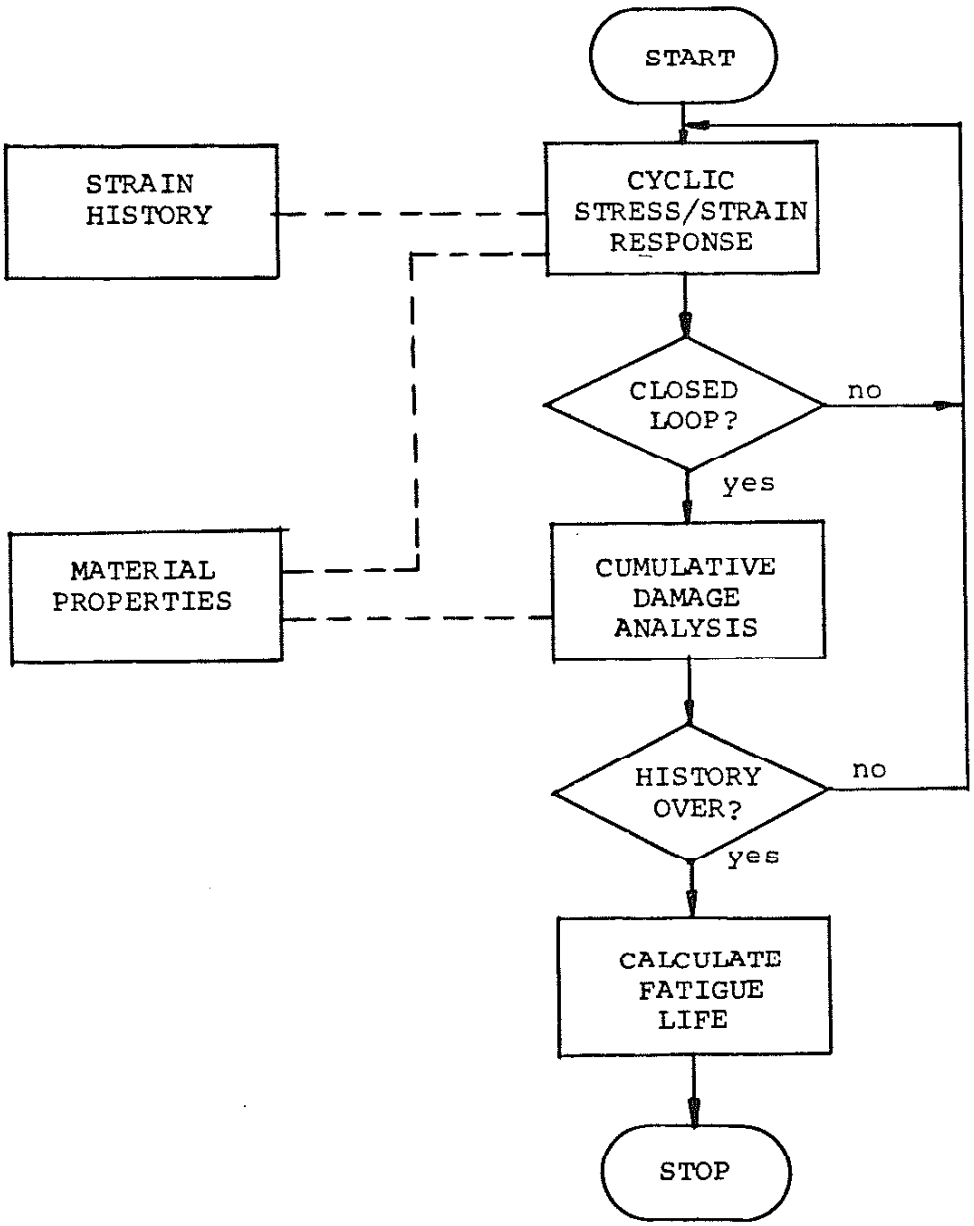

FIG. 1 FLOW CHART OF FATIGUE PREDICTION PROCEDURE FOR CAST IRON

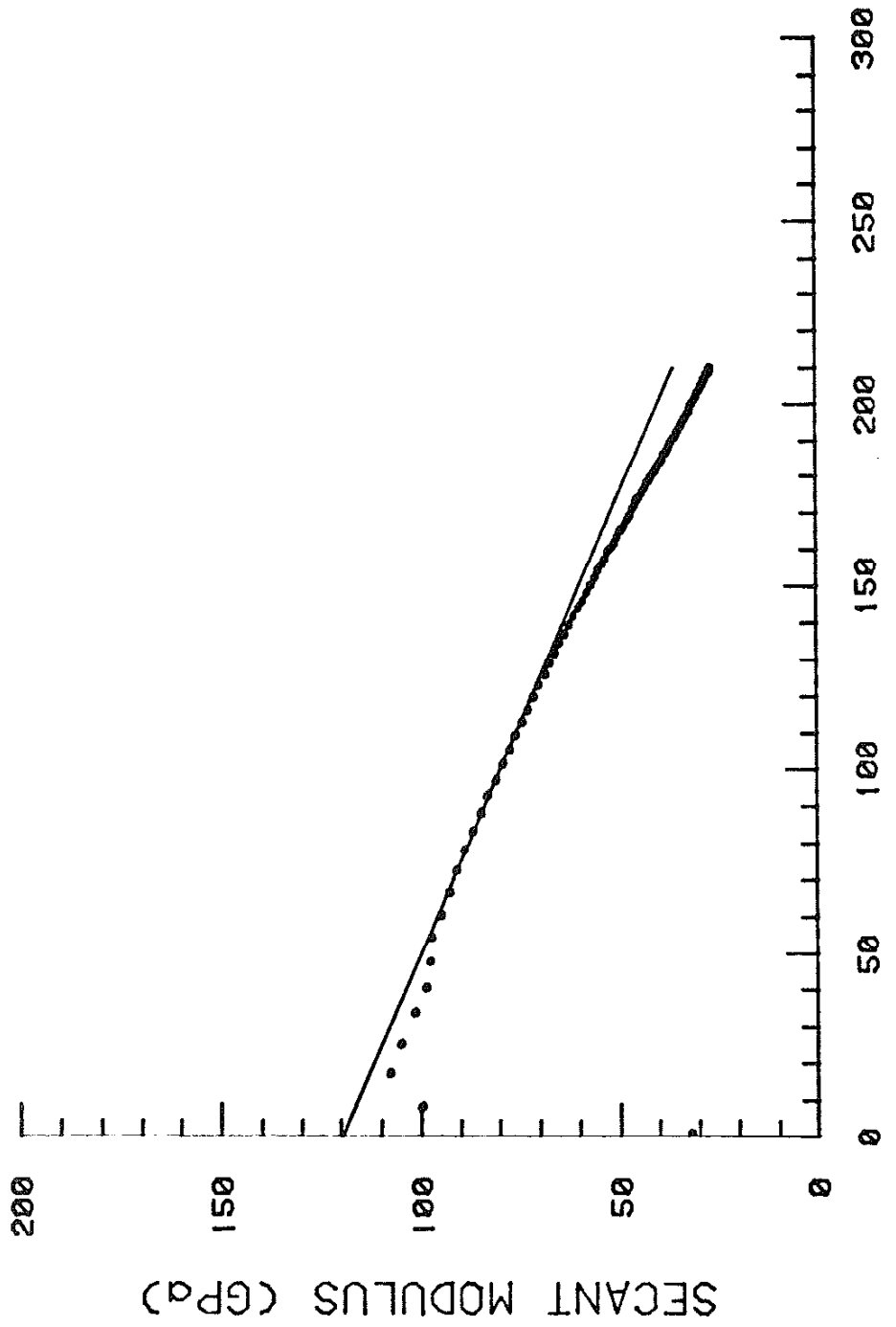

FIG. 2 SECANT MODULUS VERSUS STRESS FROM THE MONOTONIC STRESS/STRAIN CURVE OF GRAY IRON

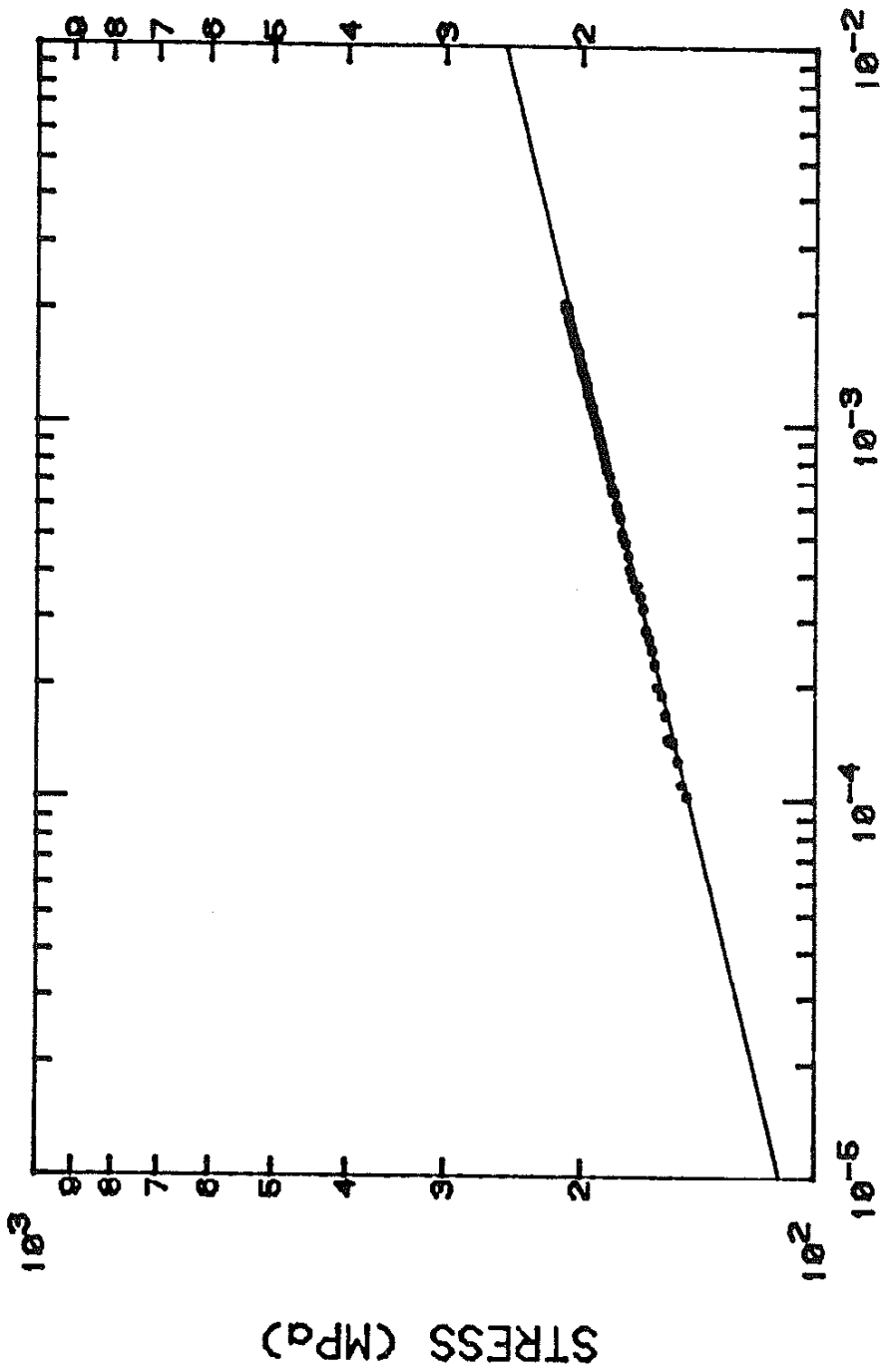

FIG. 3 STRESS VERSUS REMAINING PLASTIC STRAIN FROM THE MONOTONIC TENSILE STRESS/STRAIN CURVE OF GRAY IRON

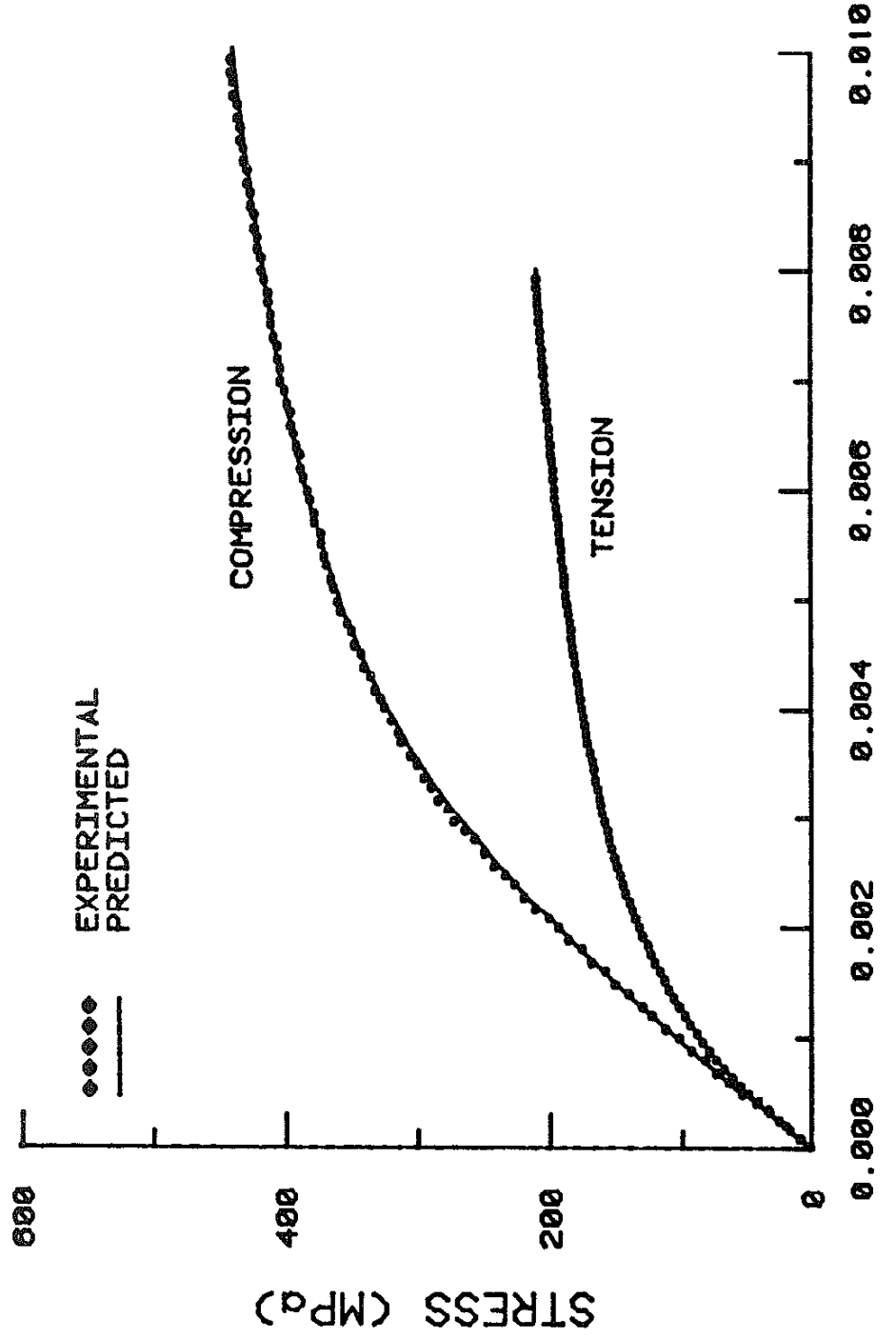

FIG. 4 EXPERIMENTAL AND PREDICTED MONOTONIC STRESS/STRAIN RESPONSE OF GRAY IRON

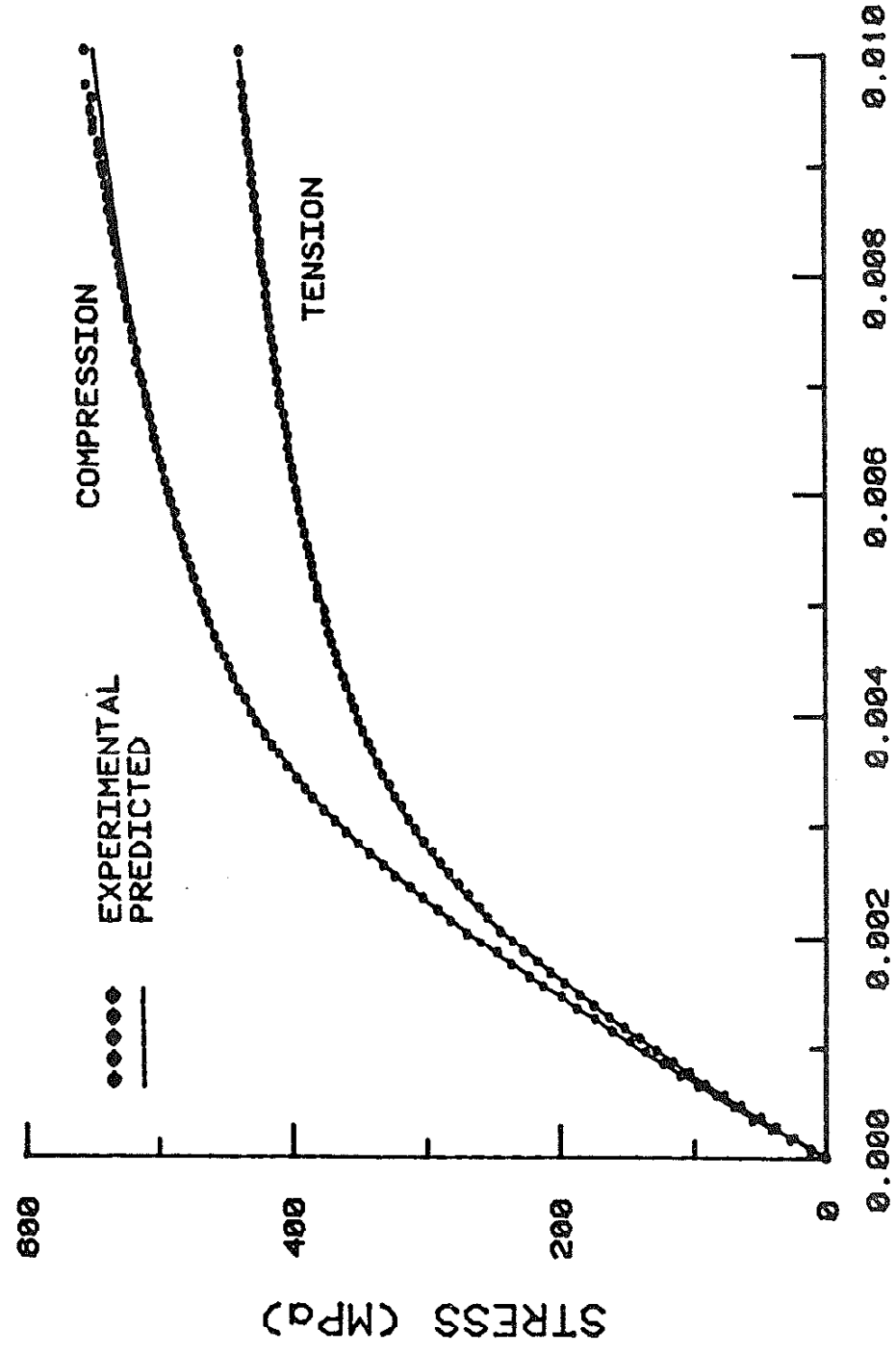

FIG. 5 EXPERIMENTAL AND PREDICTED MONOTONIC STRESS/STRAIN RESPONSE OF CG IRON

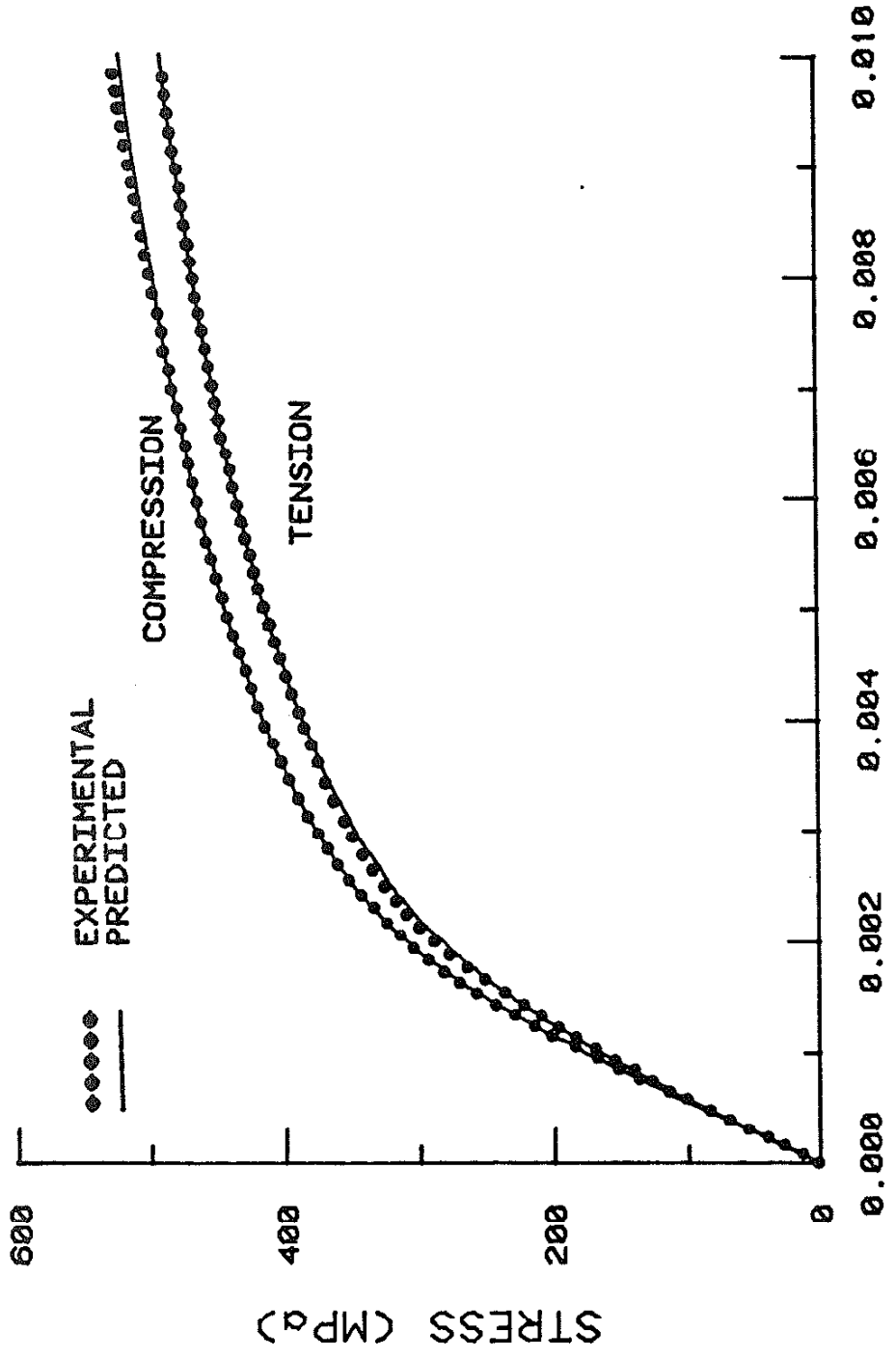

FIG. 6 EXPERIMENTAL AND PREDICTED MONOTONIC STRESS/STRAIN RESPONSE OF NODULAR IRON

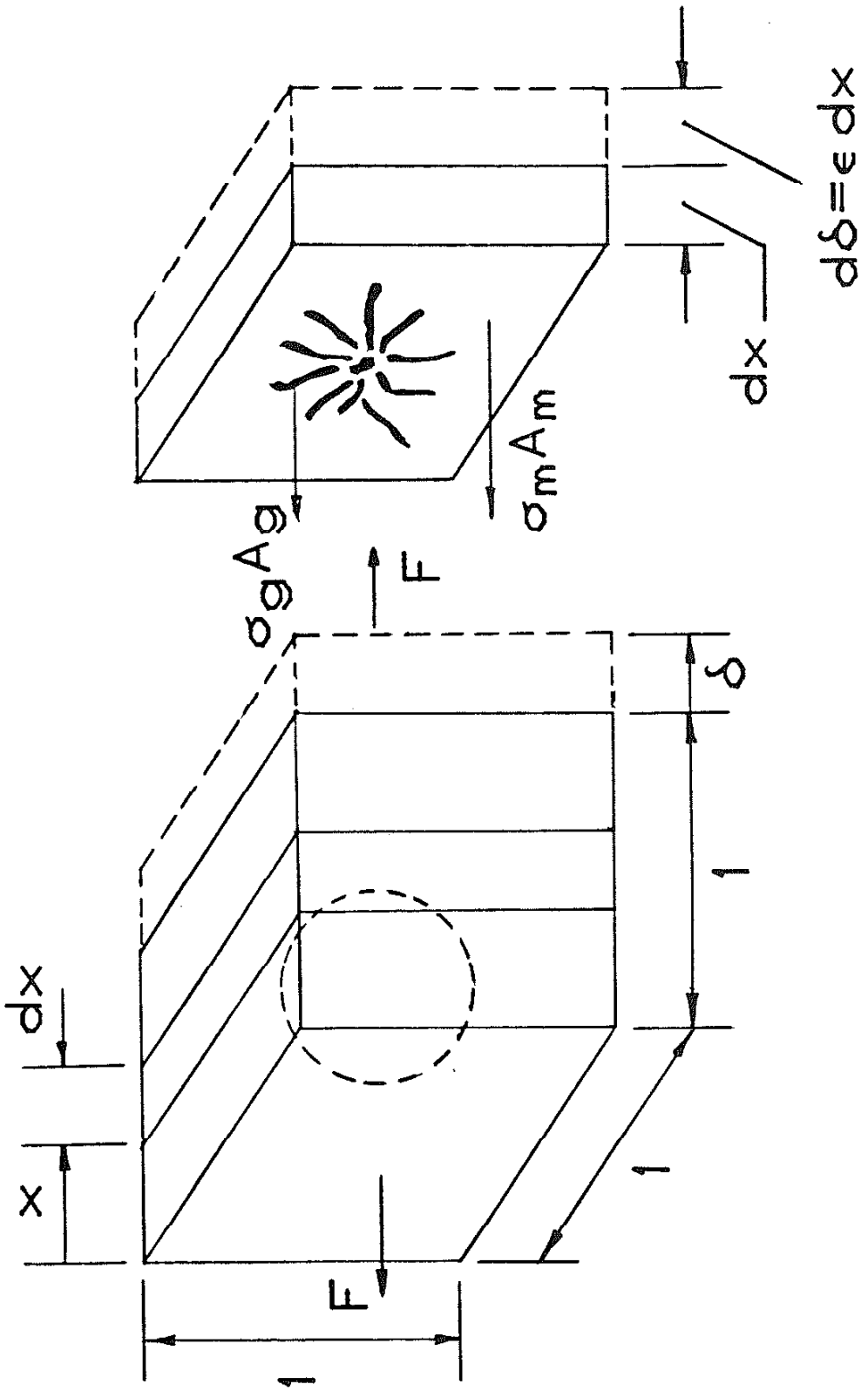

FIG. 7 MECHANICS OF MATERIALS REPRESENTATION OF A UNIT CUBE OF GRAY IRON

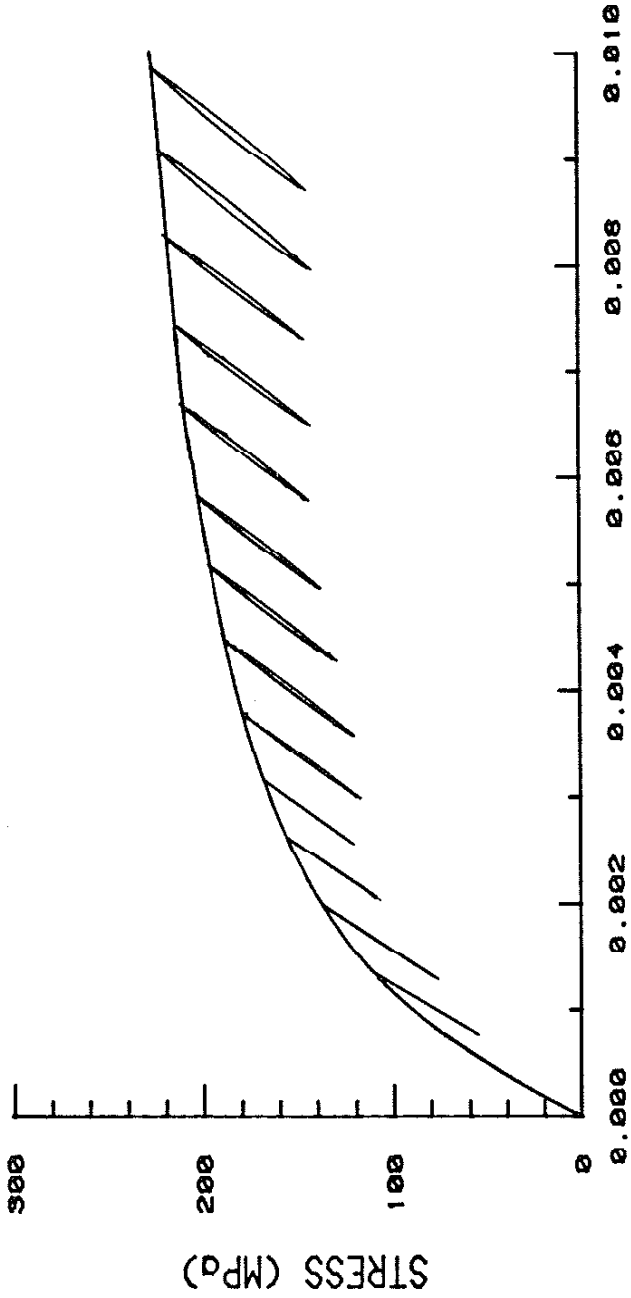

FIG. 8 INCREMENTAL TENSION TEST SHOWING DECREASE IN UNLOADING MODULUS WITH INCREASING TENSILE STRESS

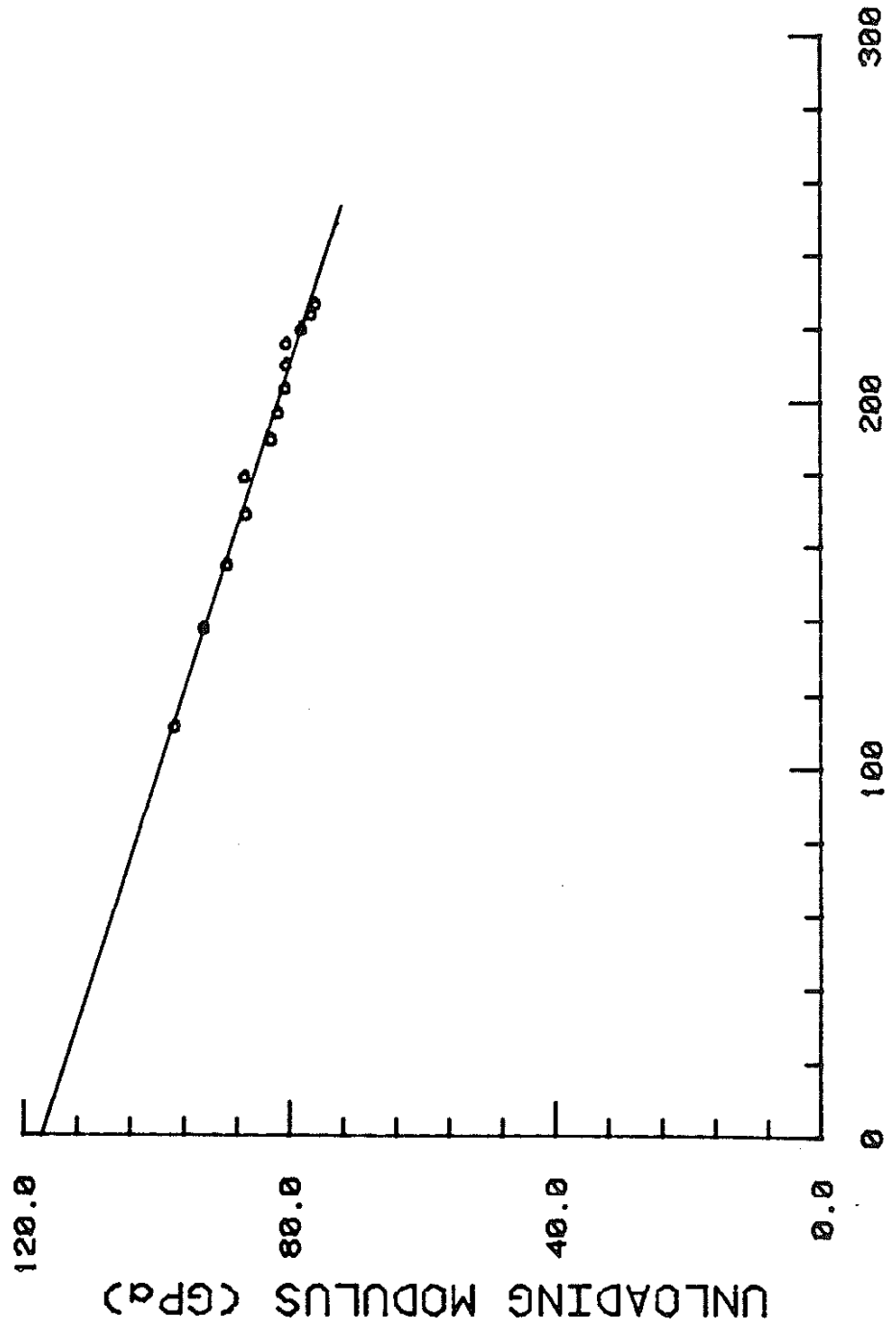

FIG. 9 UNLOADING MODULUS VERSUS TENSILE STRESS FOR INCREMENTAL TENSION TEST OF GRAY IRON

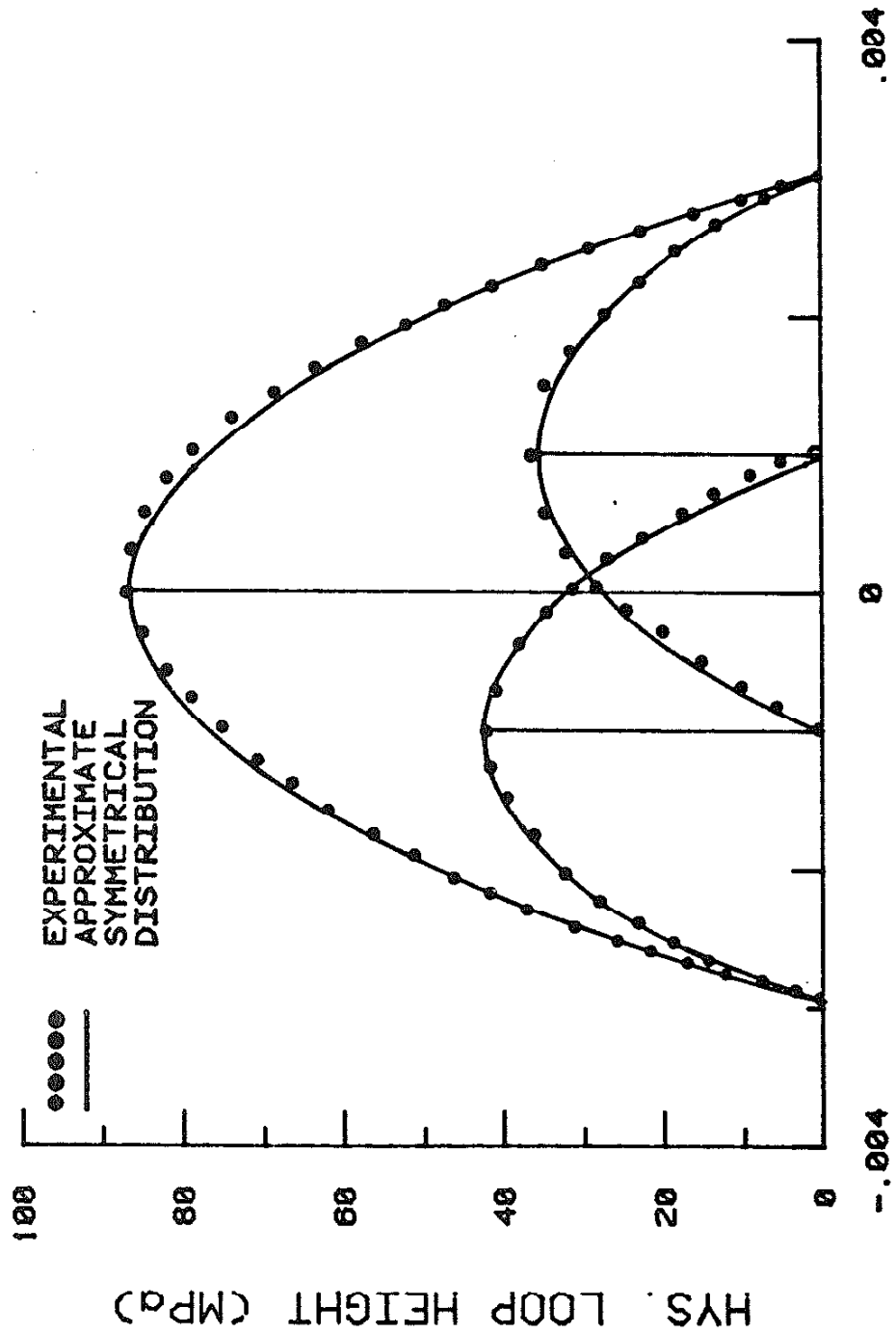

FIG. 10 HYSTERESIS LOOP HEIGHT VERSUS STRAIN FOR SEVERAL GRAY IRON HYSTERESIS LOOPS SHOWING SYMMETRY OF HYSTERESIS AREA WITH RESPECT TO MEAN STRAIN

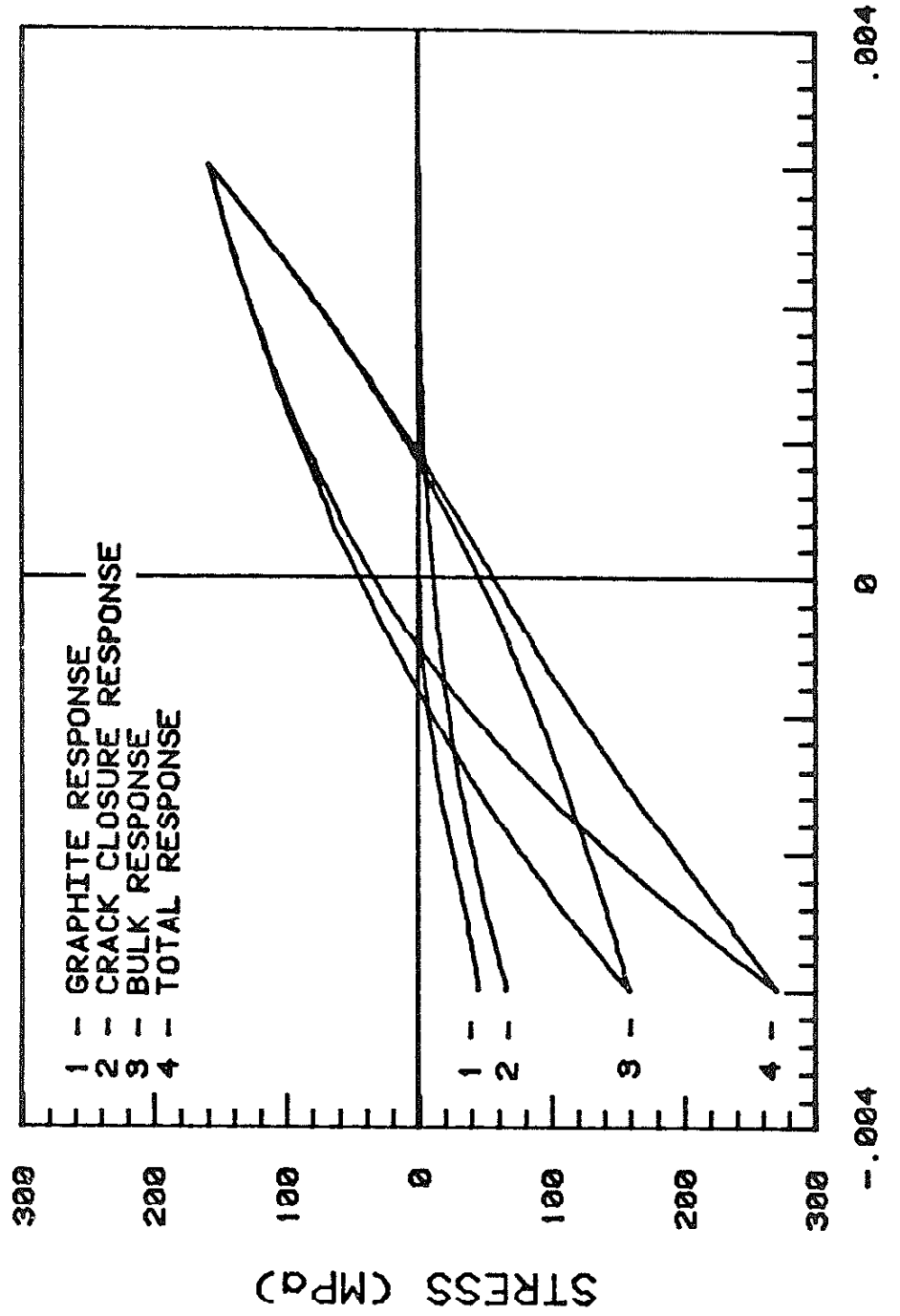

FIG. 11 INDIVIDUAL AND TOTAL COMPONENTS OF STRESS/STRAIN RESPONSE FOR A REPRESENTATIVE GRAY IRON HYSTERESIS LOOP

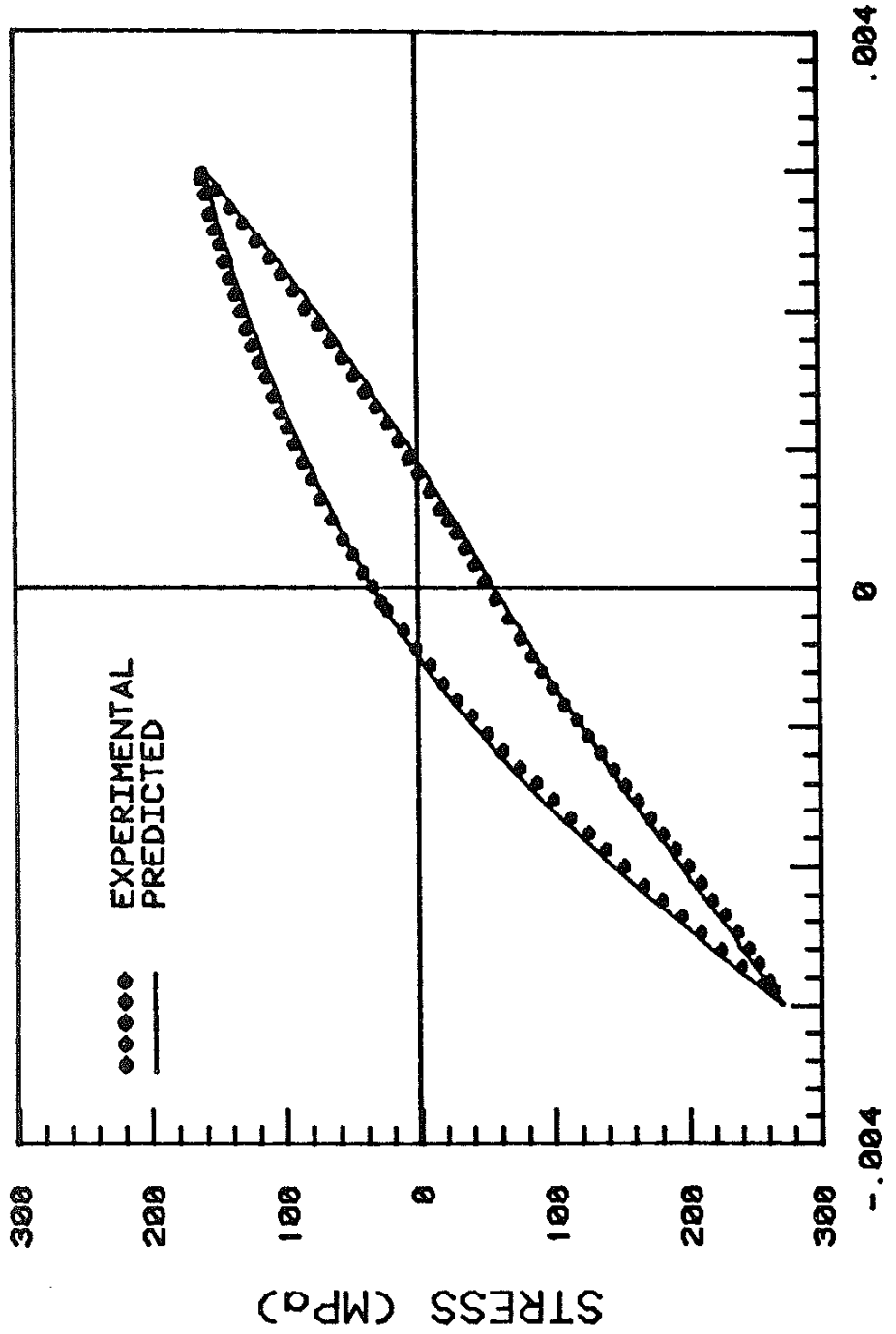

FIG. 12 EXPERIMENTAL AND PREDICTED CYCLIC STRESS/STRAIN RESPONSE OF GRAY IRON; $\varepsilon_{max} = .003$, $\varepsilon_{min} = -.003$

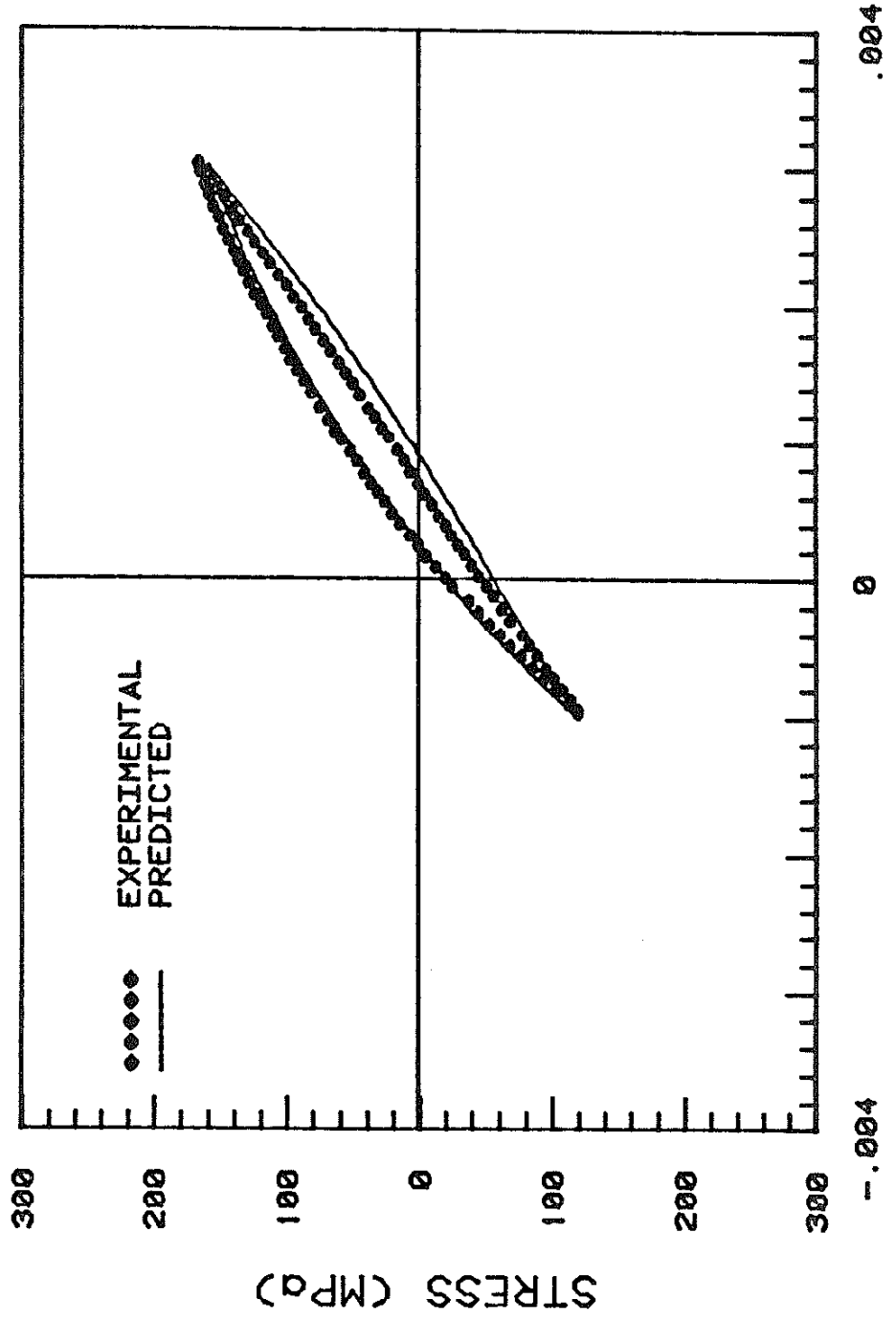

FIG. 13 EXPERIMENTAL AND PREDICTED CYCLIC STRESS/STRAIN RESPONSE OF GRAY IRON; $\varepsilon_{max} = .003$, $\varepsilon_{min} = -.001$

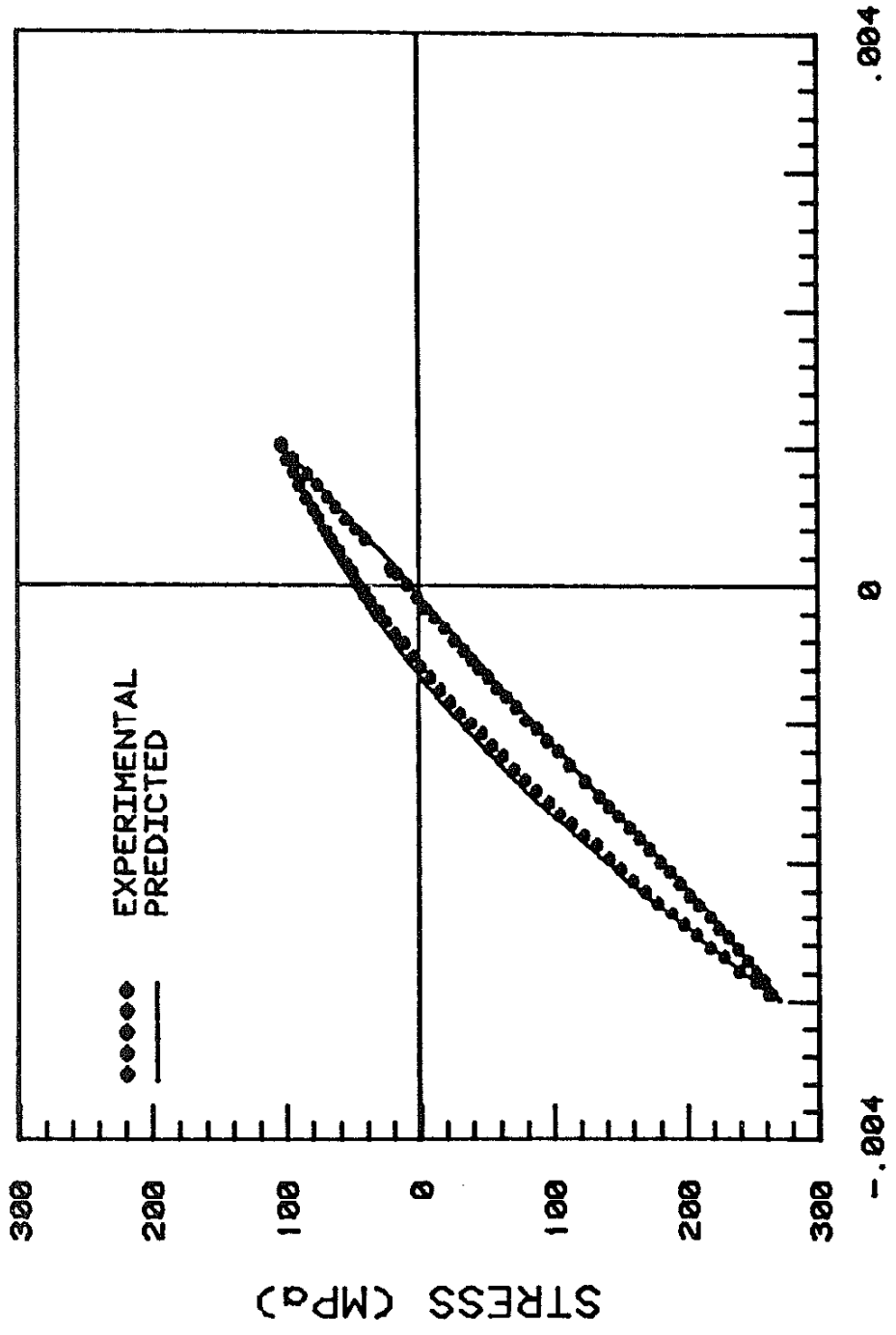

FIG. 14 EXPERIMENTAL AND PREDICTED CYCLIC STRESS/STRAIN RESPONSE OF GRAY IRON; $\varepsilon_{max} = .001$, $\varepsilon_{min} = -.003$

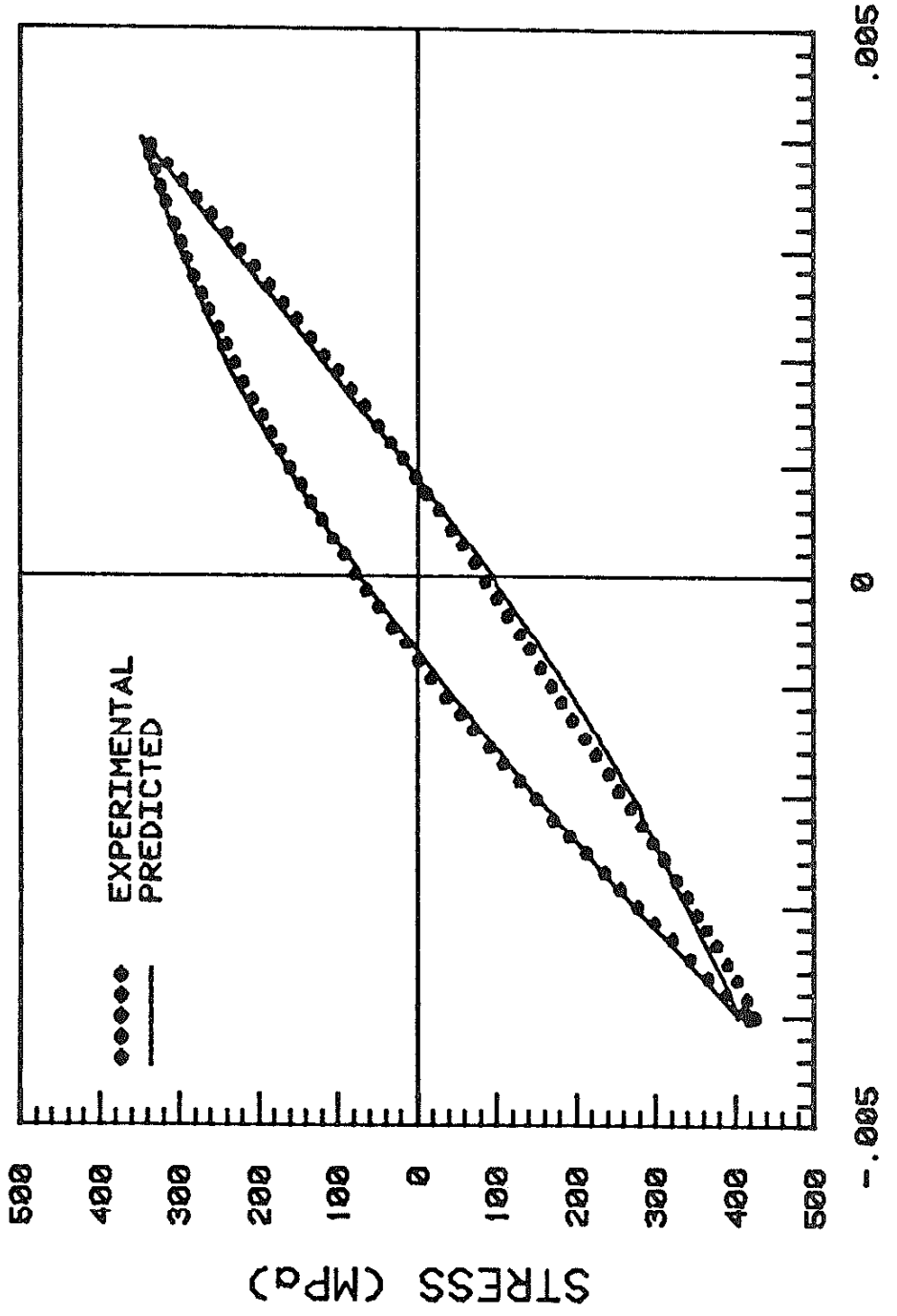

FIG. 15 EXPERIMENTAL AND PREDICTED CYCLIC STRESS/STRAIN RESPONSE OF CG IRON; $\varepsilon_{max} = .004$, $\varepsilon_{min} = -.004$

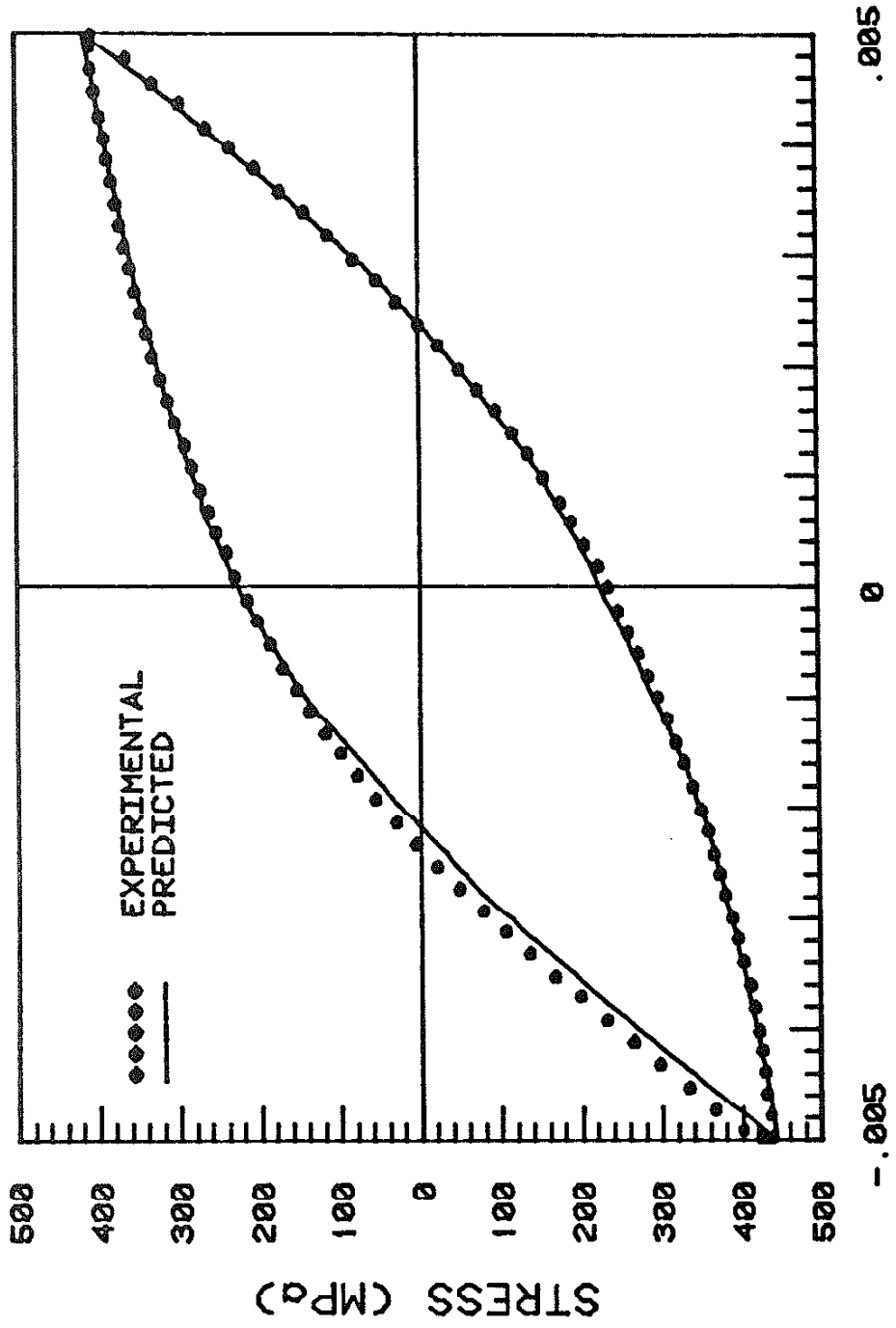

FIG. 16 EXPERIMENTAL AND PREDICTED CYCLIC STRESS/STRAIN RESPONSE OF NODULAR IRON; $\varepsilon_{max} = .005$, $\varepsilon_{min} = -.005$

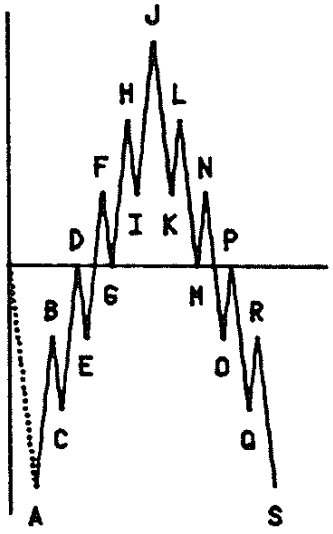

	STRAIN	ACTUAL STRESS	PRED. STRESS	STRESS ERROR
A	-.0031	-275	-271	4
B	-.0010	-49	-40	9
C	-.0020	-160	-151	9
D	.0	34	30	4
E	-.0010	-66	-67	1
F	.0010	93	82	11
G	.0	22	-4	26
H	.0020	139	123	16
I	.0010	59	40	19
J	.0031	166	161	5
K	.0010	19	7	12
L	.0020	97	89	8
M	.0	-45	-53	8
N	.0010	39	33	6
O	-.0010	-114	-115	1
P	.0	-15	-18	3
Q	-.0020	-196	-185	11
R	-.0010	-82	-74	8
S	-.0031	-275	-271	4

STRAIN HISTORY 'A'

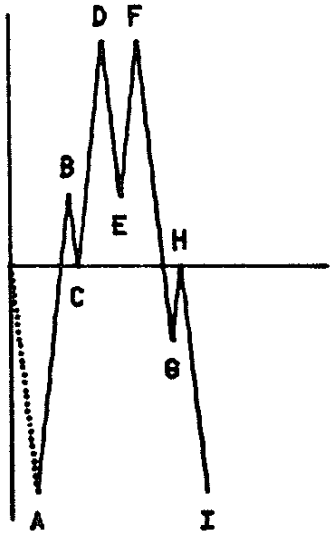

	STRAIN	ACTUAL STRESS	PRED. STRESS	STRESS ERROR
A	-.0031	-288	-271	17
B	.0010	102	82	20
C	.0	11	-4	15
D	.0031	178	161	17
E	.0010	23	7	16
F	.0031	178	161	17
G	-.0010	-123	-115	8
H	.0	-17	-18	1
I	-.0031	-288	-271	17

STRAIN HISTORY 'B'

FIG. 17 LOAD HISTORIES FOR VARIABLE AMPLITUDE STRESS/STRAIN RESPONSE TESTS

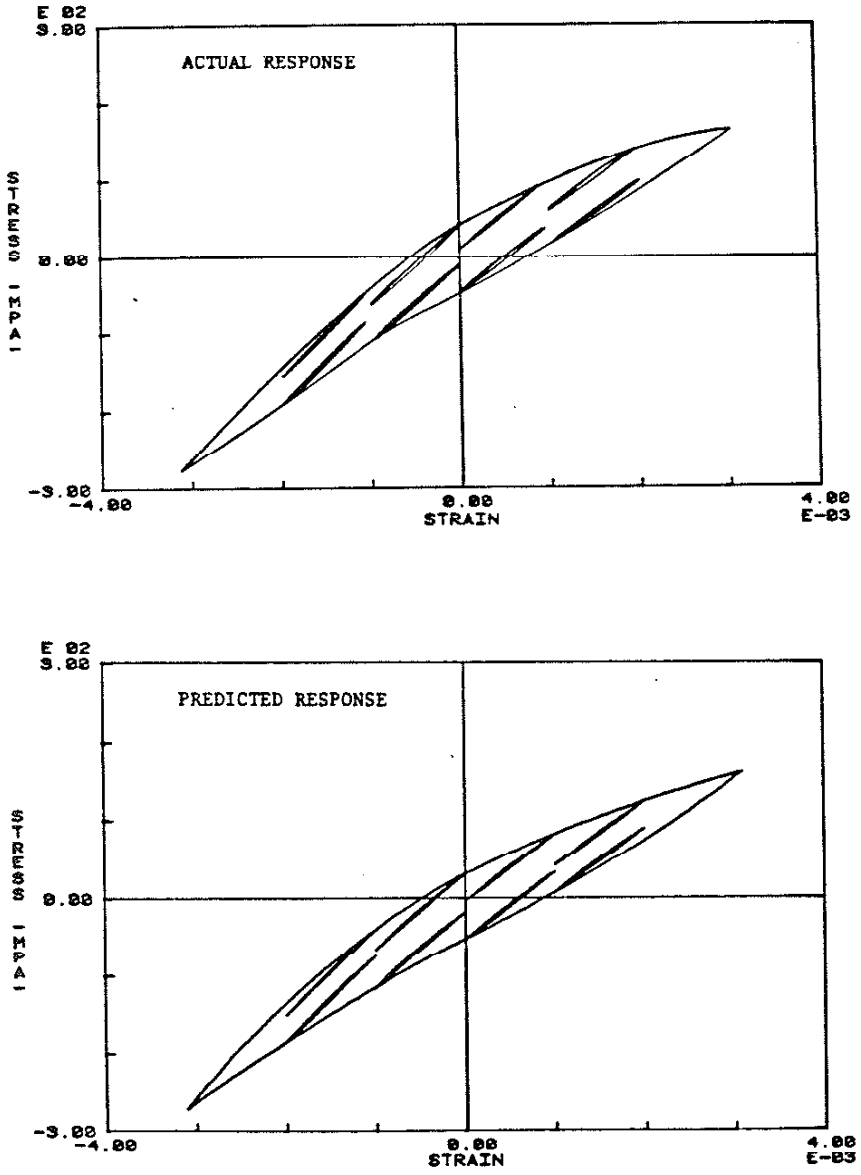

FIG. 18 EXPERIMENTAL AND PREDICTED CYCLIC STRESS/STRAIN RESPONSE OF GRAY IRON SUBJECTED TO HISTORY A

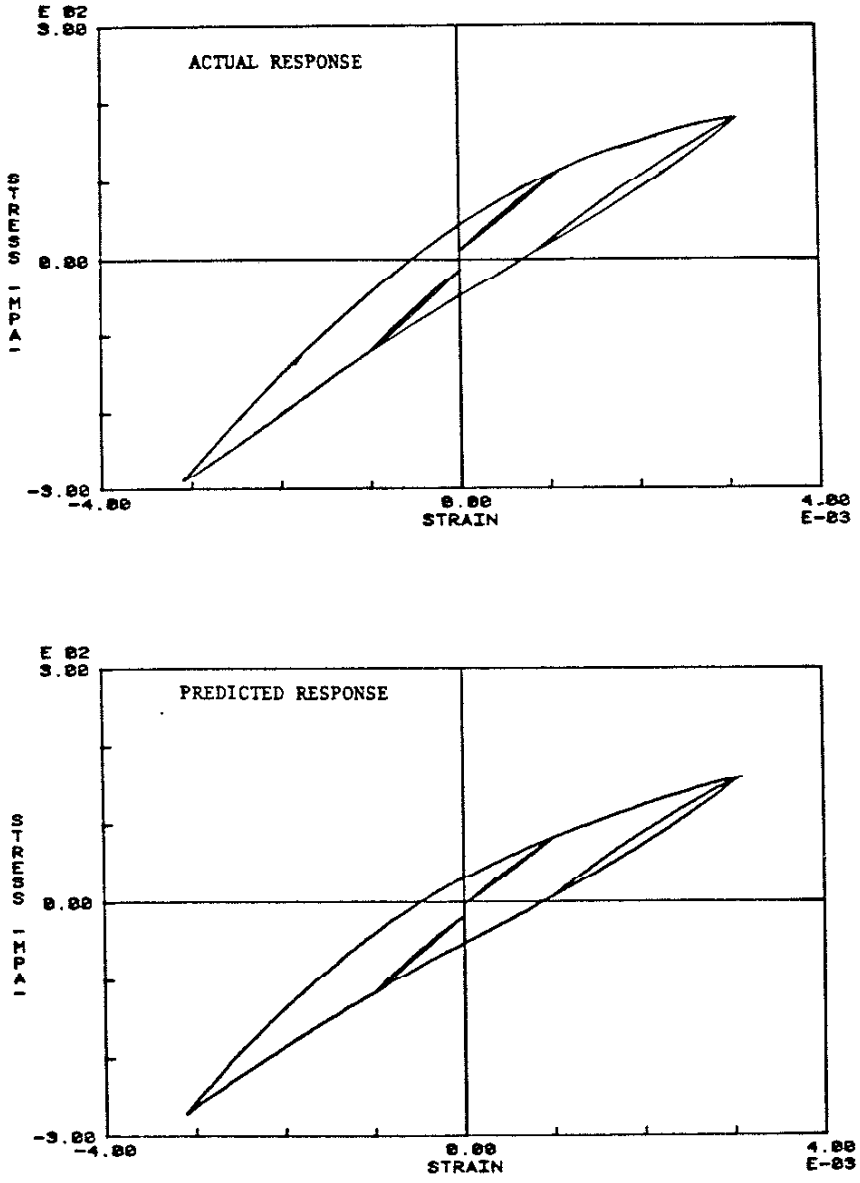

FIG. 19 EXPERIMENTAL AND PREDICTED CYCLIC STRESS/STRAIN RESPONSE OF GRAY IRON SUBJECTED TO HISTORY B

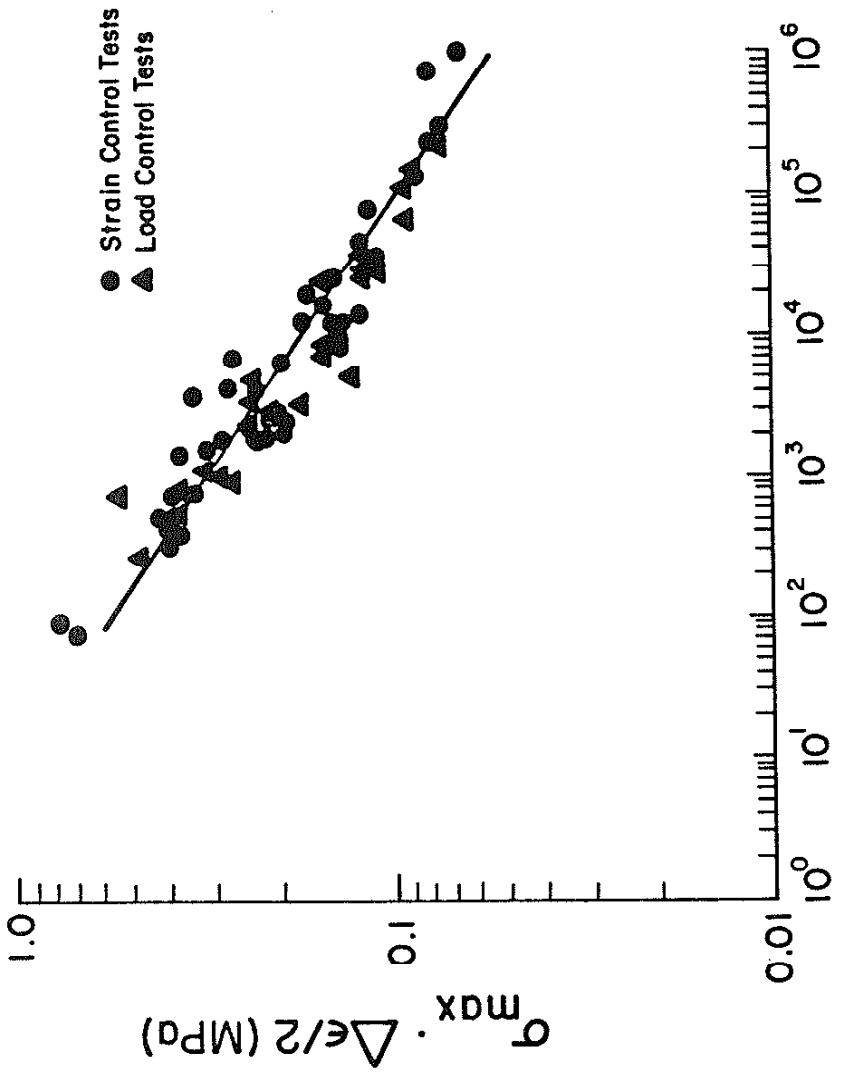

FIG. 20 FATIGUE DATA FOR GRAY IRON REPORTED IN TERMS OF THE SMITH-WATSON-TOPPER PARAMETER

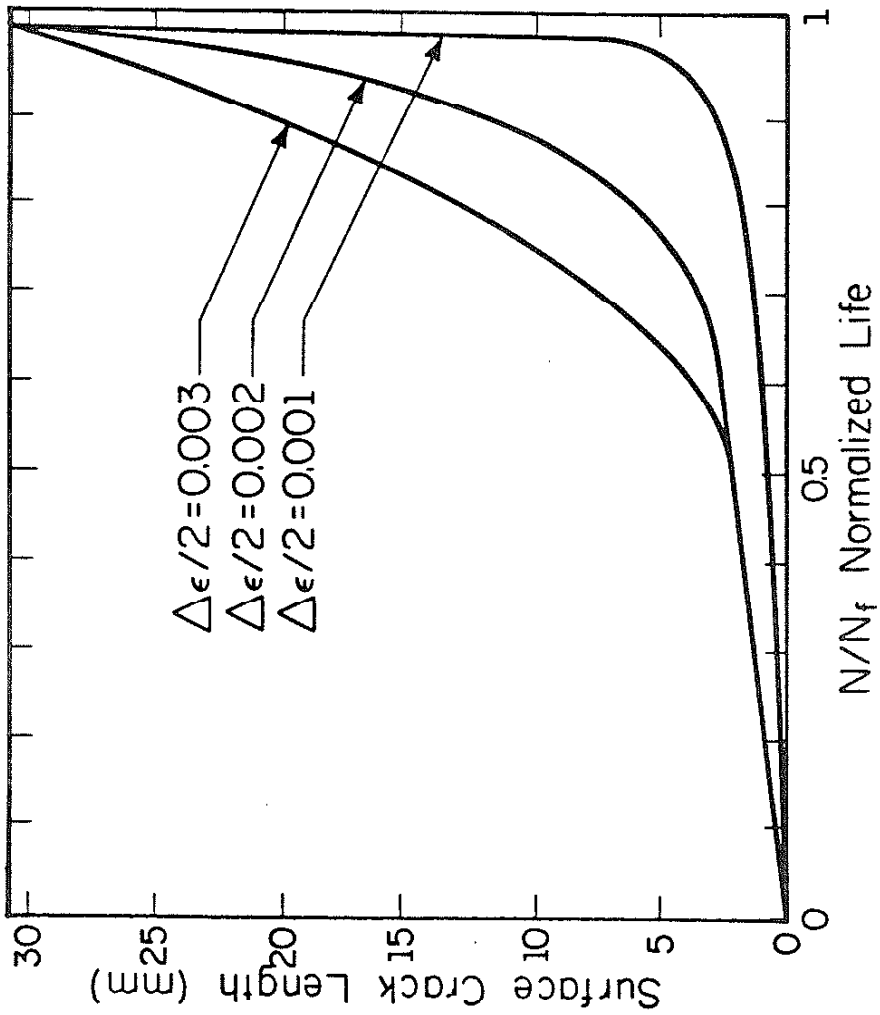

FIG. 21 SURFACE CRACK LENGTH VERSUS APPLIED CYCLE RATIO FOR GRAY IRON

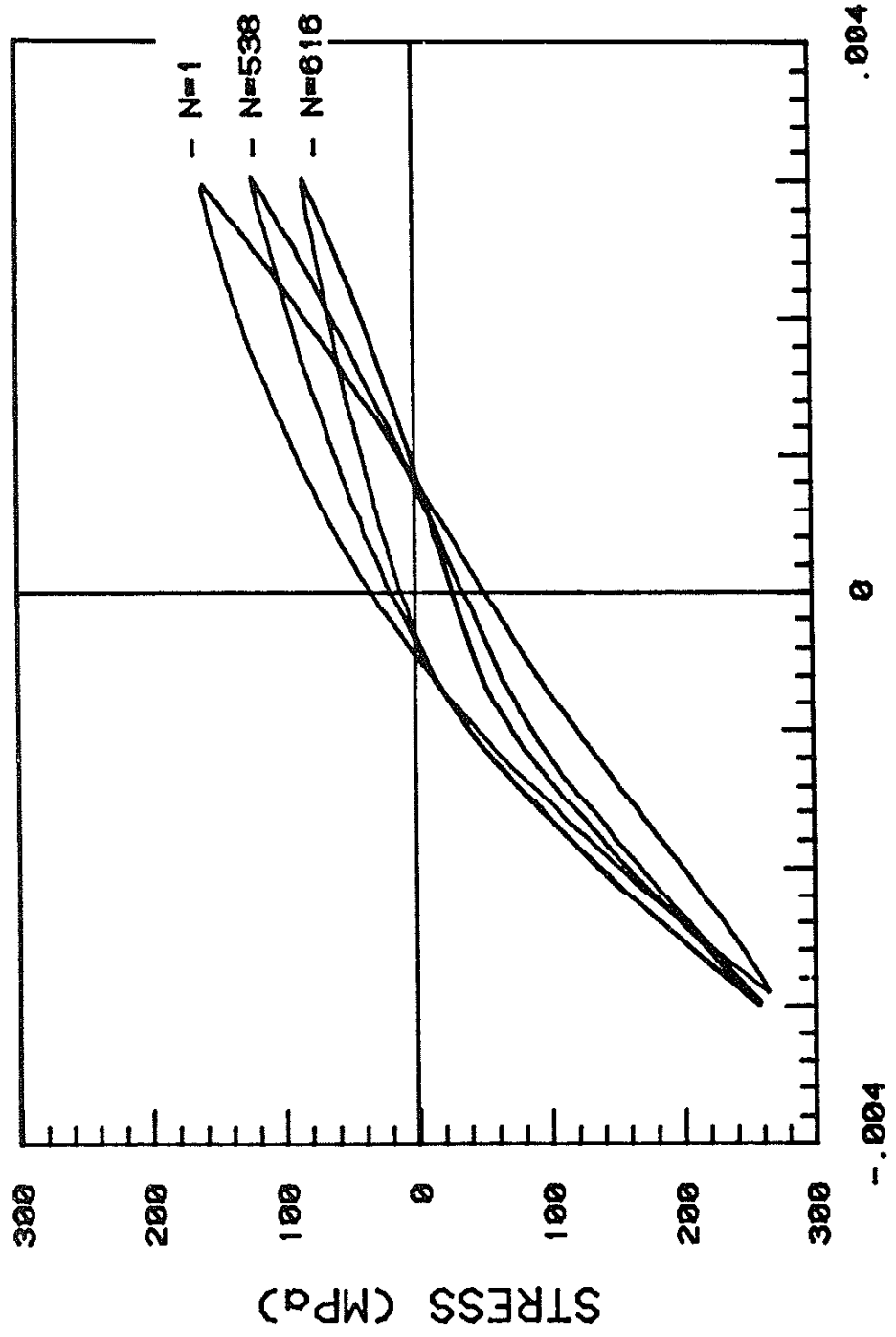

FIG. 22 HYSTERESIS RESPONSE OF GRAY IRON SHOWING DECREASE IN PEAK TENSILE STRESS WITH INCREASING APPLIED CYCLES

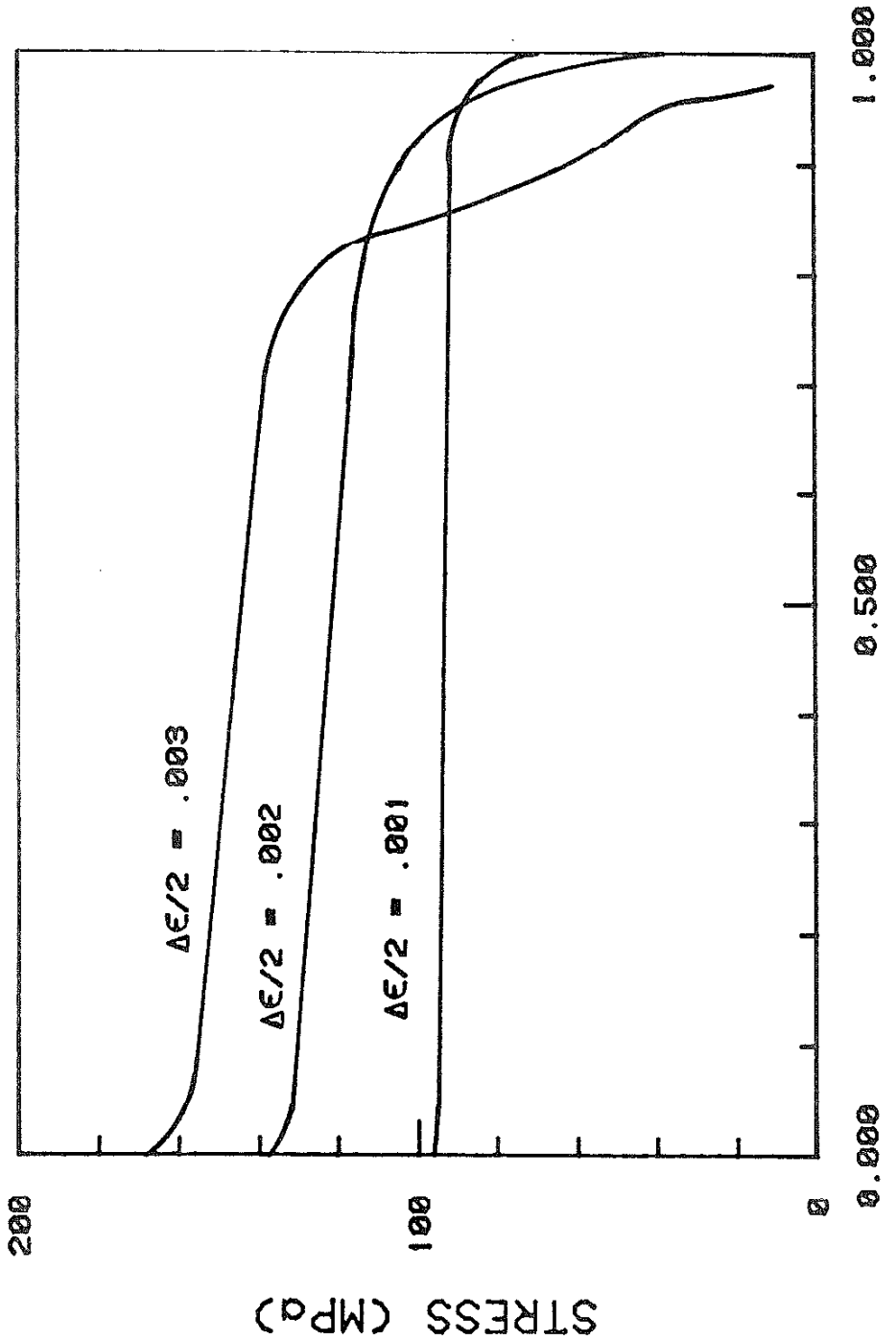

FIG. 23 PEAK TENSILE STRESS VERSUS APPLIED CYCLE RATIO FOR GRAY IRON

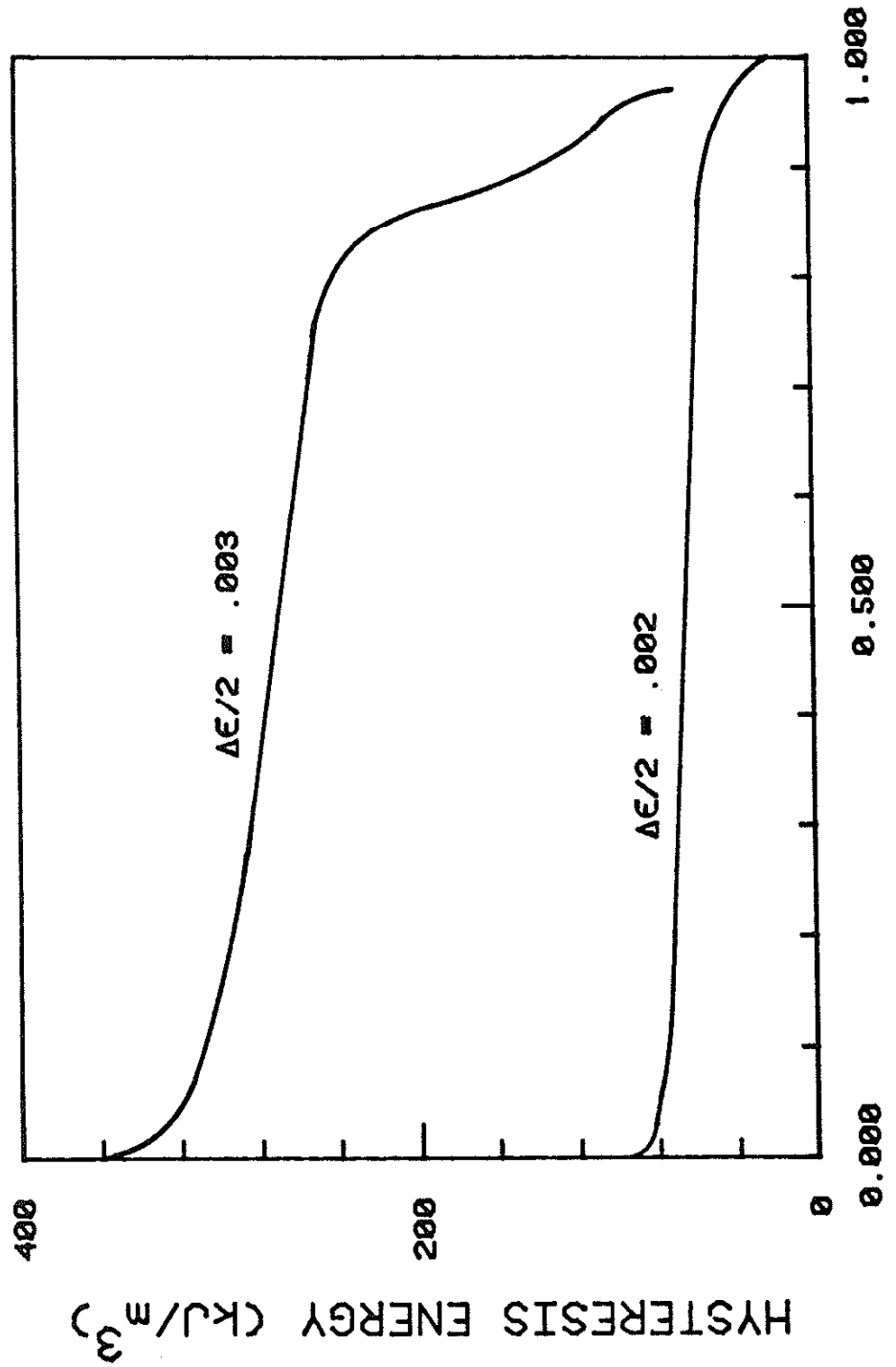

FIG. 24 HYSTERESIS ENERGY VERSUS APPLIED CYCLE RATIO FOR GRAY IRON

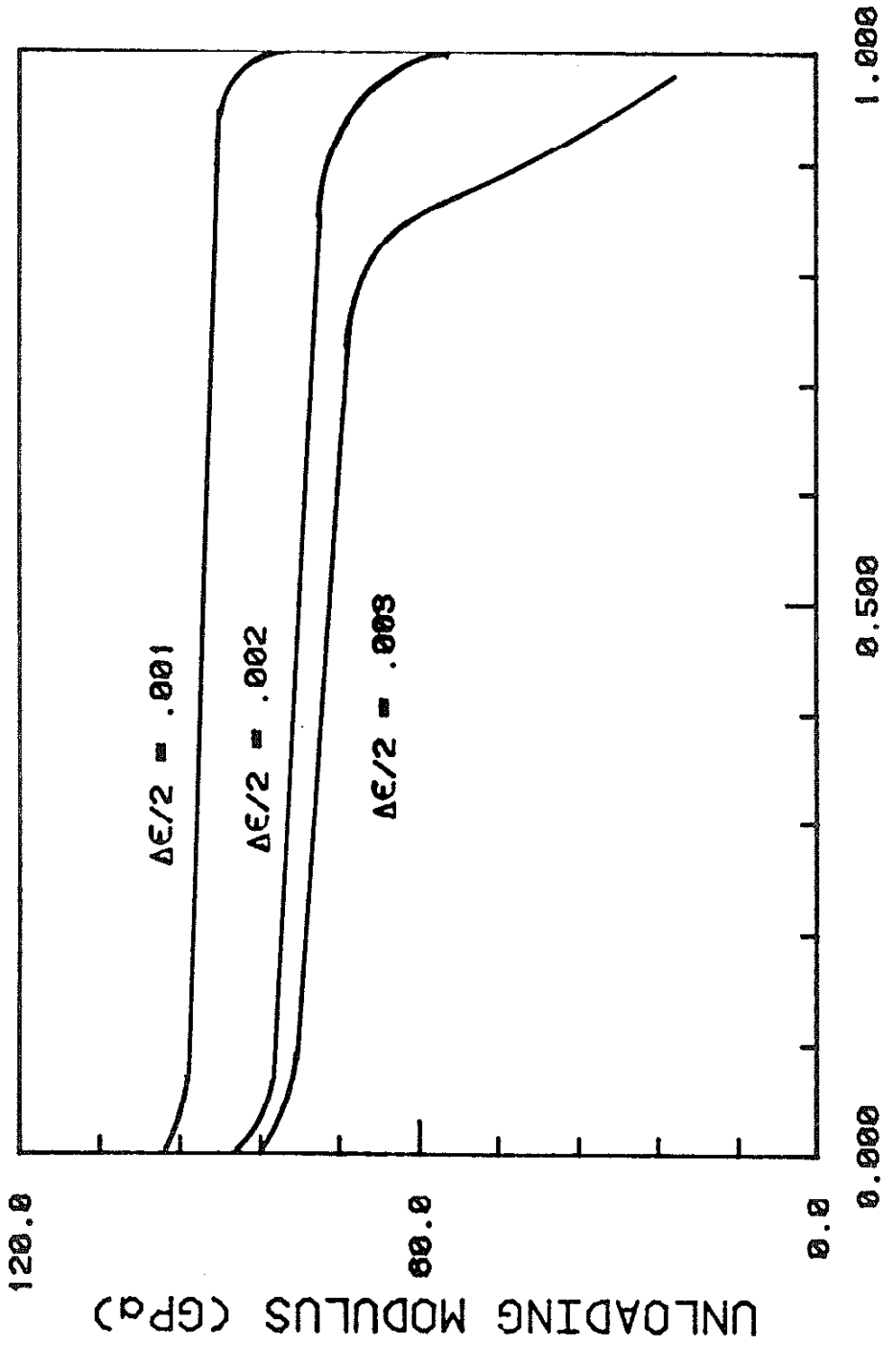

FIG. 25 UNLOADING MODULUS VERSUS APPLIED CYCLE RATIO FOR GRAY IRON

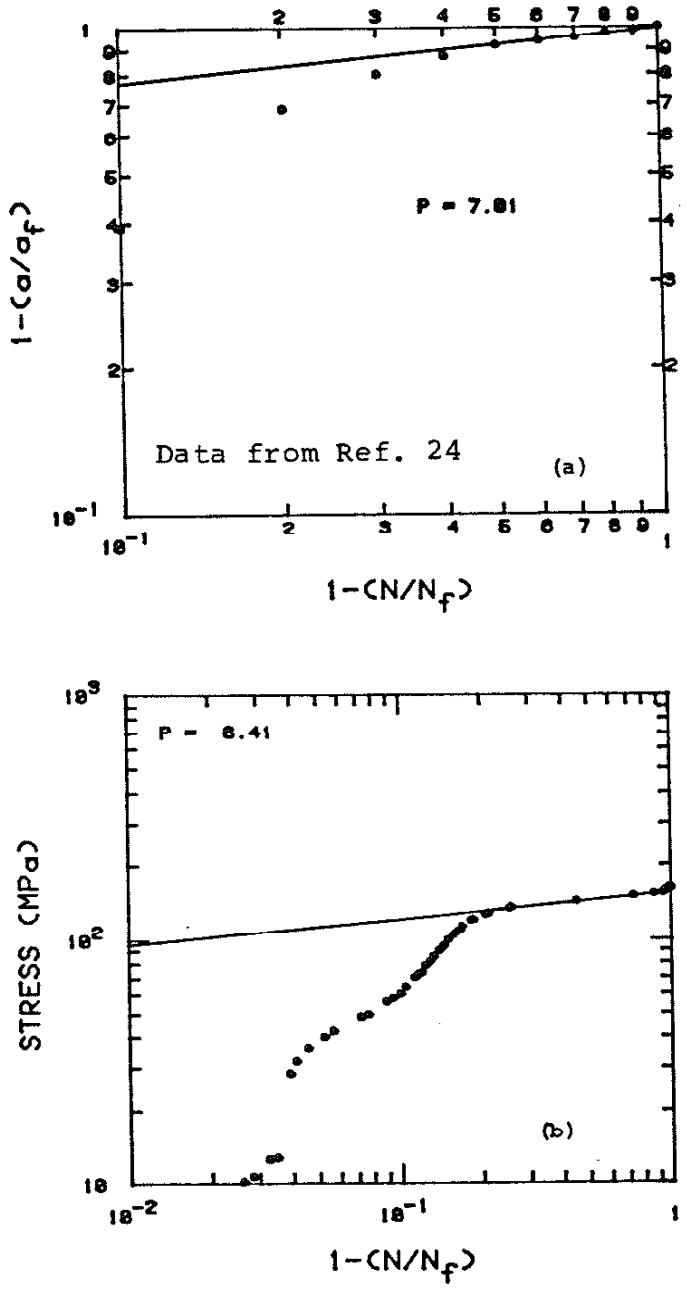

FIG. 26 DETERMINATION OF THE DAMAGE RATE PARAMETER FROM (a) CRACK GROWTH, (b) STRESS DROP, (c) HYSTERESIS ENERGY DROP AND (d) UNLOADING MODULUS DROP

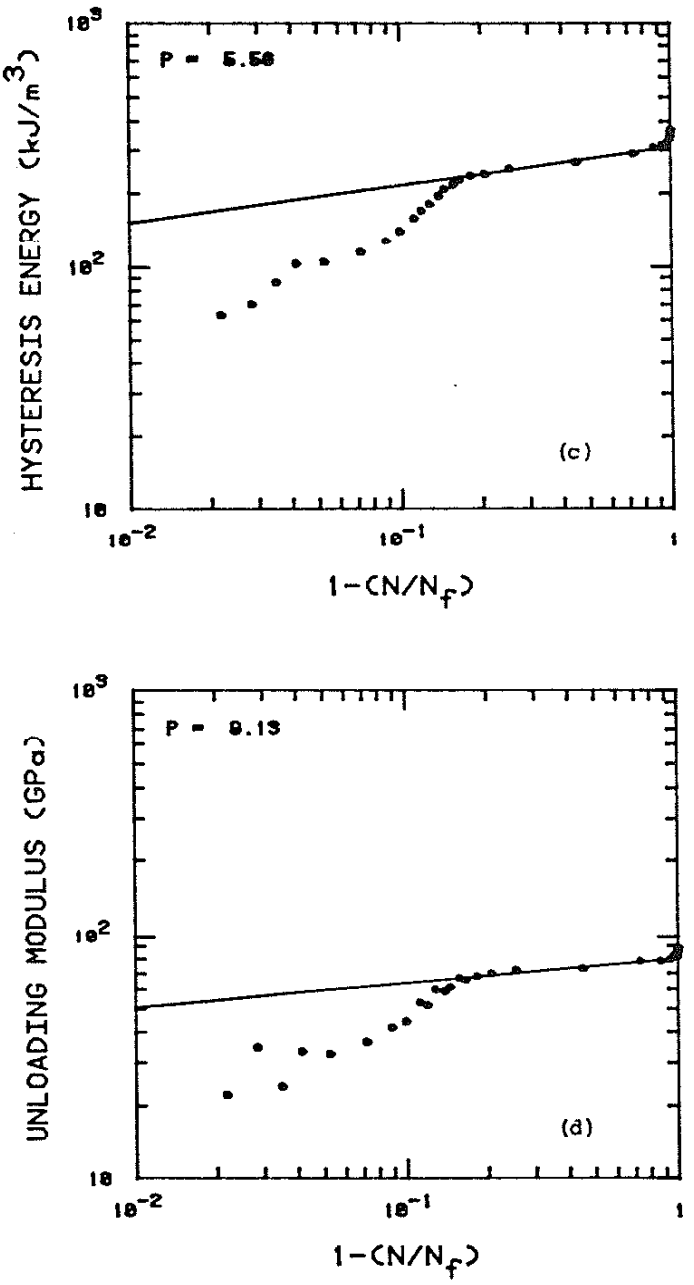

FIG. 26 DETERMINATION OF THE DAMAGE RATE PARAMETER FROM (a) CRACK GROWTH, (b) STRESS DROP, (c) HYSTERESIS ENERGY DROP AND (d) UNLOADING MODULUS DROP

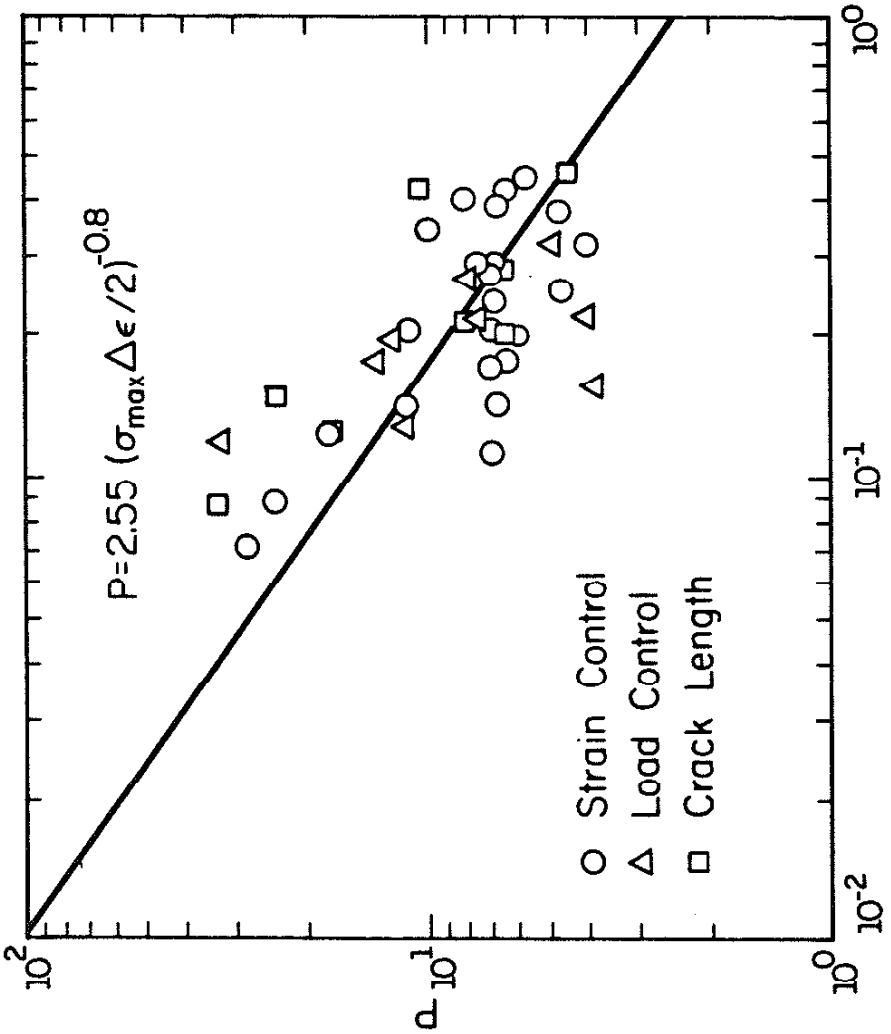

FIG. 27 DAMAGE RATE PARAMETER P PLOTTED IN TERMS OF THE SMITH-WATSON-TOPPER PARAMETER

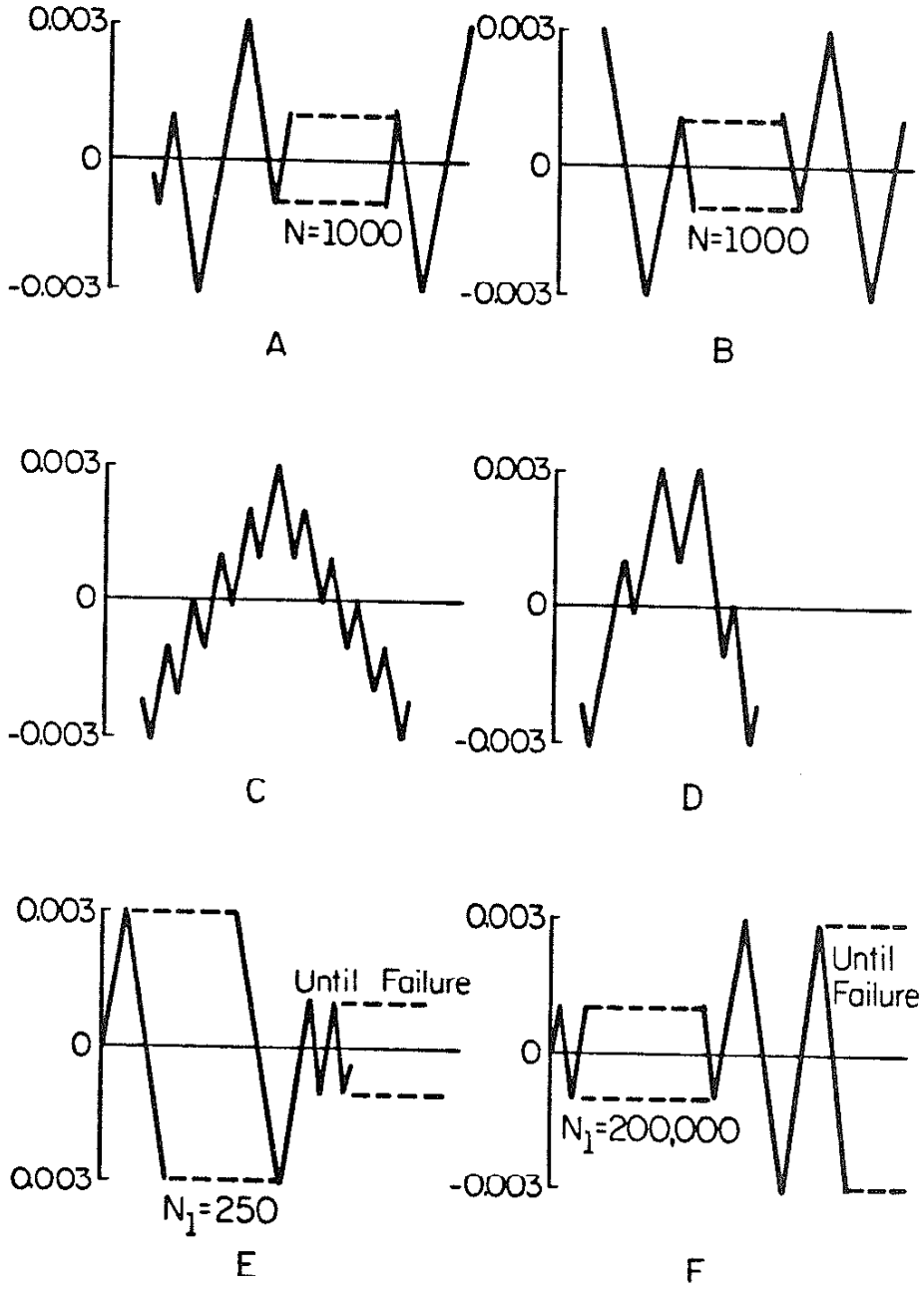

FIG. 28 LOAD HISTORIES FOR VARIABLE AMPLITUDE FATIGUE TESTS

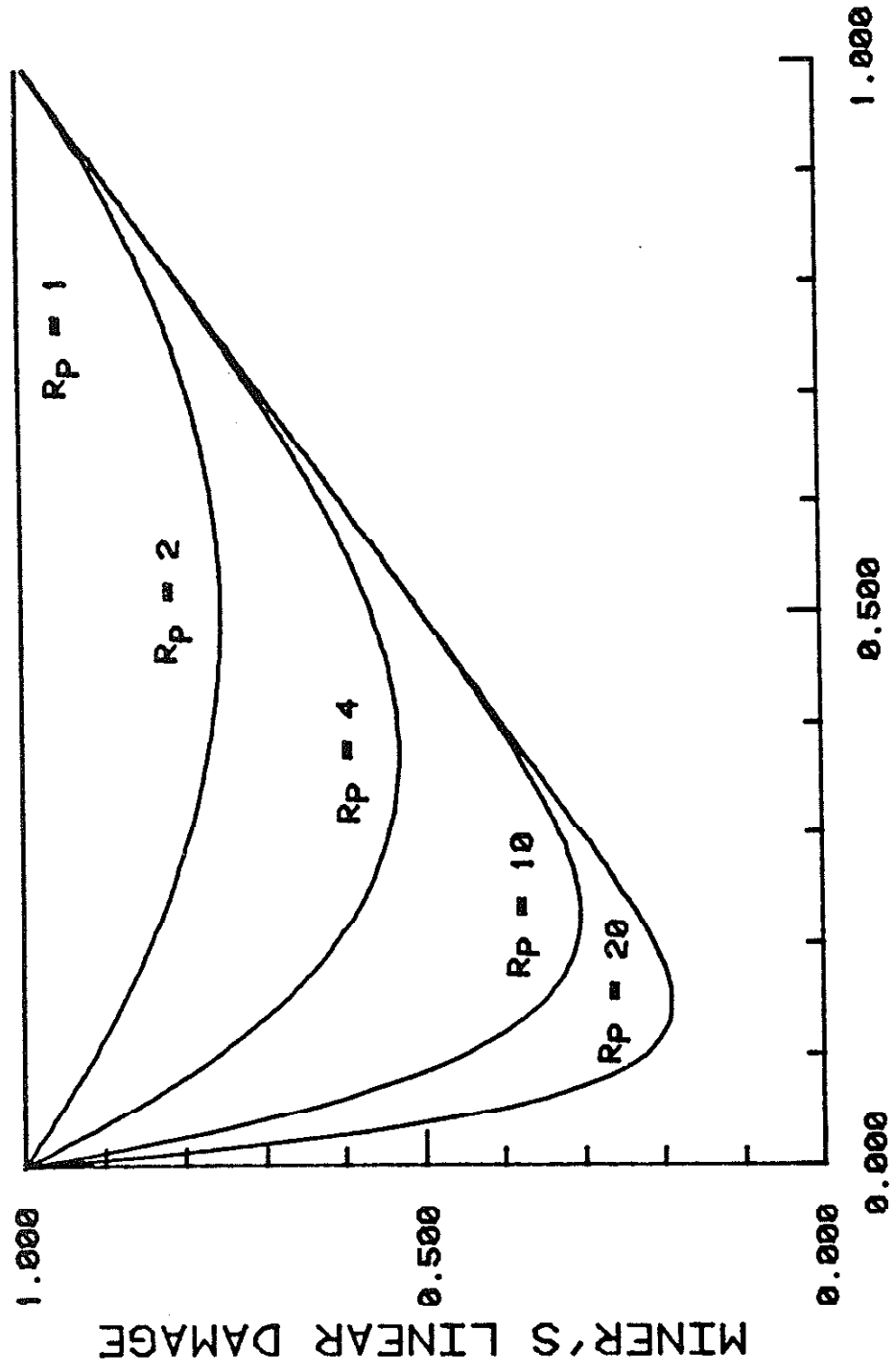

FIG. 29 MINER'S LINEAR DAMAGE PREDICTION AT FAILURE FOR HI-LO LOADING. FAILURE WAS DETERMINED BY CONTINUUM DAMAGE MODEL FOR SEVERAL VALUES OF $R_p = (P_2 + 1)/(P_1 + 1)$.

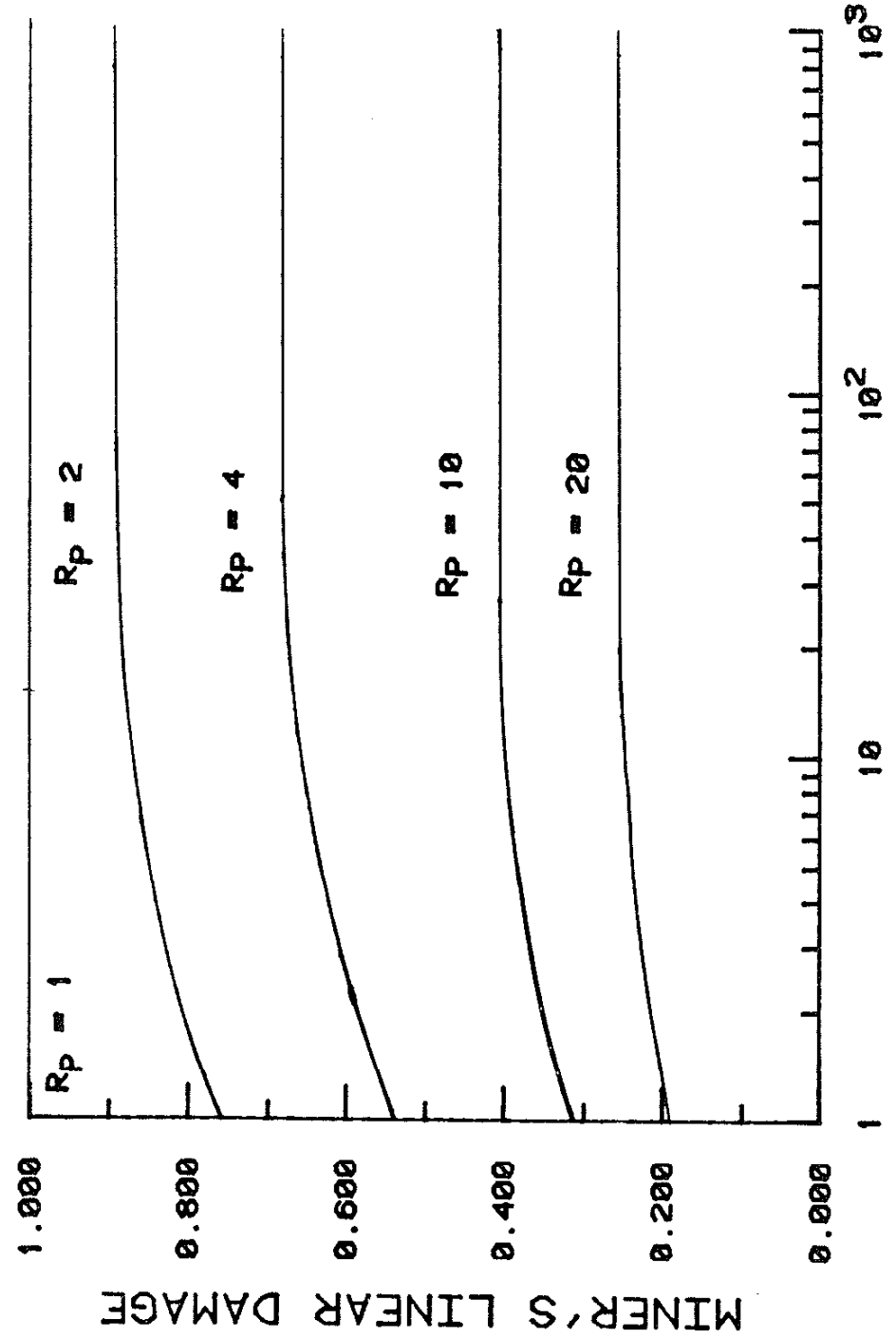

FIG. 30 MINER'S LINEAR DAMAGE VERSUS BLOCKS TO FAILURE FOR TWO LEVEL REPEATED BLOCK LOADING. FAILURE WAS DETERMINED BY CONTINUUM DAMAGE MODEL FOR SEVERAL VALUES OF $R_p = (P_2 + 1)/(P_1 + 1)$.

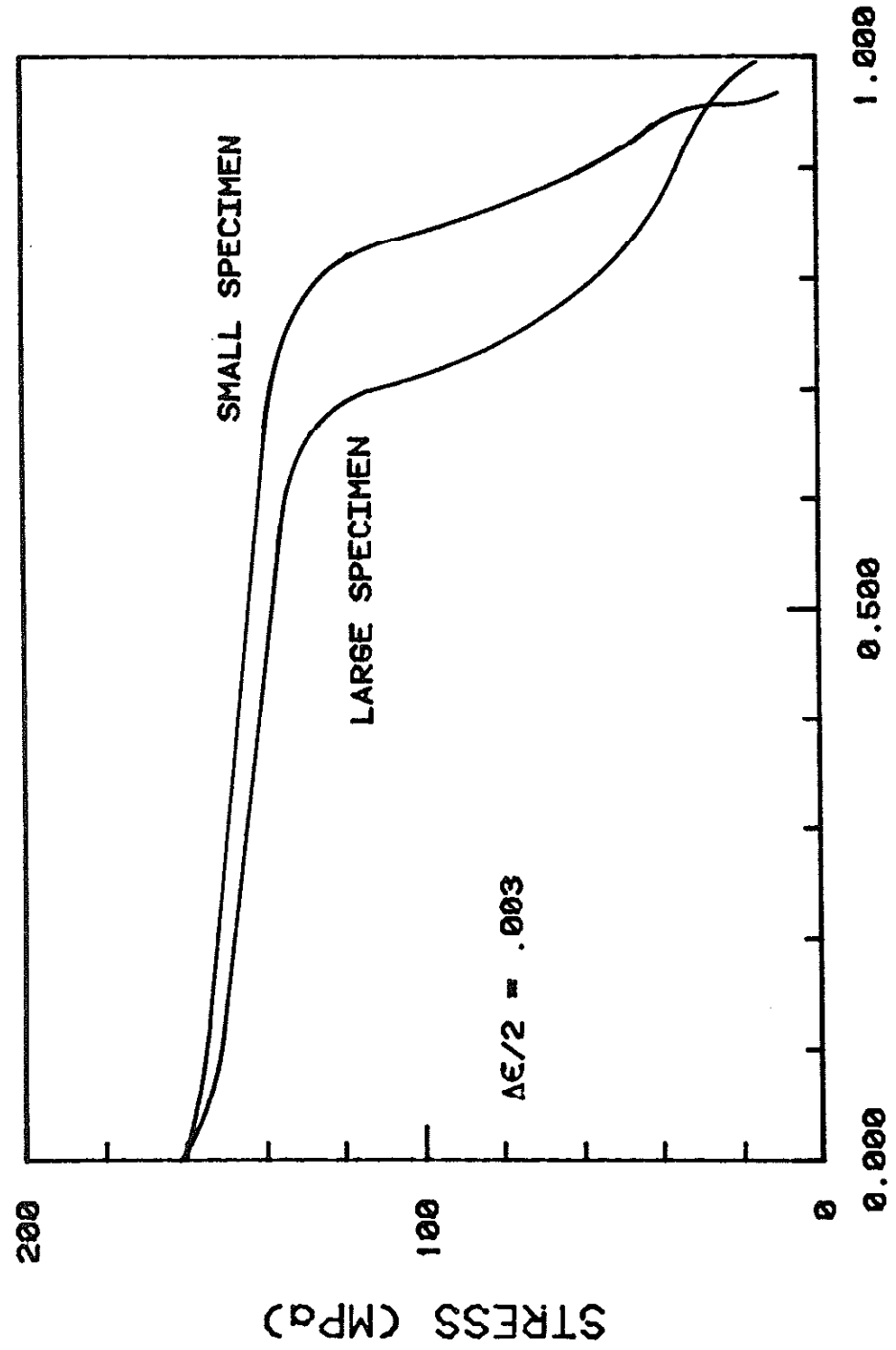

FIG. 31 PEAK TENSILE STRESS VERSUS APPLIED CYCLE RATIO FOR TWO DIFFERENT SIZED GRAY IRON SPECIMENS

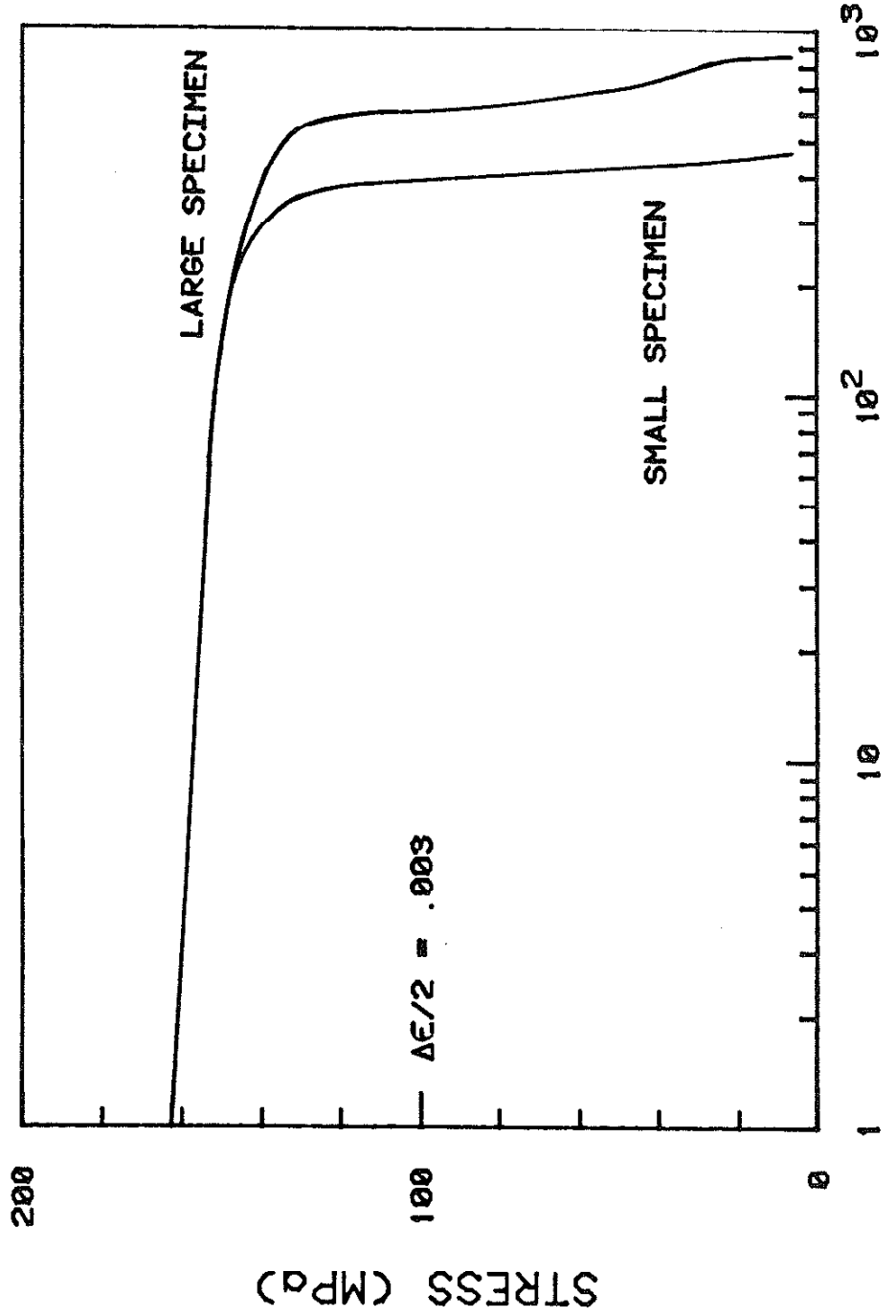

FIG. 32 PEAK TENSILE STRESS VERSUS APPLIED CYCLES FOR TWO DIFFERENT SIZED GRAY IRON SPECIMENS

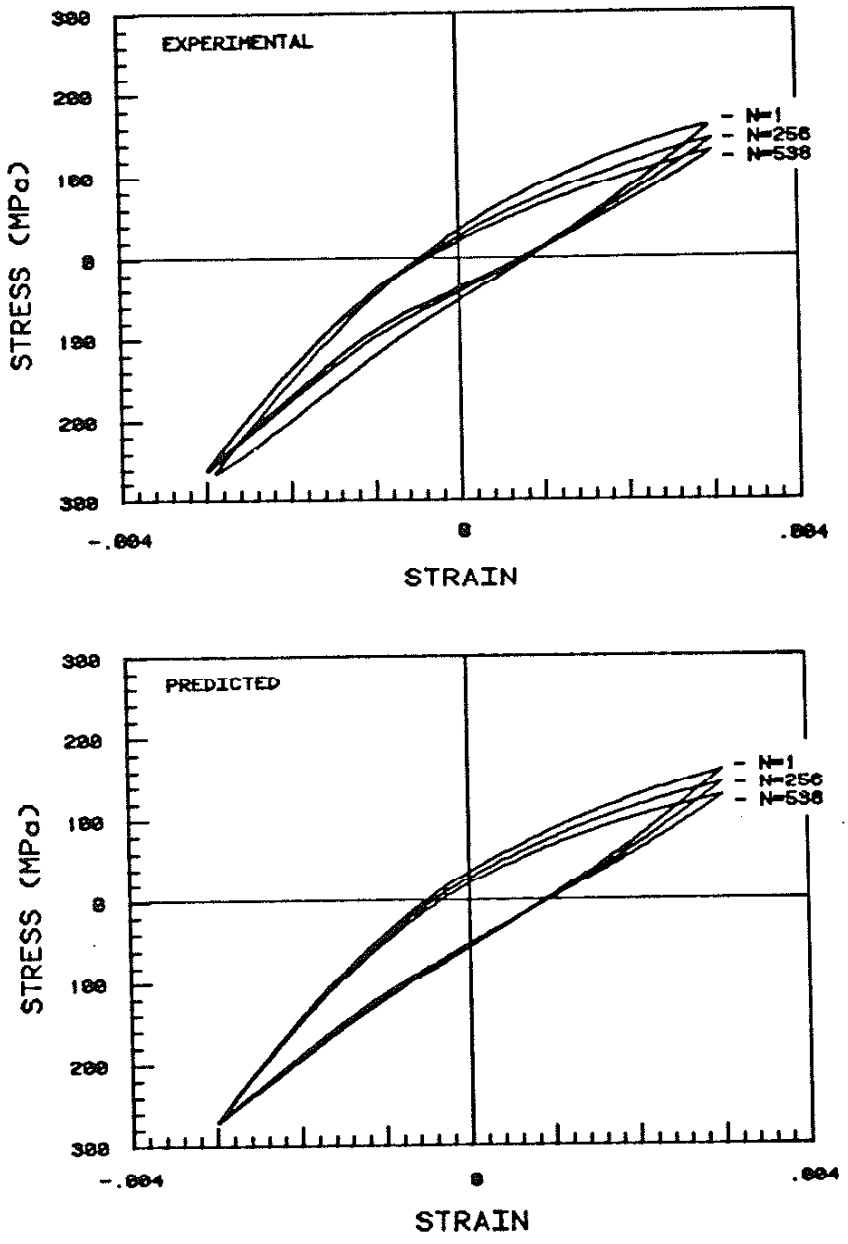

FIG. 33 EXPERIMENTAL AND PREDICTED CYCLIC STRESS/STRAIN RESPONSE OF GRAY IRON AT SELECTED CYCLE NUMBERS; $\varepsilon_{max} = .003$, $\varepsilon_{min} = -.003$

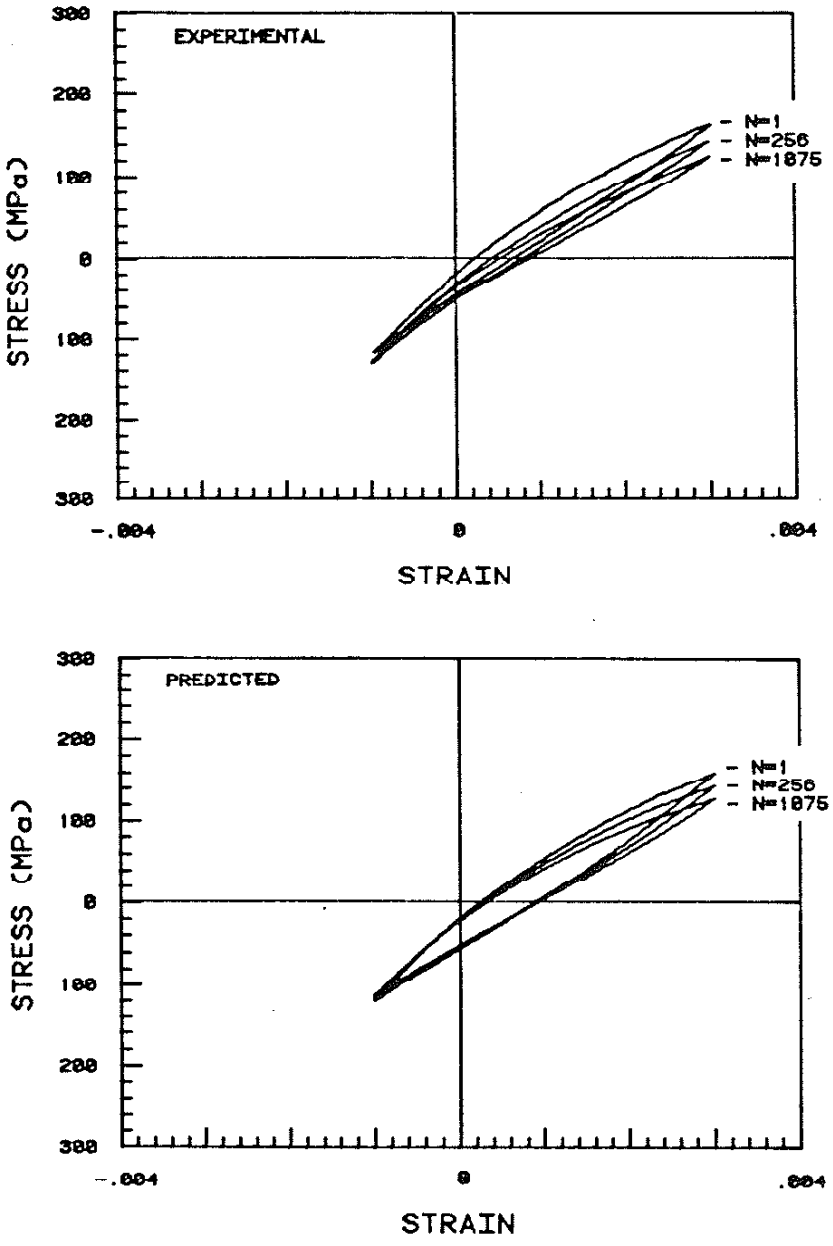

FIG. 34 EXPERIMENTAL AND PREDICTED CYCLIC STRESS/STRAIN RESPONSE OF GRAY IRON AT SELECTED CYCLE NUMBERS; $\varepsilon_{max} = .003$, $\varepsilon_{min} = -.001$

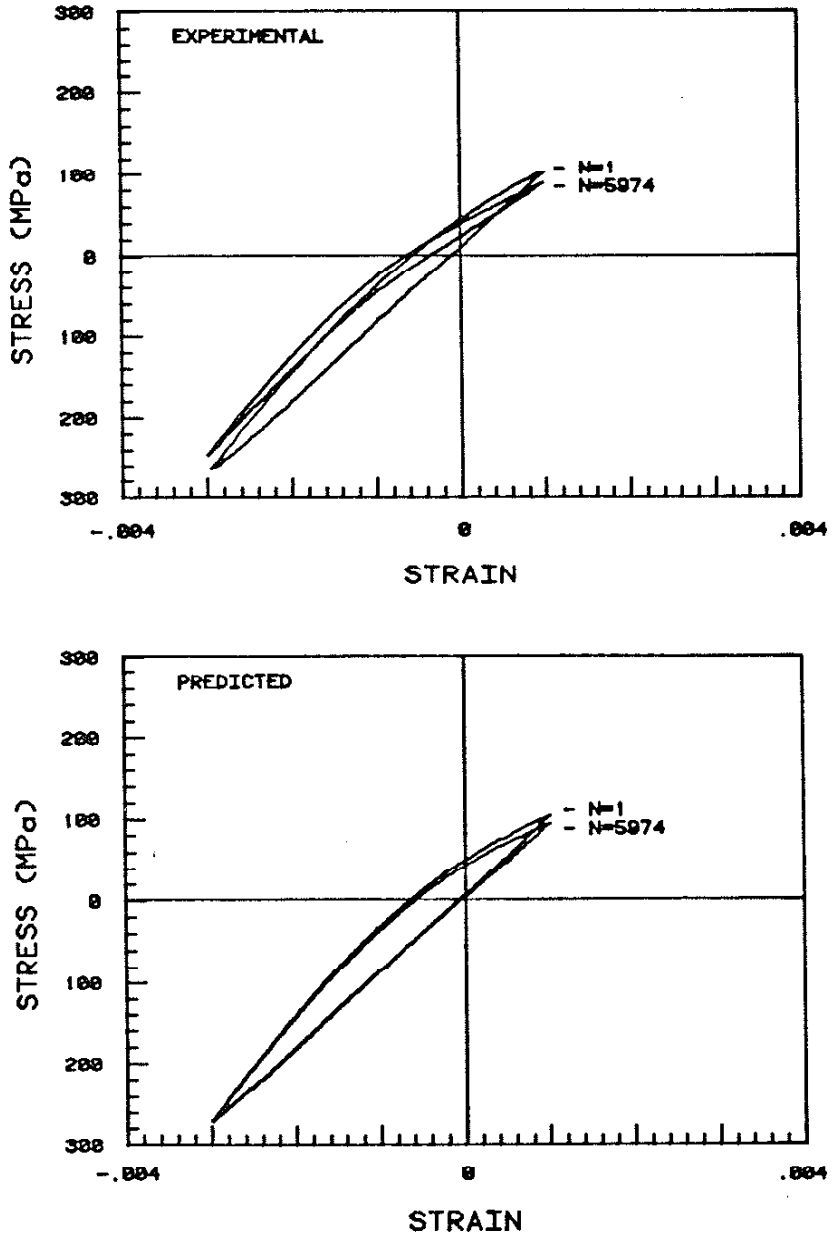

FIG. 35 EXPERIMENTAL AND PREDICTED CYCLIC STRESS/STRAIN RESPONSE OF GRAY IRON AT SELECTED CYCLE NUMBERS; $\varepsilon_{max} = .001$, $\varepsilon_{min} = -.003$

APPENDIX A

MATERIAL DESCRIPTION

A. Gray Iron

Test bars, 30 mm in diameter and 200 mm long, were cast in chemically bonded sand molds to produce pearlitic gray iron. Graphite structure is classified as approximately 80 percent ASTM Type A (Size 3 - 4), and approximately 20 percent ASTM Type D (Size 7). Approximately 20 percent of the Type A has a tendency toward Type B. Matrix microstructure is classified as 5 - 7 percent ferrite with the balance moderately coarse pearlite. Approximately 98 percent of the pearlite is resolvable at 200X magnification. Material chemistry is given in Table A1 and photomicrographs shown in Fig. A1.

B. Compacted Graphite Iron

Test bars, 30 mm in diameter and 200 mm long, were cast in green sand molds. Graphite structure is 5 - 7 percent nodules (ASTM Type I, Size 6 - 7) with the balance compacted flake (Size 4 - 5 per gray iron plate). Matrix microstructure is 10 - 12 percent ferrite with the balance pearlite. A small amount of microshrinkage is detectable. Material chemistry is also given in Table A2 and the microstructure shown in Fig. A2.

C. Nodular Iron

Standard Y blocks were cast in chemically bonded sand molds to produce nodular iron. Graphite structure is 95 percent nodules (ASTM Type I) and 5 percent irregular nodules (ASTM Type II). Nodules are 10 percent Size 5 and 90 percent Size 6.

The matrix consisted of 45 - 50 percent ferrite with the balance pearlite. A small amount of microshrinkage is detectable. Chemistry is given in Table A1 and photomicrographs in Fig. A3.

TABLE A1. MATERIAL CHEMISTRY (WT %)

	C	Si	Mn	S	P	Ti	Ni	Cr	Mo	Cu	Sn	Al	Mg	Ce
Gray Iron	3.30	2.20	.44	.02	.01	.01	.06	.03	.01	.40	-	-	-	-
CG Iron	3.72	2.55	.63	.018	.04	.18	.31	.11	.02	.42	.12	.01	.019	-
Nodular Iron	3.85	2.71	.49	.008	-	-	-	.065	-	.23	-	-	.05	.015

ETCHED IN PICRAL

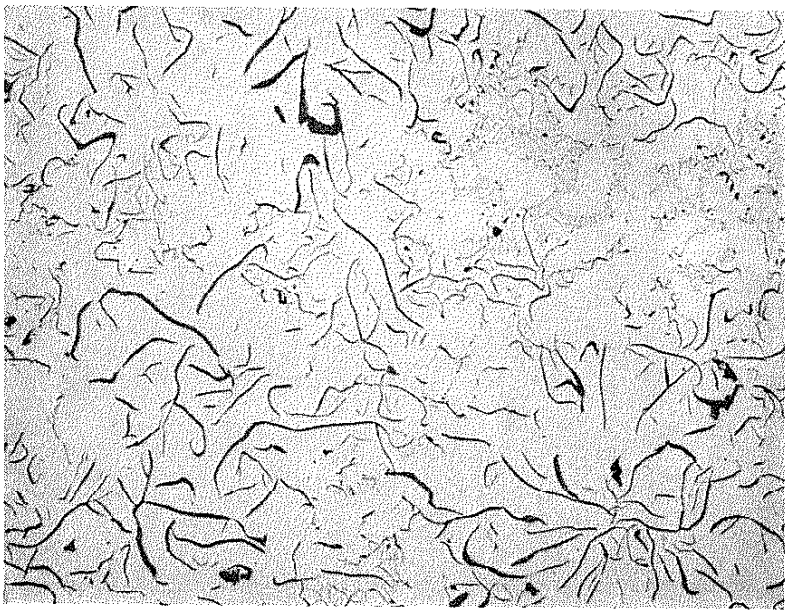

UNETCHED

100X

FIG. A1 GRAY IRON MICROSTRUCTURE

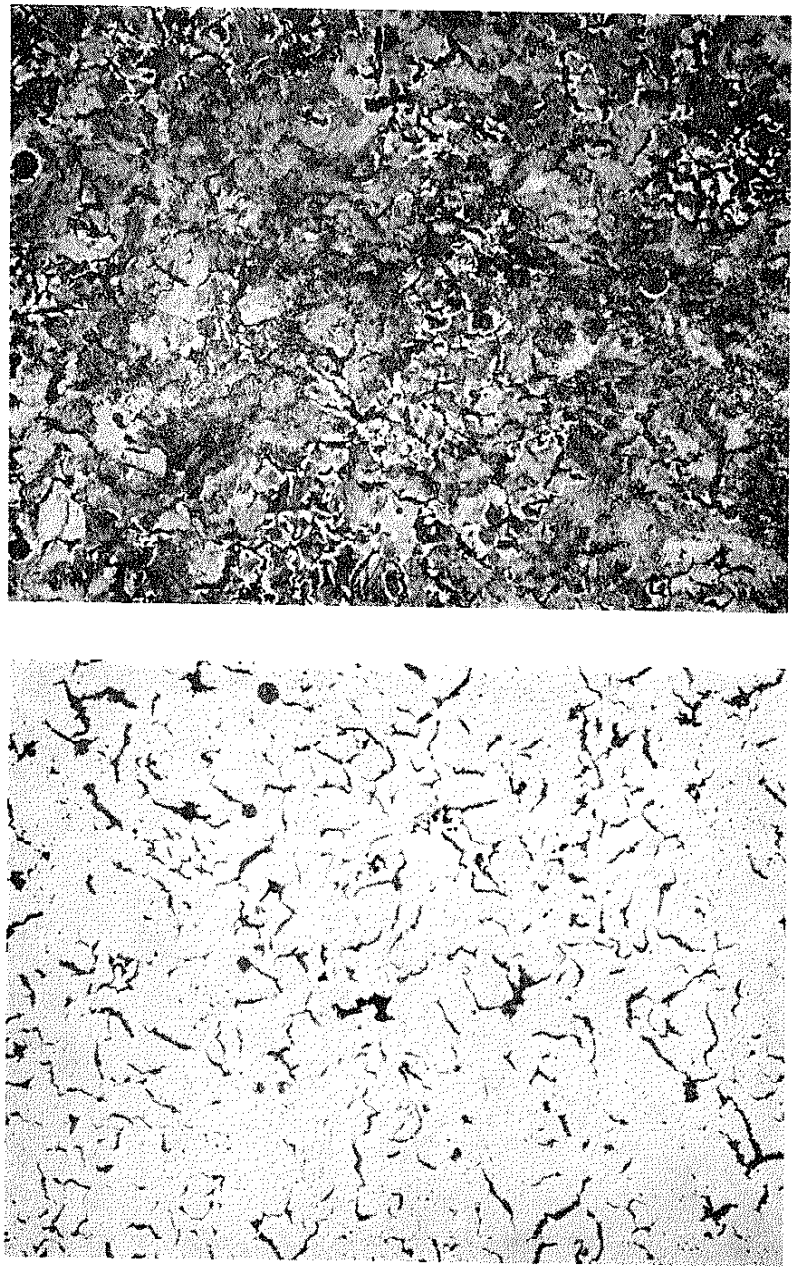

FIG. A2 CG IRON MICROSTRUCTURE

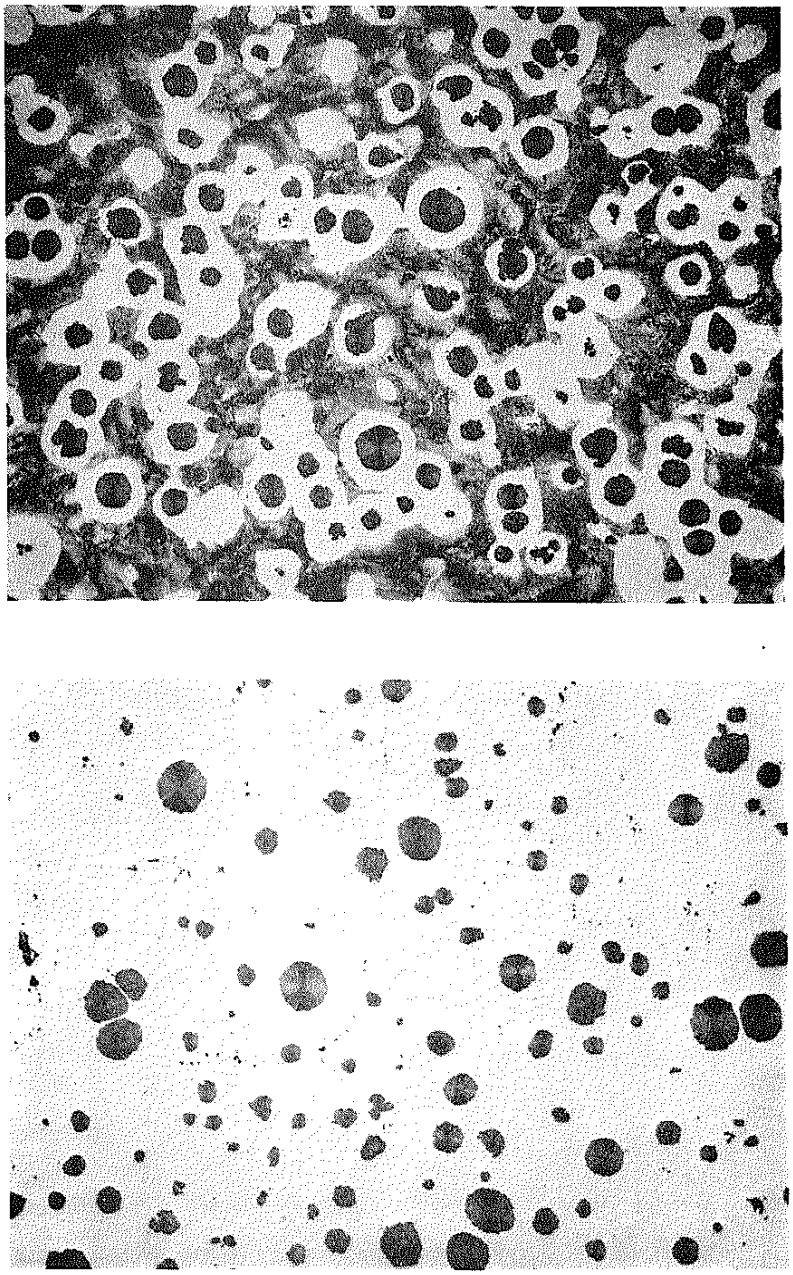

FIG. A3 NODULAR IRON MICROSTRUCTURE

APPENDIX B

STRESS/STRAIN ALGORITHM FOR CAST IRON SUBJECTED VARIABLE STRAIN HISTORIES

The following algorithm (suitable for computer implementation) combines the cast iron stress/strain model with the essential features of rainflow counting [37] so that variable strain histories may be analyzed. It is assumed that the strain history to be evaluated is known beforehand and that it can be rearranged to begin and end with the maximum or minimum strain (whichever has the greatest absolute magnitude). The following steps allow the initialization of stress and strain arrays needed for the simulation.

Step 1: Determine the maximum strain, e_{max}, and minimum strain, e_{min}.

Step 2: Form a strain array, e_i, containing 101 discrete strains in even increments such that $e_1 = e_{min}$ and $e_{101} = e_{max}$.

Step 3: Form a strain range array, Δe_i, containing 101 discrete strain ranges in even increments such that $\Delta e_1 = 0$ and $\Delta e_{101} = e_{max} - e_{min}$.

Step 4: Form a monotonic stress array, $(S_M)_i$, containing 101 discrete stress values corresponding to strain, e_i, or

$$\left| e_i \right| = \frac{(S_M)_i}{E_0 + m(S_M)_i} + \left[\frac{(S_M)_i}{K}\right]^{1/n_T} \qquad \text{(B1)}$$

The Newton-Raphson iterative technique can be used to solve this equation. If e_i is positive, use tensile properties and make $(S_M)_i$ positive; if e_i is negative, use compressive properties and make $(S_M)_i$ negative.

Step 5: Form a bulk stress array, $(S_B)_i$, containing 101 discrete stress values corresponding to strains, e_i. Equation (8) may be used, but a more direct method (without regression for bulk properties) is chosen. Here, an intermediate result, X, in the following relationship, allows for straightforward solution.

$$e_i = \frac{X}{E_0 + m_T X} + \left[\frac{X}{K_T}\right]^{1/n_T} \qquad \text{(B2)}$$

$$(S_B)_i = \frac{E_0 X}{E_0 + m_u X}$$

$(S_B)_i$ should be given the sign of e_i.

Step 6: Form a bulk stress range array, $(\Delta S_B)_i$, containing 101 discrete stress range values corresponding to Δe_i, or

$$\Delta e_i = \frac{X}{E_0 + (m_T/2)X} + 2\left[\frac{X}{2K_T}\right]^{1/n_T} \qquad (B3)$$

$$(\Delta S_B)_i = \frac{E_0 X}{E_0 + m_u X}$$

Step 7: Form a graphite stress array, $(S_G)_i$, according to the following

$$(S_G)_i = (S_M)_i - (S_G)_i \quad \text{if } e_i < 0$$
$$= 0 \quad \text{if } e_i \geq 0 \qquad (B4)$$

Step 8: Form a crack closure stress array, $(S_{cc})_i$, by the following relationship:

$$(S_{cc})_i = Q\,(e_{max} - e_i)^q \qquad (B5)$$

The values of Q and q are solved according to Eqs. (22)-(24).

Step 9: Solve

$$A_{eff} = 1 + \frac{m_u (S_M)_{101}}{E_0} \qquad (B6)$$

Several other arrays are needed by the algorithm, but need not be initialized. They are

$(\sigma_B)_n$ = rainflow bulk stress array

σ_n = rainflow total stress array (B7)

ε_n = rainflow strain array

m_n = rainflow index array

Stress/strain simulation of cast iron now progresses according to the flow chart in Fig. B1. The algorithm determines when closed hysteresis loops are formed and calculates strain range, stress range and mean stress for each. All of the calculation of fatigue life and deformation behavior in this thesis were performed with this algorithm.

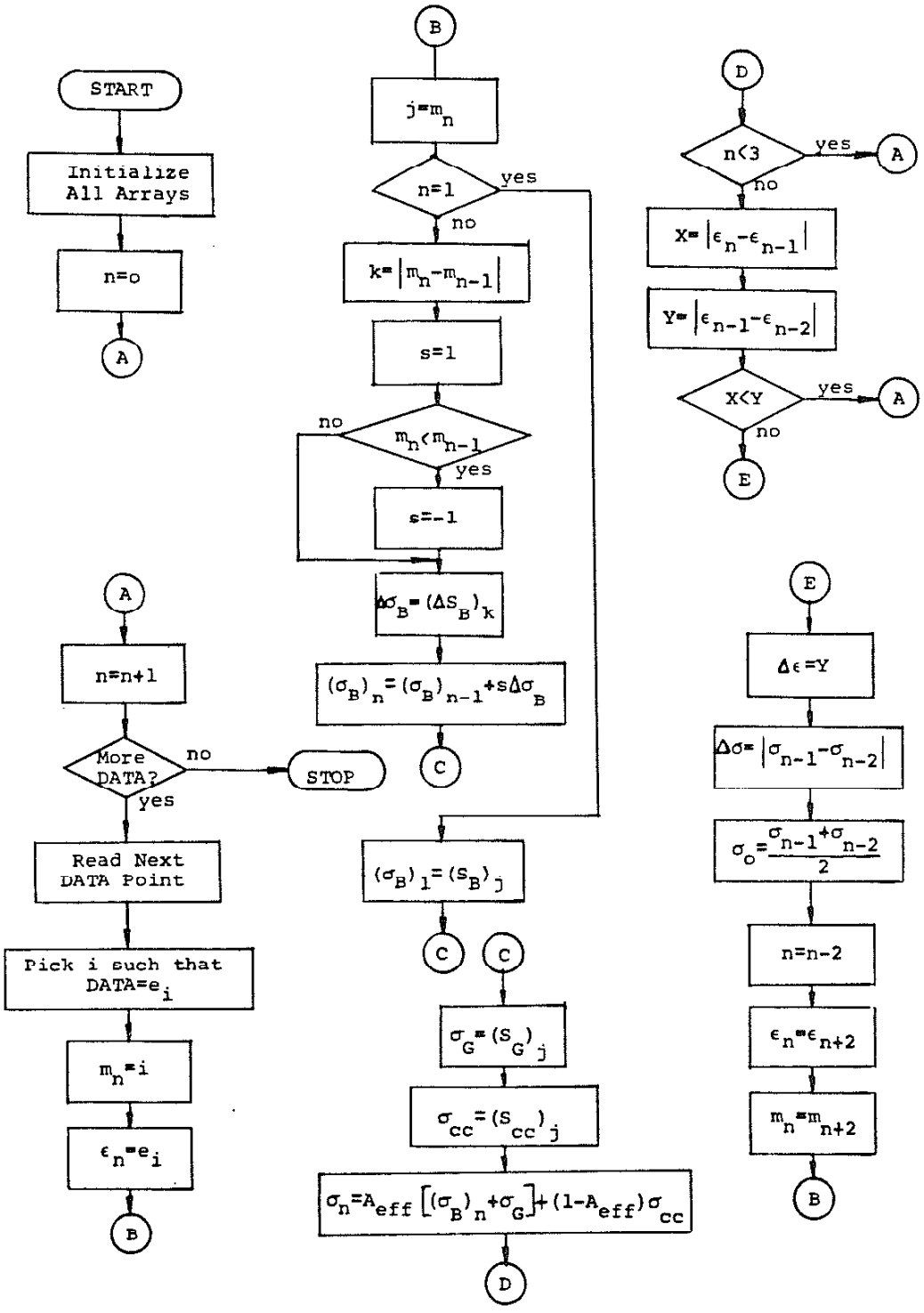

FIG. B1 FLOW CHART OF STRESS/STRAIN ALGORITHM

APPENDIX C

A PROPOSED METHOD FOR DETERMINING CYCLIC STRESS/STRAIN PROPERTIES FROM STRAIN-CONTROLLED FATIGUE TESTS

Procedures for determining stable cyclic stress/strain material properties of wrought metals are well defined [38]. It is less clear how to do this for cast irons since, in general, no stable behavior exists. It would be, however, desirable to at least minimize the effect of early matrix transient behavior. Stress/strain properties obtained from monotonic tests would then be better replaced by information from strain-controlled fatigue tests. A proposed procedure for doing this follows.

1. Conduct a series of completely-reversed strain-controlled fatigue tests at different strain amplitudes. Stress/strain hysteresis loops are stored at prescribed times during each test. In this investigation, loops were sampled at cycles numbers corresponding to integer powers of 2 and when peak tensile loads decreased by prescribed amounts (5 to 95 percent of maximum initial load in 5 percent increments). Also, one hundred (100) stress/strain pairs per loop were used.

2. For each test (strain amplitude), perform the following analysis.

   2a. From each loop, determine the peak tensile and compressive stresses and the unloading tangent modulus from the peak tensile stress.

   2b. Plot peak tensile stress versus $1 - (N/N_f)$ on a log-log plot as shown in Fig. 26(b). Determine the slope and intercept of the straight-line portion of the curve. The intercept corresponds to σ_{max} in Eq. (35) and represents the extrapolated peak tensile stress from which the effects of early matrix hardening/softening have been minized.

   2c. Repeat the procedure in 2b with peak compressive stresses to determine the extrapolated initial peak compressive stress.

   2d. Repeat the procedure in 2b with unloading modulus to determine the extrapolated initial unloading modulus. This is illustrated in Fig. 26(d).

3. Cyclic stress/strain properties (m_T, K_T, n_T, m_C, K_C, n_C, m_u and E_0) can now be determined as follows:

   3a. For each strain amplitude, plot unloading modulus versus peak tensile stress as shown in Fig. 9. Linear regression will result

in a slope, m_u, and intercept, E_0. As discussed earlier, the intercept should closely correspond to the tangent modulus of the extrapolated initial tensile and compressive stress/strain curves at zero stress and strain.

3b. Initial peak tensile stresses are divided by their corresponding strain amplitudes to give secant moduli as a function stress. When plotted as in Fig. 2, there should be a well-defined linear region. A best fit straight line through this region and the intercept, E_0 (previously determined in Step 3a), will have a slope, m_T. Secant strain expressed by Eq. (3) is calculated and remaining plastic strain (strain amplitude minus secant strain) determined as a function of tensile stress. Material properties, K_T and n_T, are determined as illustrated in Fig. 3 and Eq. (4).

3c. Compressive material properties (m_C, K_C and n_C) are determined in the same way as tensile properties.

Stress/strain material properties derived in this manner have two distinct advantages over those derived from monotonic tests. First, since the results are obtained from a number of samples, they should more representative of average behavior. Second, the effects of early matrix transient behavior will be minimized in an analogous manner to stable cyclic properties in wrought metals.

REFERENCES

1. Simpson, B.L., "History of the Metalcasting Industry," American Foundrymen's Society Publication, 1948, pp. 189-190.

2. Thum, A. and Ude, H., "Die-Elastizitat und die Schwingungsfestigkiet des Guesseisens," Die Giesserei, Vol. 16, 1929, pp. 547-556.

3. Coffin, L.F., Jr., "The Flow and Fracture of a Brittle Material," Journal of Applied Mechanics, American Society of Mechanical Engineers, Vol. 17, No. 3, September 1950, p. 74.

4. Flinn, R.A. and Ely, R.J., "Stress Determination in Cast Iron for Railway Service," Symposium on Testing of Cast Iron with SR-4 Type of Gage, ASTM STP 97, 1950.

5. MacKenzie, discussion of reference 4.

6. Clough, W.R. and Shank, M.E., "The Deformation and Rupture of Gray Cast Iron," Transactions of the American Society for Metals, Vol. 49, 1957, pp. 241-262.

7. Gilbert, G.N.J., "Variations of the Microstructure of a Flake Graphite Cast Iron after Stressing in Tension and Compression," Journal of the British Cast Iron Research Association, Vol. 12, 1964, pp. 31-47.

8. Gilbert, G.N.J., "Stress/Strain Properties of Cast Iron and Poisson's Ratio in Tension and Compression," Journal of the British Cast Iron Research Association, Vol. 9, 1961, pp. 347-363.

9. Gilbert, G.N.J., "The Components of Strain Due to Deformation of the Matrix and Due to Volume Changes in a Flake Graphite Cast Iron Under Uniaxial Stress," Journal of the British Cast Iron Research Association, Vol. 11, 1963, pp. 512-524.

10. Mitchell, M.R., "Cyclic Deformation and Fracture Behavior of Gray Cast Iron," M.S. Thesis, Wayne State University, Department of Metallurgy, Detroit, Michigan, 1969.

11. Fash, J.W., Socie, D.F. and Russell, E.S., "Fatigue Crack Initiation and Growth in Gray Cast Iron," Proc., Fatigue '81, Society of Environmental Engineers, Fatigue Group Conference, Warwick University, England, 24-27 March 1981, pp. 40-51.

12. Russell, E.S., "Finite Element Simulation of the Microstructure of Gray Cast Iron," Fracture Control Program, Report No. 33, College of Engineering, University of Illinois at Urbana-Champaign, December 1979.

13. Downing, S.D. and Socie, D.F., "Stress/Strain Simulation Model for Gray Cast Iron," International Journal of Fatigue, Vol. 4, No. 3, July 1982, pp. 143-148.

14. Gilbert, G.N.J., "The Stress/Strain Properties of Nodular Cast Irons in Tension and Compression," Journal of the British Cast Iron Research Association, Vol. 12, No. 2, March 1964, pp. 170-193.

15. Testin, R.A., "Interim Report on Fatigue Behavior of High Hardness Nodular Cast Iron," Fracture Control Program, Report No. 7, College of Engineering, University of Illinois at Urbana-Champaign, March 1973.

16. Palmer, K.B., "Fatigue Properties of Cast Iron, Engineering Properties and Performance of Modern Iron Castings," British Cast Iron Research Association, Birmingham, England, 1970, p. 97.

17. Palmer, K.B., "Mechanical Properties of Compacted-Graphite Irons," British Cast Iron Research Association, Birmingham, England, 1976, p. 31-37.

18. Gilbert, G.N.J. and Kemp, S.D., "The Cyclic Stress/Strain Properties of Flake Graphite Cast Iron - A Progress Report," Journal of the British Cast Iron Research Association, Vol. 28, 1980, pp. 284-296.

19. Blackmore, P.A. and Morton, K., "Structure-Property Relationships in Graphite Cast Irons," International Journal of Fatigue, Vol. 4, No. 3, July 1982, pp. 149-155.

20. Gilbert, G.N.J., "Mechanical Properties of Graphite Cast Irons," Iron & Steel, January, February and March 1957.

21. Topper, T.H., Wetzel, R.M. and Morrow, JoDean, "Neuber's Rule Applied to Fatigue of Notched Specimens," Journal of Materials, Vol. 4, No. 1, March 1969, pp. 200-209.

22. Mitchell, M.R., "A Unified Predictive Technique for the Fatigue Resistance of Cast Ferrous-Based Metals and High Hardness Wrought Steels," Fracture Control Program, Report No. 23, College of Engineering, University of Illinois at Urbana-Champaign, September 1976.

23. Testin, R.A., "Characterization of the Cyclic Deformation and Fracture Behavior of Nodular Cast Iron," M.S. Thesis, University of Illinois at Urbana-Champaign, 1973; also T. & A.M. Report No. 371, Department of Theoretical and Applied Mechancis, University of Illinois at Urbana-Champaign, June 1973.

24. Fash, J.W., "Fatigue Crack Initiation and Growth in Gray Cast Iron," Fracture Control Program, Report No. 35, College of Engineering, University of Illinois at Urbana-Champaign, October 1980.

25. Molinaro, L., "Fatigue Behavior and Crack Development in Compacted Graphite Cast Iron," Fracture Control Program, Report No. 39, College of Engineering, University of Illinois at Urbana-Champaign, May 1981.

26. Starkey, M.S. and Irving, P.E., "The Influence of Microstructure on Fatigue Crack Initiation in Spheroidal Graphite Cast Iron," Proc., Int. Symp. on Low Cycle Fatigue Strength and Elasto-Plastic Behavior of Materials, Stuttgart, 1979.

27. Hua, C., "Fatigue Crack Growth in Nodular Cast Iron," Fracture Control Program, Report No. 47, College of Engineering, University of Illinois at Urbana-Champaign, February 1983.

28. Smith, K.N., Watson, P. and Topper, T.H., "A Stress/Strain Function for the Fatigue of Metals," Journal of Materials, JMLSA, Vol. 5, No. 4, December 1970, pp. 767-778.

29. Fash, J.W. and Socie, D.F., "Fatigue Behavior and Mean Effects in Gray Cast Iron," International Journal of Fatigue, Vol. 4, No. 3, July 1982, pp. 137-142.

30. Douglas, M.J. and Plumtree, A., "Application of Fracture Mechanics to Damage Accumulation in High Temperature Fatigue," Fracture Mechanics, ASTM STP 677, 1979, pp. 68-84.

31. Kachanov, L.M. in Problems of Continuum Mechanics, Society for Industrial and Applied Mathematics, Philadelphia, 1961, pp. 202-218.

32. Lemaitre, J. and Plumtree, A., "Application of Damage Concepts to Predict Fatigue Failures," Journal of Engineering Materials and Technology, ASME, Vol. 101, July 1979, pp. 284-292.

33. Socie, D.F., Fash, J.W. and Leckie, F.A., "A Continuum Damage Model for Fatigue Analysis of Cast Iron," to be presented at the ASME Conference on "Advances in Life Prediction Methods," September 1983.

34. Brussat, T.R., "Rapid Calculation of Fatigue Crack Growth by Integration," Fracture Toughness and Slow-Stable Cracking, ASTM STP 559, 1974, pp. 298-311.

35. Galliart, D.R., "Estimating Fatigue Crack Propagation Lives at the Test Site," Fracture Mechanics, ASTM STP 677, 1979, pp. 757-769.

36. Socie, D.F., "Prediction of Fatigue Crack Growth in Notched Members Under Variable Amplitude Loading," Engineering Fracture Mechanics, Vol. 9, No. 4, 1977, pp. 849-865.

3. Downing, S.D. and Socie, D.F., "Simple Rainflow Counting Algorithms," International Journal of Fatigue, Vol. 4, No. 1, January 1982, pp. 31-40.

38. Raske, D.T. and Morrow, JoDean, "Low Cycle Fatigue Testing from a Mechanics of Materials Viewpoint," Manual on Low Cycle Fatigue Testing, ASTM STP 465, 1969, pp. 1-32.

VITA

Stephen Douglas Downing was born July 19, 1947 in Brockton, Massachusetts. He attended elementary and high school in Randolph, Massachusetts and graduated with honors in 1965. He then entered the University of Illinois and received a B.S. in Engineering Mechanics in 1970 and an M.S. in Theoretical and Applied Mechanics in 1971. In 1974, he joined his present employer, Deere & Company Technical Center, where he is involved with fatigue and failure analysis. In 1980, he entered the Department of Mechanical Engineering at the University of Illinois to further his education and pursue a Ph.D.

A list of his publications for the past several years are:

1. Downing, S.D. and Socie, D.F., "Modeling the Cyclic Deformation Behavior of Gray Iron Under Axial Strain," Proceedings of SEECO '83, Digital Techniques in Fatigue, Society of Environmental Engineers, The City University, London, England, 28-30 March 1983, pp. 152-175.

2. Downing, S.D. and Socie, D.F., "Stress/Strain Simulation Model for Gray Cast Iron," International Journal of Fatigue, Vol. 4, No. 3, July 1982, pp. 143-148.

3. Downing, S.D. and Socie, D.F., "Simple Rainflow Counting Algorithms," International Journal of Fatigue, Vol. 4, No. 1, January 1982, pp. 31-40.

4. Galliart, D.R., Downing, S.D. and Berns, H.D., "Computer Based Material Properties...An Effective Link to Reliable Products," Closed Loop, Vol. 9, No. 1, May 1979, pp. 3-14.

5. Galliart, D.R. and Downing, S.D., "Development of Data Reduction Procedures Which Yield Useful Design Parameters," SAE Paper No. 760682.

6. Downing, S.D., Galliart, D.R. and Berenyi, T.A., "A Neuber's Rule Fatigue Analysis Procedure for Use with a Mobile Computer," SAE Paper No. 760317.

7. Tucker, L.E., Downing, S.D. and Camillo, L., "Accuracy of Simplified Fatigue Prediction Methods," SAE Paper No. 750043.

8. Downing, S.D., "Comparison of Total and Incremental Plasticity Analyses for Two Classes of Problems," M.S. Thesis, University of Illinois, Urbana, Illinois, 1971.

He is a member of the Honor Society of Phi Kappa Phi.